1-1-2020

The Design of Tribological Composites for Multifunctional Applications: Model Development and Topology Optimization

Xiu Jia
Lehigh University

The Design of Tribological Composites for Multifunctional Applications: Model Development and Topology Optimization

by

Xiu Jia

Presented to the Graduate and Research Committee

of Lehigh University

in Candidacy for the Degree of

Doctor of Philosophy

in

Mechanical Engineering

Lehigh University

January 2020

Approved and recommended for acceptance as a dissertation in partial fulfillment of the requirements for the degree of Doctor of Philosophy.

_____
Date

_____
Dissertation Advisor

Committee Members:

_____
Prof. Natasha Vermaak, Committee Chair

_____
Prof. Brandon Krick

_____
Prof. Nik Nikolov

_____
Prof. Nicholas Strandwitz

_____
Prof. Yue Yu

Acknowledgments

I would like to express my deep gratitude to my advisor, Prof. Natasha Vermaak, for her consistent guidance, patience, inspiration, and encouragement throughout my PhD journey. I thank her for always supporting me both academically and emotionally especially at those stressful and tough moments. I feel extremely lucky to have such a caring advisor and mentor like her.

I would like to extend my gratitude to Prof. Brandon Krick. I thank him for introducing me to the field of tribology, working with me closely, and providing inspiring discussions and constructive insights on a regular basis. I would also like to acknowledge my committee members, Prof. Yue Yu, Prof. Nicholas Strandwitz, and Prof. Nik Nikolov, for their generous help and valuable feedback.

I would like to thank my collaborator, Tomas Grejtak, from the Tribology Lab. It has been a great pleasure to work with him. This dissertation could not be complete without his hard work on the experiments. I thank my colleagues in Prof. Vermaak's group, my WiSE ladies, and all my friends for their friendship and support.

Special thanks to my family especially my parents for their unconditional love and

support. They are the most important people in my life, and I dedicate this dissertation to them.

Content

List of Tables

List of Figures

Abstract

As a result of the significant economic and environmental burdens caused by wear, extensive research has been conducted to understand, predict, and control wear to achieve desired performance and lifetimes for tribological systems. Sliding interfaces in many tribological systems must also be multifunctional, prompting the need to optimize for a range of properties and processes. Composites serve as great multifunctional candidates for targeted properties and performance: including mechanical, thermal, electrical, and chemical. However, current material selection and design processes for tribological composites are often trial-and-error, time-consuming and involve significant material and energy waste. This dissertation presents a new design framework that can direct and accelerate the development of tribological composites for combined wear and thermal performance. The framework integrates three main components: (i) wear models that can predict the evolution of key metrics (surface topography, material loss, contact pressure and temperatures) (ii) wear experiments that are used to evaluate and validate the wear models and (iii) topology optimization tools that control the spatial arrangement of materials in tribological composites to achieve target multifunctional performance. In particular, existing wear models are improved and enhanced for the design of rotary and linear wear systems. One of the major contributions is the development of a thermomechanical wear model that includes frictional

heat generation and transfer, along with temperature-dependent wear rates. The model developments are incorporated into several topology optimization protocols, and for the first time, a framework to design tribological composites for enhanced frictional heat dissipation is presented. The material distribution within bi-material composites is optimized to minimize temperatures at sliding interfaces while maintaining target wear performance.

Chapter 1

Introduction

Tribological composites are used in a wide range of industries including energy, transportation, aerospace, and biological sectors. Current design processes for these composites are largely empirical and trial-and-error, involving significant material and energy waste. *The overall goal of this dissertation is to establish a systematic framework for the design of tribological composites undergoing abrasive sliding wear.*

1.1 On the importance and impact of tribology

Tribology is the branch of science and engineering concerned with interacting surfaces in relative motion and includes the study of friction, wear and lubrication [2]. Since the term *Tribology* was first coined by Peter H. Jost, a British engineer, in 1964 [3], it has become an important interdisciplinary area that links mechanics, materials, chemistry, physics, biology and more. Almost every engineering system has surfaces that move against each other where tribological interactions occur. Loss of energy due to friction and wear in

engineering systems accounts for huge economic losses and environmental burdens. In 2017, Holmberg and Erdemir [4] investigated the global impact of friction and wear on energy consumption, economic expenditures, and CO_2 emissions covering transportation, manufacturing, power generation, and residential sectors. The study concluded that (i) approximately 23% of global energy consumption originates from tribological contacts (ii) by implementing advanced tribological technologies the potential global savings would amount to 1.4% of the annual GDP and 8.7% of the total energy consumption in 15 years and (iii) the global CO_2 emissions can be reduced by 3,140 $MtCO_2$ resulting in cost savings of 970,000 million Euros over 15 years.

1.2 Wear

This dissertation focuses on the mechanics of wear, more specifically, abrasive sliding wear. Wear always occurs when surfaces slide against each other. It can be defined as "damage to a solid surface, generally involving progressive loss of materials, due to relative motion between that surface and a contacting substance or substances" [5]. Wear can be classified into different types based on the contact involved (sliding, rolling, impact, fretting, and slurry), the surface damage mechanism (abrasive, adhesive, fatigue, corrosive), the presence of a lubricant (dry or unlubricated, wet or lubricated), etc. [5]. In this dissertation, dry abrasive sliding wear is of interest, where material is removed from a sliding surface by the hard protuberances on a counter surface without lubrication (as illustrated in Figure 1.1) [2].

In some cases, wear is desirable and can be used constructively. For example, in grinding and polishing processes, wear is utilized to remove materials and to shape surfaces [6]. How-

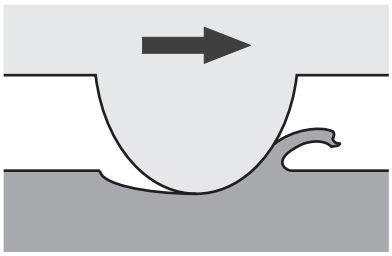

Figure 1.1: Schematic of dry abrasive sliding wear.

ever, most of the time, wear is detrimental and can lead to reduced efficiency of operation and significant maintenance and replacement costs. Therefore, wear should be considered early in the design processes of engineering systems that involve moving interfaces such as gas turbine engines, automotive engines and transmissions, tires and brakes, hard disk drives for data storage, electromechanical devices, artificial human joints, etc. [5].

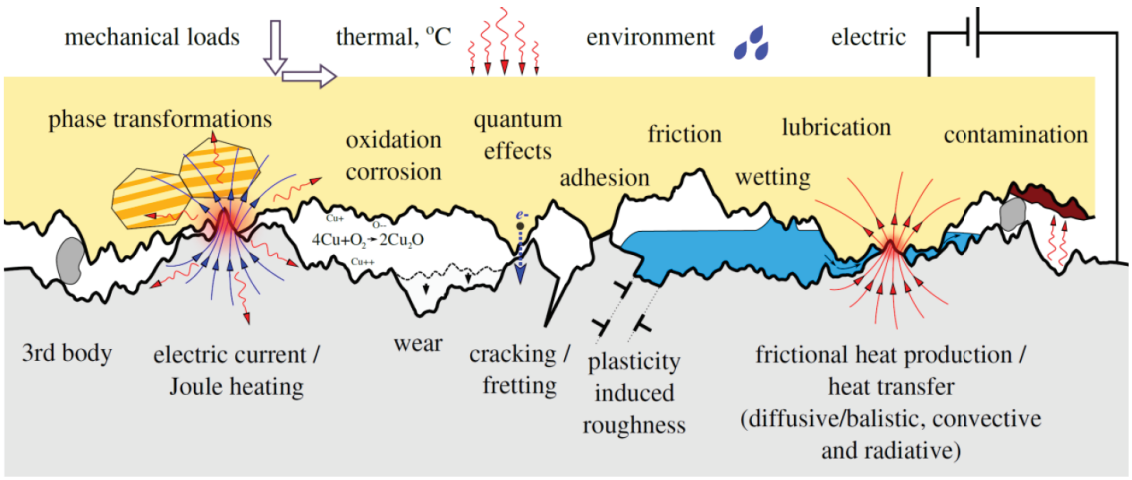

Figure 1.2: Schematic representing the multiphysical nature of tribological interactions [7].

Understanding wear mechanisms is the foundation for reducing or controlling its effects. Wear involves multiple physics at multiple scales. Solid surfaces contain geometrical features at scales ranging from macroscale profile or waviness, roughness, to atomic fluctuations. Wear is accompanied by various physical phenomena taking place at and near sliding interfaces, including mechanical, thermal, chemical, electrical, etc. (Figure 1.2) [7, 8]. The thermomechanical aspect is one of the most critical and strongly coupled multiphysics of

wear [7]. Wear is always complicated by friction. During frictional processes, most of the available mechanical energy will be transformed into heat [9], which causes the temperature to rise, especially at sliding interfaces. In some cases, frictional heating is favorable. For example friction welding utilizes frictional heat to join materials. However, most of the time, temperature rise caused by frictional heating can degrade tribological and mechanical properties, impacting the operation and lifetime of sliding components. Due to the complex nature of wear, tremendous effort has been made to investigate wear from experimental, theoretical, and numerical aspects and across length and time scales (Figure 1.3) [10].

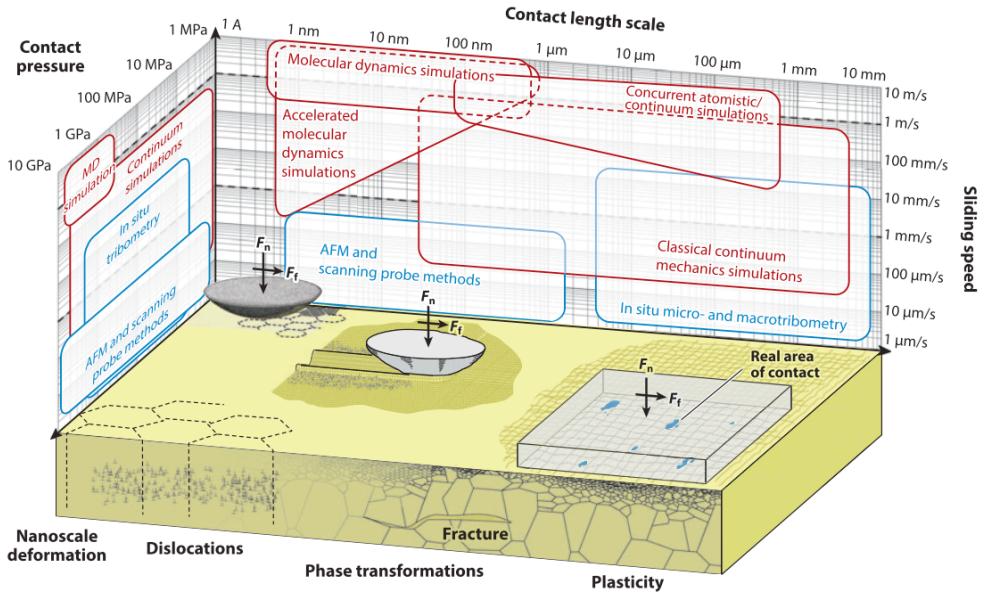

Figure 1.3: Schematic from [11] shows materials tribology spans multiple length scales and timescales. There are currently areas of strong overlap between experimental capabilities and both numerical and theoretical modeling of tribological processes.

Experimental investigations of wear have been carried out to examine wear mechanisms, provide constitutive tribological properties of materials and systems, and simulate practical applications. Tribometers are the instruments used in most of the experimental studies to evaluate wear and friction. Tribometers differ considerably in design and must be selected based on the wear mechanisms of interest, contact configurations, and operating conditions.

The recent development of high-resolution instrumentation such as atomic force microscopes (AFM) has also enabled the fundamental investigation of tribological processes at small length scales (1nm-1μm) [11].

Typical experiments assess wear based on the amount of material volume loss and the state of the worn surface [12]. The measurement of volume loss can be made directly by weighing the mass change and measuring change in dimensions. It can also be inferred based on the topographical measurement made by optical profilometers such as interferometers and stylus profilometers. The accurate measurement of macro-, micro- and nano-scale surface topographies provides information about both surface profile and local damage and is helpful for identification of wear mechanisms. In addition to these two major metrics, several other factors can also be monitored during wear experiments, such as coefficient of friction and contact temperature. Coefficient of friction can be determined based on the applied normal load and measured friction force obtained from the tribometers. There have been many techniques developed to measure contact temperature, such as embedded thermocouples, infrared detectors, *in situ* thermal micro-tribometer, etc. [13, 14].

A simple but common way to interpret measurements from wear experiments involves application of Archard's wear equation. The equation (Equation (1.1)) was initially proposed by Archard and Hirst [15] to measure adhesive wear of metals under unlubricated conditions but has been extended to more general cases of wear and materials beyond metals. As shown in Figure 1.4(a), it states that the volume of material lost, ΔV, from a surface is proportional to the relative sliding distance, Δs, the applied normal load, F_n, and a coefficient, K:

$$\Delta V = F_n K \Delta s. \tag{1.1}$$

This equation combines all parameters related to materials, operating and contact conditions, environment, and lubricants into one coefficient. This coefficient, K, is the so-called "wear rate" and has units of $mm^3/(Nm)$. It is a system parameter that characterizes the wear resistance of a material in a particular wear system. As shown in Figure 1.4(b), the values of wear rates can vary from 10^{-3} to 10^{-10} $mm^3/(Nm)$ across different materials as well as within the same material family depending on the particular wear conditions. There have been studies that determine the value of wear rates based on intrinsic material properties, active wear mechanisms, and relevant operating conditions [16], however, the most common approach is to conduct wear experiments.

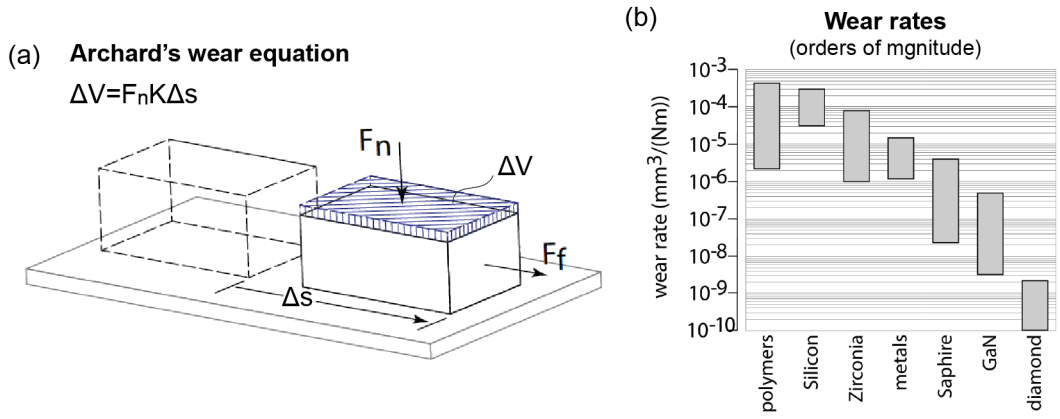

Figure 1.4: Schematic of Archard's wear equation and wear rate. (a) Schematic of Archard's wear equation. (b) General ranges of wear rates for different materials.

In experiments, it is commonly observed that wear undergoes a transition from an initial run-in regime to a steady-state regime as sliding proceeds. According to the GOST (former USSR) Standard, run-in is defined as "the change in the geometry of the sliding surfaces and in the physicomechanical properties of the surface layers of the material during the initial sliding period, which generally manifests itself, assuming constant external conditions, in a decrease in the frictional work, the temperature, and the wear rate" [17].

Figure 1.5(a) shows is a typical wear volume loss evolution where the volume loss in-

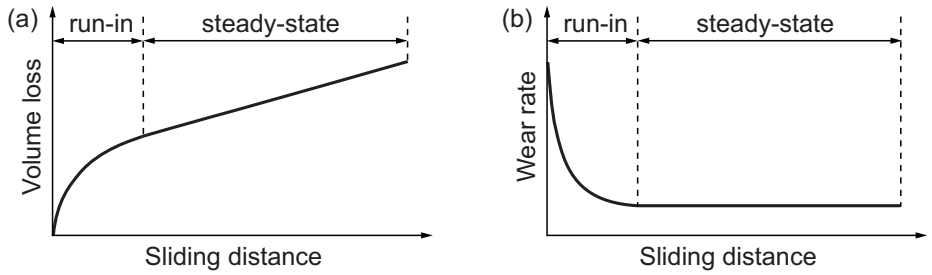

Figure 1.5: Schematic of typical wear regimes: run-in and steady-state. (a) Volume loss evolution. (b) Wear rate evolution.

creases rapidly during run-in, then reduces in rate upon reaching steady-state. When the applied normal load on the material is kept constant, the slope of the volume loss curve reflects the wear rate, which decreases from an initially high value and gradually converges to a lower value as shown in Figure 1.5(b). This stabilization results from adjustments between contacting surfaces which may include surface conformity, oxide film formation, material transfer, phase transformation, subsurface micro-structural reorientation, etc. [18]. It should be noted that this dissertation only takes the adjustments of the macro-scale surface topographies into account while not considering any changes in surface roughness, fundamental contact conditions and wear mechanisms. This has been shown elsewhere [10,14,19] to be an appropriate approximation for many sliding abrasive wear systems ranging from chemical mechanical polishing (CMP) to dinosaur dentition.

Along with numerous experimental investigations, many numerical tools have been developed and utilized to model and predict wear. Molecular dynamics (MD) simulations have been unitized to explain and model atomic-scale tribological phenomena. MD is able to provide unique fundamental insights into the coupling between the complex atomic-scale processes and the macroscale tribological behavior of materials [11]. For example, Zhang et al. [21] investigated the diamond-copper sliding system and revealed distinct deformation regimes including no-wear, adhering, ploughing and cutting regimes. Jang et al. [22] demon-

strated that the molecular structural orientation at polytetrafluoroethylene (PTFE) surfaces strongly influences wear and friction. Cheng et al. [23] identified the thermo-chemical wear mechanisms for diamond cutting tools in the nanometric cutting of single crystal silicon through combining MD simulations with AFM experiments. Despite the demonstrated usefulness of atomistic simulations in understanding fundamental mechanisms of wear, the widespread application of these tools remains limited by their length and time scales and computational costs [11].

Wear has also been historically investigated and modeled from a continuum mechanics perspective [16,20]. Many theoretical studies have been conducted to probe specific mechanical mechanisms of wear [16]. Traditionally, the wear mechanisms for metallic surfaces have been probed based on the theory of plastic deformation, in particular, plastic ratchetting of the near-surface layer in repeated sliding contact [24, 25]. For ceramics, Wang et al. [26] investigated the mechanism transition from plastic deformation-controlled to crack/fracture-controlled wear due to contact stresses exceeding critical micro-crack/fracture stresses.

Numerical tools, such as finite element analysis (FEA), have also been used to simulate interactions between rough surfaces or asperities (including elastoplasticity and fracture) to reveal different wear mechanisms and estimate the wear resistance of materials [27–29]. In addition to these more fundamental investigations, FEA-based wear simulation frameworks have been developed to estimate the lifetime and geometric change of moving components for various practical applications, such as conical joint wear [30], oscillatory contacts [31, 32], fretting wear [33] and hip joint wear [34]. Since wear always involves evolving surface geometries and contact conditions, these type of simulations usually consist of an iterative procedure that integrates Archard's wear equation and contact analysis by FEA as shown

in Figure 1.6. The continuous wear process is approximated at discrete time increments. At each increment, the contact pressure distribution is obtained by performing the contact analysis based on the current geometry and contact conditions. The height loss at all positions along the sliding interface is evaluated using Archard's wear equation (Equation (1.4)). Then the surface geometry is updated according to the calculated height loss and is used for the contact problem at the next increment. The above steps are executed iteratively until a stop criterion is met. Typically, stop criteria include maximum sliding distance or time, convergence to steady-state, and wear-out failure.

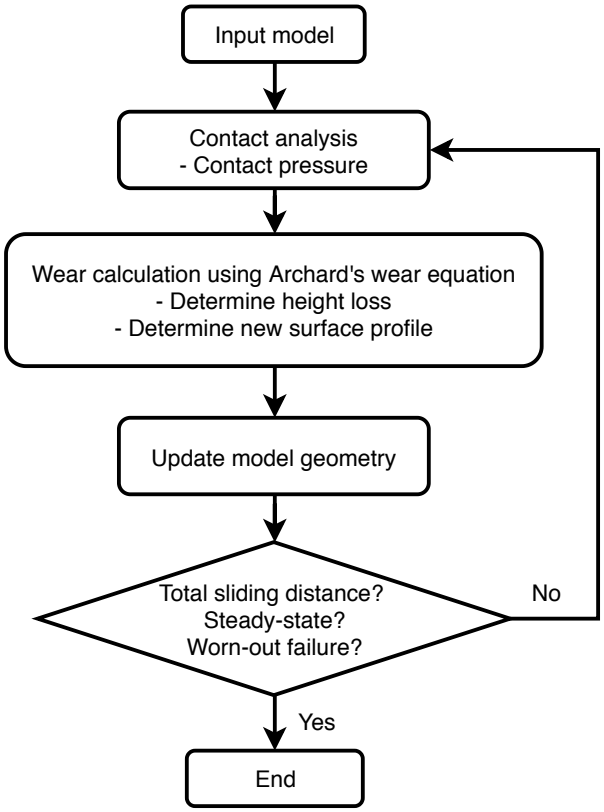

Figure 1.6: Flow chart of a typical wear simulation procedure.

The detailed contact analysis performed by FEA has the advantage of providing accurate contact information, i.e. stress, strain, and contact pressure. However, it is usually computationally expensive and time-consuming because the contact problem needs to be solved

at each time increment along with updates to geometry [35]. To address this, strategies have been proposed to accelerate the FEA-based simulations. For example, extrapolation techniques have been used to reduce the total number of FE contact analyses [31].

In engineering applications, simple and reliable wear models are often preferred in material selection and design processes for achieving desired performance and lifetime estimates. However, due to the multiscale and multidisciplinary nature of wear, it is widely accepted that no simple and universal model is applicable to all wear situations [16, 20]. Instead, models for wear are usually tailored to specific wear conditions and scales as illustrated in Figure 1.3 [11]. For example, analytical contact formulations of elastic half-space contacts derived from the Boussinesq and Cerruti potential functions are applicable for modeling chemical mechanical polishing (CMP) [19]. Elastic foundation models have also proven to be promising for efficient wear simulations. The Winkler foundation model is the first elastic foundation model that was incorporated into wear simulation [35]. In the Winkler foundation model, the surface is represented by a bed of elastic springs as shown in Figure 1.7(a). Each spring is independent with no lateral interactions. The contact pressure is calculated locally from deformation of the elastic foundation:

$$P = k_s u, \tag{1.2}$$

where k_s is the stiffness of the springs representing the compliant foundation and u is the local vertical deflection of the springs.

Sawyer [10] established a numerical scheme based on the Pasternak foundation model to investigate surface dishing, erosion phenomenon and contact pressure evolution during chemical mechanical polishing (CMP). This Pasternak-based model was later used to for

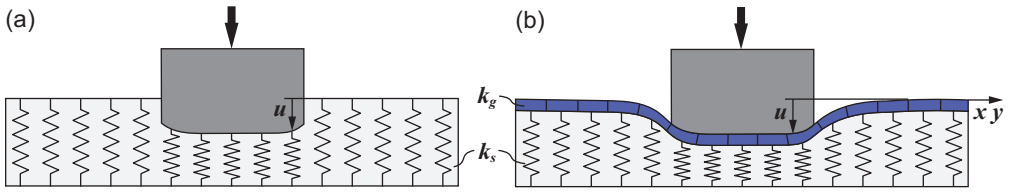

Figure 1.7: Schematic of foundation models. (a) Winkler foundation model. (b) Pasternak foundation model.

the analysis of wear in grinding dentitions of hadrosaurid dinosaurs, incorporating fossilized wear properties [36, 37]. In the Pasternak foundation model, the elastic spring elements representing the compliant counter-body are coupled to a surface layer of beam elements as shown in Figure 1.7(b). The contact pressure is given by:

$$P = k_s u - k_g \nabla^2 u, \tag{1.3}$$

where k_s is the stiffness of the springs, k_g is the foundation parameter that takes the local curvature of the beam element layer into account, and $\nabla^2 = \frac{\partial^2}{\partial x^2} + \frac{\partial^2}{\partial y^2}$ is the Laplacian operator.

The application of the Pasternak foundation model for iterative wear simulations of multi-material surfaces subject to linear abrasive sliding wear was investigated by Sidebottom et al. [38]. The transition from run-in to steady-state wear regime has been shown numerically by monitoring the surface profile evolution and material volume loss history. This work was later mathematically reformulated by Feppon et al. [39] so that a direct solution of the steady-state wear could be obtained from the governing well-posed partial differential equation (PDE) system. Feppon's reformulated wear model was also integrated into a topology optimization protocol to design periodic composites for minimal run-in volume loss in linear wear systems [40]. The effectiveness of the identified periodic designs

was assessed by several wear experiments [41]. *Through this dissertation, the foundation-based wear models are further modified and extended to address different wear systems for improved predictive accuracy and functionality.*

1.3 Topology optimization: a design approach for composites

Composites are material systems consisting of two or more materials which are designed for multifunctionality that is superior to any of the material constituents acting alone [43]. Tribological composites have been historically used in automotive clutch facings and brake linings to provide high friction, low wear and structural rigidity during operation [44]. Composite coatings are usually designed for enhanced tribological, electrical, optical, and chemical functions to protect components such as bearings, seals, and valves [2]. Polymer-based tribological composites combine their intrinsic properties (such as being lightweight and corrosion resistant) with unique properties of their reinforcements. For example, reinforcing fibers (carbon, glass, or aramid) can enhance wear resistance and solid lubricants (PTFE, graphite or MoS_2) can reduce friction [45]. Another example is the recent development of a novel wear resistant epoxy composite that incorporates diisocyanate-based self-healing agents that reduce the growth of fatigue cracks during rolling while also improve fracture toughness [46].

While the conventional empirical and trial-and-error design approaches for tribological composites have had many successes, they are also time-consuming and can lead to significant material and energy waste [47,48]. Outside of tribological fields, the increasing demand for multifunctional composites has led to the development of new analysis tools and design methodologies to relate constituent material properties and material distributions to target

multifunctional performance. Among these new design paradigms, topology optimization offers a powerful framework to address the design challenges of multifunctional composites. In this dissertation, topology optimization is leveraged for *multifunctional tribological composites*.

Topology optimization is a mathematical approach that finds the optimal lay-out or material distribution in a design domain for a given objective [49]. Topology optimization was introduced for structural design problems by Bendsøe and Kikuchi in 1988 [50]. Typically, structural optimization can be classified into two broad categories as illustrated in Figure 1.8: sizing and topology optimization. Sizing optimization determines the thickness, length, or other geometric parameters of members which are predefined in the structure. However, topology optimization does not require any initial geometric parametrization of the structure and allows structural connectivity or topology to evolve during the design process. In this way, it offers more design freedom than sizing optimization and can lead to more non-intuitive designs with high-performance. With the goal of finding the best material distribution in a design domain for an objective function, topology optimization couples physical modeling with optimization algorithms to drive the design decision in a systematic and mathematics-driven manner. This makes topology optimization a powerful alternative to the conventional empirical and trial-and-error design approaches for tribological composites.

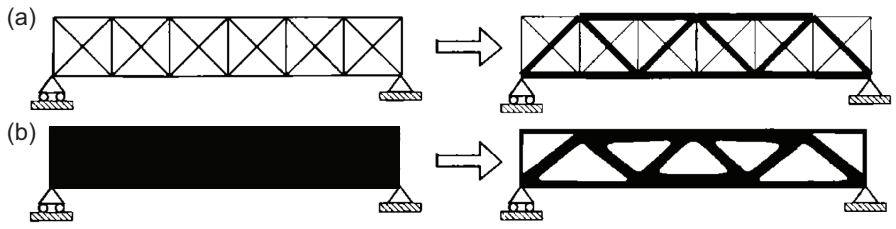

Figure 1.8: Categories of structural optimization based on [49]. (a) Sizing optimization. (b) Topology optimization.

Since the introduction of the homogenization method [50], many approaches have been developed to perform topology optimization. The main differences among these approaches are related to the definition or parameterization of the design domain in terms of how to present material(s) and void (no material). It should be noted that due to the nonlinear and non-convex nature of almost all topology optimization problems, regardless of approach, global optimality cannot be guaranteed [49]. Density-based methods are the most widely used, where the design domain is discretized into elements and each element is characterized by one design variable, i.e. element density, ρ_e. Elements with density $\rho_e = 1$ are occupied by solid material and elements with density $\rho_e = 0$ are void or another solid material. The discrete optimization problem is converted into a continuous one by allowing the density variables to have values between 0 and 1 or ρ_{min} and 1 ($\rho_{min} > 0$ is used to prevent computational difficulties such as singularity in the finite element analysis). As shown in Figure 1.9(a), black represents a solid material with $\rho_e = 1$, white represents void with $\rho_e = \rho_{min}$, and gray has intermediate density. The material properties of each element are calculated based on the element density using appropriate interpolation schemes. The Solid Isotropic Material (originally Microstructure) with Penalization (SIMP) method is the most common scheme. In the SIMP method, material properties, such as the elastic modulus (E_e) of an element with density ρ_e is calculated as:

$$E_e = E_0 \rho_e^p, \tag{1.4}$$

where E_0 is the elastic modulus of the solid material and p is a penalization parameter. The design goal is to achieve an optimal discrete distribution of void and solid elements within the design domain, i.e. 0/1 design. The penalization parameter is chosen to be larger

than 1 which has been proven to help suppress intermediate densities and encourage 0/1 designs [49]. Figure 1.9 shows the interpolated modulus as a function of element density with a range of penalization parameters (p). The exact value of the parameter (p) is often chosen depending on the specific optimization problem but $p \geq 3$ is usually required [49].

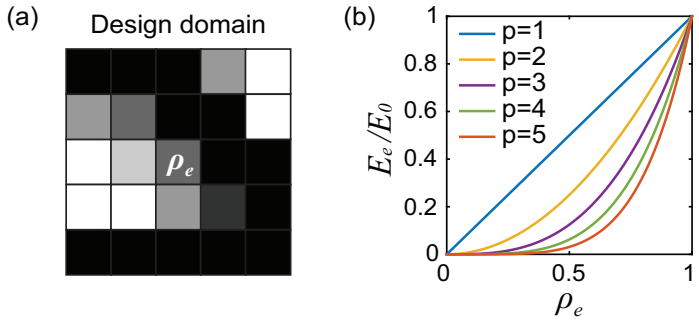

Figure 1.9: Schematic of the density-based method (SIMP). (a) Parameterization of design domain. (b) SIMP interpolation schemes.

Another well-developed approach for topology optimization is the boundary variation method, where the material distribution in the design domain is represented by implicit functions that define boundaries between solid and void or different solids. For example, in the level-set method, solid/void or material boundaries are found as the zero level-set or contour of a scalar level-set function. As illustrated in Figure 1.10, the distribution of two materials (A and B) in a two-dimensional design domain, Ω, is represented by the closed zero level-sets, $\partial\Omega_a$, of the three-dimensional level-set function, ϕ. The evolution of the boundaries (moving, merging and creating new inclusions) is realized by updating the level-set function according to the shape and topological derivatives obtained from the physical problem and optimization conditions [51–53]. One advantage of the level-set method over density-based methods is the clear boundaries between different materials without elements that have (often non-physical) intermediate densities. Techniques such as using extended finite element methods (XFEM) can further improve the smoothness of material boundaries

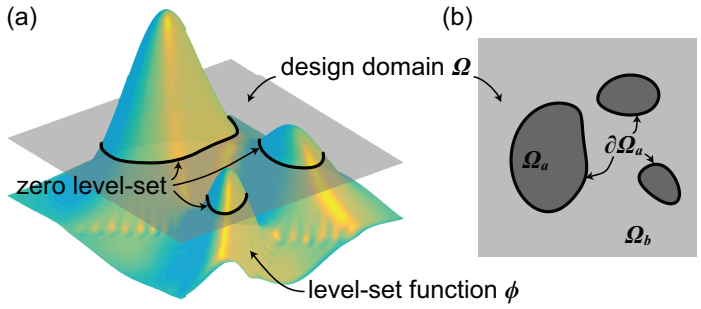

Figure 1.10: Schematic of the level-set method. (a) Level-set function and its zero-level set. (b) Corresponding material distribution in the design domain.

[54]. However, it has been found that the dependency of the optimal solution on initial guess is significant for the level-set method [55]. In addition, reinitializations to reshape the level-set function are periodically required which increases the computational complexity [53, 56]. Other topology optimization approaches include: discrete methods such as the Evolutionary Structural Optimization (ESO) and Bi-directional Evolutionary Structural Optimization (BESO) methods [57], explicit methods such as the Moving Morphable Components (MMC) method [58, 59] and methods utilizing deep learning and neural networks [60, 61].

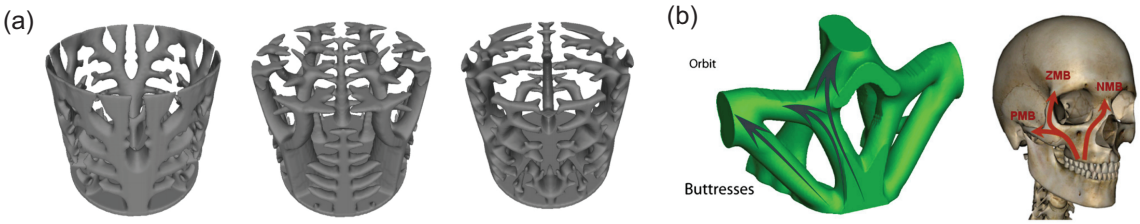

Figure 1.11: Some recent applications of topology optimization. (a) Heat sink designs for LED cooling [62]. (b) Optimized bone craniofacial segmental replacements [63].

Topology optimization offers a generalized design framework that may be applied for a broad range of disciplines, including heat transfer, fluids, acoustics, electromagnetics, optics, biology, medicine, and more [49, 64, 65]. Lazarov et al. [62] designed heat sinks for passive cooling in light-emitting-diode (LED) lamps (Figure 1.11(a)). Sutradhar et al. [63]

designed patient-specific large craniofacial segmental bone replacements (Figure 1.11(b)).

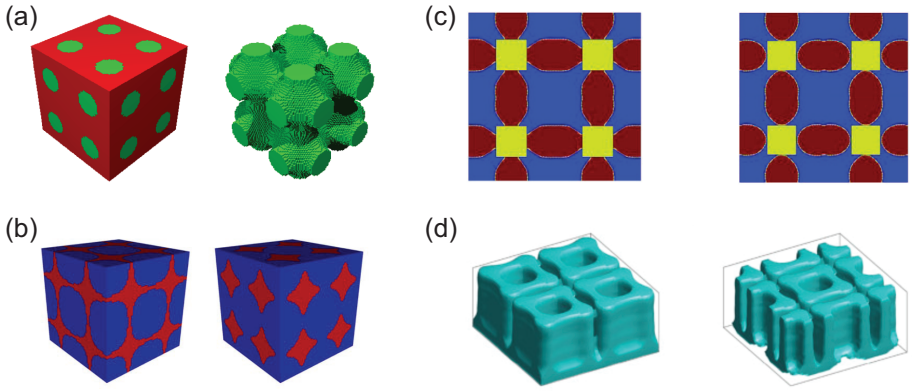

Figure 1.12: Applications of topology optimization for multifunctionality. (a) Transport of heat and electricity [66]. (b) Stiffness and fluid permeability [67]. (c) Stiffness and thermal conductivity [68]. (d) Stiffness and electrical conductivity [69].

Topology optimization has also been extensively used to design multifunctional materials and structures. Torquato et al. [66] presented the first application of topology optimization to optimize composite microstructures for the simultaneous transport of heat and electricity (Figure 1.12(a)). Guest et al. [67] optimized the base cell microstructure of a periodic material for maximized stiffness and fluid permeability (Figure 1.12(b)). In addition, designs for combinations of stiffness and thermal [68] or electrical conductivity [69] have also been proposed (Figures 1.12(c) and (d), respectively).

In contrast, topology optimization for tribological applications has only recently been introduced [41, 70]. In Feppon et al. [70], a level-set based topology optimization framework was proposed that determined optimal periodic composite unit-cell configurations for minimal volume loss during linear abrasive sliding wear. During this dissertation, the work by Feppon et al. was collaboratively validated through experiments for periodic composites (Figure 1.13) [41]. These results illustrate the potential of topology optimization as a means to design and develop tribological composite systems. However, before this dissertation, no prior work had focused on designing composites for multifunctional performance at the

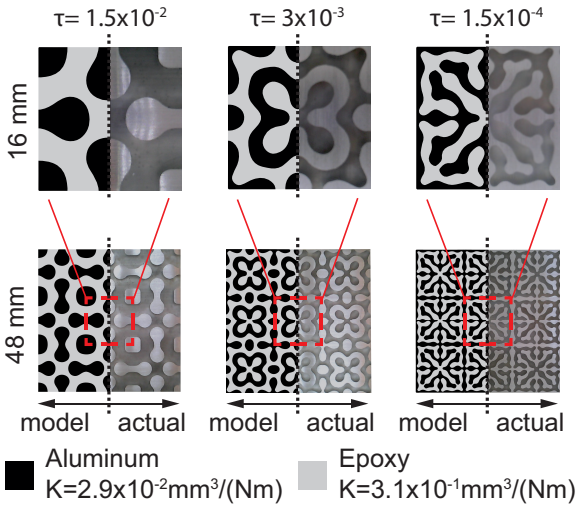

Figure 1.13: Optimized periodic composite unit-cells for minimal run-in volume loss [41,70].

sliding interface.

1.4 Research objective and dissertation outline

To summarize, tribological composites are needed to meet increasing demands for wear and multifunctional performance in tribological systems across different sectors. While current design processes rely on intuitive, parametric and/or trial-and-error approaches, the objective of this dissertation is to develop a systematic framework. Towards this end, this dissertation integrates efficient and accurate predictive wear models with topology optimization to design tribological composites for multifunctional applications.

The dissertation is structured as follows. In Chapter 2, a rotary wear model is established based on the Archard's wear equation and the elastic Pasternak foundation model. This rotary wear model provides both an iterative simulation capacity for the continuous wear process and a direct prediction of steady-state wear performance based on initial material distribution and loading conditions. Wear experiments are conducted (led by col-

laborators) to evaluate the accuracy of the numerical prediction tools. It was found that existing numerical models had difficulty capturing boundary and edge-effects. Chapter 3 addresses this challenge by proposing a generalized wear model that incorporates an implicit treatment of boundary conditions and a new asymmetric foundation model for linear wear. Based on comparison with experiments, these model developments and extensions are found to provide more accurate and realistic wear predictions. Additionally, for the first time, an optimization-based calibration procedure is proposed to obtain foundation parameters needed for implementing the foundation-based wear models. In Chapter 4, frictional heating associated with wear at sliding interfaces is investigated. A three-dimensional steady-state heat transfer model with frictional heat flux boundary conditions is established to obtain thermal fields within sliding components. The heat transfer analysis is integrated into the linear wear simulation framework established in Chapter 3 to investigate thermo-mechanical wear by incorporating temperature-dependent wear rates. Chapter 5 explores the utility of topology optimization in designing multifunctional composites for wear-related problems. A density-based topology optimization framework is developed to find optimal bi-material composites that maximize the dissipation of frictional heat at sliding interfaces with wear performance constraints. Finally, Chapter 6 presents the key conclusions of this dissertation as well as directions for future work.

Chapter 2

Wear models

Existing studies that employ foundation-based wear models have so far only explored linear wear systems where the surfaces in contact undergo relative linear reciprocating or unidirectional sliding. However, rotary wear systems are also common in machinery applications such as clutches and brakes, where the sliding between surfaces is caused by relative rotation. In this chapter, for the first time, one of the classical foundation-based wear models is extended to address rotary abrasive sliding wear systems with a thrust washer configuration. The proposed rotary wear model combines Archard's wear equation (modified for rotary sliding) and the Pasternak elastic foundation model. Iterative simulation is used for efficient predictions of the evolution of key wear features: contact pressure, worn surface profile, and material volume loss. A convergence condition is incorporated to detect the onset of steady-state wear and a direct solution of steady-state wear performance is derived from the model formulation based on the material distribution and loading conditions. The proposed model provides guidance for designing composite surfaces based on desired steady-state wear performance. Rotary wear experiments are conducted (led by collaborators) to

validate the new wear prediction tools and evaluate optimized composite designs.

2.1 Rotary wear model

As shown in Figure 2.1, the rotary wear system of interest has a rotary axial thrust washer geometry. The specimen is rotating against a counter-body causing material removal at the sliding interface, Ω. As is typical for these models, it is assumed that wear only occurs at the specimen surface. The sliding interface of the specimen, Ω, has an annular shape, with an inner radius, $r = R_1$, and an outer radius, $r = R_2$. A polar coordinate system is used with an origin at the center of Ω.

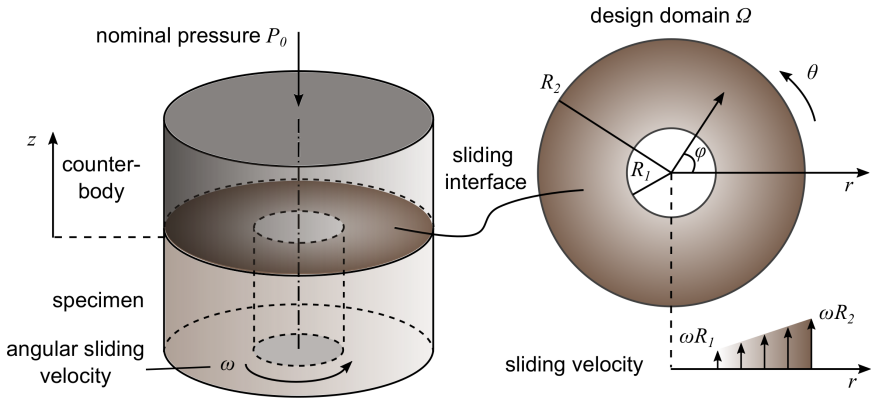

Figure 2.1: Schematic of rotary wear system.

2.1.1 Archard's wear equation: modified for rotary wear systems

Wear is considered on a local scale by following particular points at the sliding surface and determining the wear depth at a particular position according to the local contact conditions. Here, the Archard's wear equation is adapted and applied [15, 71]. The incremental wear depth at a particular position in Ω, $\Delta z(r, \varphi)$, after an incremental angular sliding distance,

$\Delta s(r)$, is calculated as

$$\Delta z(r,\varphi) = -P(r,\varphi)K(r,\varphi)\Delta s(r), \tag{2.1}$$

where $P(r,\varphi)$ is the local contact pressure and $K(r,\varphi)$ is the local wear rate. The wear rate, $K(r,\varphi)$ of unit (mm^3/Nm), characterizes the wear resistance of a material in a specific wear system. Here, it is assumed that each material has a distinct wear rate which does not change during wear. The material distribution within the sliding interface Ω determines the wear rate distribution. When the sliding interface consists of only one material, the wear rate $K(r,\varphi)$ is constant within Ω; when the sliding interface consists of more than one material, the wear rate $K(r,\varphi)$ can be represented by a piecewise constant function of the radial distance from the annulus center, r, and the angular position φ, corresponding to the material distribution.

It is noted that, in contrast to linear sliding wear, rotary wear systems have a radially dependent sliding velocity field (see Figure 2.1), which results in a non-uniform sliding distance distribution. The incremental sliding distance at a particular position is the product of the incremental sliding angle ($\Delta\theta$) and the local radial distance from the center of the annular domain (r):

$$\Delta s(r) = r\Delta\theta. \tag{2.2}$$

In Figure 2.1, θ denotes the *total* rotational sliding angle ($\Delta\theta$ is the incremental rotational sliding angle) while φ denotes the angular coordinate. Then Equation (2.1) is written as:

$$\Delta z(r,\varphi) = -P(r,\varphi)K(r,\varphi)r\Delta\theta. \tag{2.3}$$

In this way, a rotary wear rate coefficient, $K_R(r,\varphi) = rK(r,\varphi)$ of units mm^3/(N rad),

can be defined for rotary wear systems. It is dependent on both the local material wear rate, $K(r, \varphi)$, and the local position, r. As a result, Archard's wear equation is modified for rotary wear systems:

$$\Delta z(r, \varphi) = -P(r, \varphi) K_R(r, \varphi) \Delta\theta. \tag{2.4}$$

This equation gives the incremental wear depth at a particular position that is caused by an incremental rotating angle. The local incremental wear depth is proportional to the local contact pressure and local rotary wear rate. In differential form, the wear model corresponding to Equation (2.4) can be written as:

$$\frac{\partial z(r, \varphi)}{\partial \theta} = -P(r, \varphi) K_R(r, \varphi). \tag{2.5}$$

2.1.2 Pasternak foundation model

Archard's wear equation provides an explicit prediction of the surface profile evolution as long as the pressure distribution between the contacting surfaces is known. In order to provide the contact pressure relation, the elastic Pasternak foundation model [72, 73] that has been previously used in design and validation studies for linear wear systems [74–77] is used. The specimen is assumed to be rotating against an abrasive and fully compliant counter-body. The compliant counter-body is modeled as an elastic foundation which composed of spring elements coupled with bending beam elements (with corresponding parameters k_s and k_g). The units of k_s and k_g are N/mm^3 and N/mm, respectively. These elements are illustrated in Figure 2.2 where a bi-material composite surface is sliding against a compliant counter-body.

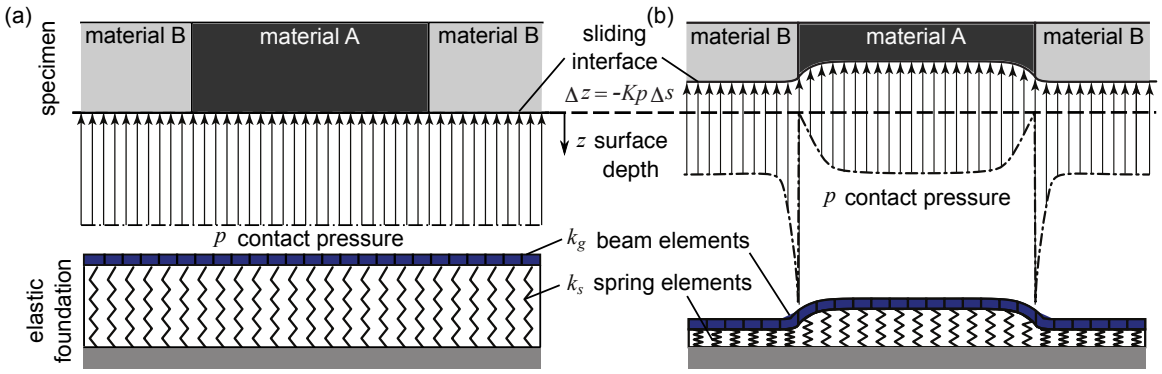

Figure 2.2: Schematic of Pasternak foundation model. (a) Specimen with initially surface and undeformed foundation. (b) Worn specimen surface and deformed elastic foundation.

Initially the composite surface is flat and it is on top of an undeformed elastic foundation as shown in Figure 2.2(a). A constant normal load is applied, causing the foundation springs to compress. Together with the relative sliding between the surfaces in contact, the specimen surface starts to be worn away. Due to the different wear rates of the constituent materials, the initially flat surface becomes uneven, which causes bending of the beam elements at the counter-body surface (Figure 2.2(b)). As a result, the local contact pressure can be represented as a function of the deflection of the spring elements and the local curvature of the beam elements [73, 74]:

$$P = k_s(z - h) - k_g\nabla^2 z, \tag{2.6}$$

where h is a reference depth, and $(z-h)$ is the local deflection of the elastic foundation with respect to this recessing reference depth. Lastly, $\nabla^2 z = \frac{1}{r}\frac{\partial}{\partial r}(r\frac{\partial z}{\partial r}) + \frac{1}{r^2}\frac{\partial^2 z}{\partial \varphi^2}$ is the Laplacian of z in a polar coordinate system that is related to the curvature of the surface beam element layer of the counter-body.

The use of the Pasternak foundation model is based on the assumption that the counter-body is fully compliant so that there is perfect contact between the specimen and the counter-body. The contact pressure is predicted by the displacement of the counter-body

surface, rather than the properties of the constituent materials at the specimen surface. This assumption imposes some restrictions on the applications of the model, such as, sliding against hard materials. Nevertheless, the model has been shown applicable for a broad range of engineering systems from wear of dental materials to chemical mechanical polishing (CMP) [74, 75].

During the entire wear process, the specimen is loaded with a constant normal load, F_n. Thus the average pressure at the sliding surface, $< P >$ ($< \cdot >$ denotes average value throughout the dissertation), remains constant at P_0:

$$< P > (\theta) = \frac{1}{|\Omega|} \int_0^{2\pi} \int_{R_1}^{R_2} P(r, \varphi) r dr d\varphi = P_0, \quad \forall \theta. \tag{2.7}$$

The reference depth, h, is recessing during the wear process. After a total sliding angle, θ, h can be determined by taking the average of both sides in Equation (2.7):

$$h = -\frac{P_0}{k_s} + < z > - \frac{k_g}{k_s} < \nabla^2 z >, \tag{2.8}$$

which leads to the following relationship between the pressure, P, and the local depth of the surface profile, z:

$$P(r, \varphi) = P_0 + k_s(z - < z >) - k_g(\nabla^2 z - < \nabla^2 z >). \tag{2.9}$$

2.1.3 Rotary wear model formulation

Combining modified Archard's wear equation (Equation (2.5)) and the Pasternak foundation model (Equation (2.9)), the recessing local surface depth, $z(\theta, r, \varphi)$, can be determined

by solving the following differential equation with appropriate initial and boundary conditions:

$$\frac{1}{K_R}\frac{\partial z}{\partial \theta} + k_s(z - < z >) - k_g(\nabla^2 z - < \nabla^2 z >) = -P_0. \tag{2.10}$$

Here, composite systems with rotationally symmetric material distributions are of interest. This allows for the further simplification of the model from two-dimensional to one-dimensional, representing a line-scan along the radial direction that is independent of φ. Then the Laplacian of $z(\theta, r)$ in the governing equation (2.10) can be simplified as $\nabla^2 z = \frac{1}{r}\frac{\partial}{\partial r}(r\frac{\partial z}{\partial r})$.

The surface is considered flat before wear occurs, which gives the initial condition, i.e. $z(0, \cdot) = 0$. In terms of boundary conditions, Neumann boundary conditions with zero slope are assumed for both the inner and outer annulus boundaries. In summary, the governing equation to predict the evolution of the design surface profile for rotary wear systems is written as:

$$\begin{cases} \frac{1}{K_R}\frac{\partial z}{\partial \theta} + k_s(z - < z >) - k_g(\nabla^2 z - < \nabla^2 z >) = -P_0, \quad r \in (R_1, R_2), \\ \frac{\partial z}{\partial r} = 0, \text{ at } r = R_1 \text{ and } r = R_2, \\ z = 0, \ \theta = 0. \end{cases} \tag{2.11}$$

2.2 Iterative wear simulation

By solving the time-dependent governing equation for the continuous rotary wear process, Equation (2.11) , the evolution of worn surface profile and material loss can be predicted. In this section, an iterative simulation procedure is described which allows the numerical

prediction of rotary wear evolution.

2.2.1 Simulation algorithm

The iterative simulation is established based on the finite difference method. The continuous governing equation, Equation (2.11),is replaced with a discrete approximation by applying finite difference schemes to the derivatives with respect to time and space. The 1D domain $[R_1, R_2]$ is discretized into a grid of M elements (with $M+1$ nodes). The element dimension is $\Delta r = (R_2 - R_1)/M$ and the spatial location of the i^{th} node is $r_i = R_1 + (i-1)\Delta r$. The evolving surface is characterized by the surface height, z_i^n, of the worn profile at the position r_i, and after a rotational sliding angle, $n\Delta\theta$, with n as an iteration counter (equivalent to time counter). The wear rate is assigned to each node according to the material distribution, so that the modified rotary wear rate of the node at the position r_i is $(K_R)_i = K_i r_i$.

Given the surface profile at the n^{th} iteration, the surface profile after an incremental sliding angle, z^{n+1}, can be found by solving the following finite difference scheme based on the governing equation (2.11):

$$-P_0 = \frac{z_i^{n+1} - z_i^n}{(K_R)_i \Delta\theta} + k_s(z_i^n - < z^n >)$$
$$-k_g\left(\frac{z_{i+1}^n - 2z_i^n + z_{i-1}^n}{\Delta r^2} + \frac{1}{r_i}\frac{z_{i+1}^n - z_{i-1}^n}{2\Delta r} - < \frac{z_{i+1}^n - 2z_i^n + z_{i-1}^n}{\Delta r^2} + \frac{1}{r_i}\frac{z_{i+1}^n - z_{i-1}^n}{2\Delta r} >\right), \qquad (2.12)$$

where $z_0^n = z_2^n$ and $z_{M+1}^n = z_{M-1}^n$ are assumed according to the Neumann (zero slope) boundary conditions applied at the two boundary nodes. It is noted that the discretization scheme, Equation (2.12), is equivalent to the conventional iterative wear simulation procedure as shown in Figure 1.6, where the contact problem and wear calculation are realized

in two separate steps using (2.9) and (2.5). A discretization of Equation (2.9) allows for the estimation of contact pressure distribution corresponding to current surface profile, p_i^n:

$$p_i^n = P_0 + k_s(z_i^n - < z^n >)$$
$$-k_g\left(\frac{z_{i+1}^n - 2z_i^n + z_{i-1}^n}{\Delta r^2} + \frac{1}{r_i}\frac{z_{i+1}^n - z_{i-1}^n}{2\Delta r} - < \frac{z_{i+1}^n - 2z_i^n + z_{i-1}^n}{\Delta r^2} + \frac{1}{r_i}\frac{z_{i+1}^n - z_{i-1}^n}{2\Delta r} >\right). \quad (2.13)$$

Then the profile at the next iteration, z_i^{n+1}, is updated using the discretized version of Archard's wear equation (2.5):

$$z_i^{n+1} = z_i^n - p_i^n (K_R)_i \Delta\theta. \quad (2.14)$$

Combining the two calculation steps, Equation (2.13) and Equation (2.14) yields the same expression as the discretized governing equation (Equation (2.12)).

The cumulative material volume loss and instantaneous composite wear rate can also be calculated at each iteration during the simulation. The incremental volume loss caused by the n^{th} iteration is evaluated as:

$$\Delta V^n = 2\pi \sum_{i=1}^{M} I_i z_i^n r_i \Delta r, \quad (2.15)$$

where I represents the numerical integral coefficients that have a value of 0.5 at the two boundary nodes and a value of 1 at all intermediate nodes. Then the total material volume loss up to the n^{th} iteration is

$$V^n = \sum_{j=1}^{n} \Delta V^i. \quad (2.16)$$

The instantaneous composite wear rate at the n^{th} iteration, $K_{R,comp}$ (mm^3/N rad), is

defined as the incremental volume loss per area per average pressure per rotating angle:

$$K_{R,comp} = \frac{\Delta V^n}{|\Omega| P_0 \Delta\theta}. \tag{2.17}$$

2.2.2 Numerical results

In this section, a case study is presented to demonstrate the iterative rotary wear simulation. In this case study, the following parameters are assumed. The annular domain has an inner radius $R_1 = 4.24$ mm and an outer radius $R_2 = 12.7$ mm. The domain is discretized into $M = 100$ elements in the radial direction with $\Delta r = 0.0846$ mm. The constant applied normal force is set as $F_n = 40$N resulting in an average pressure of $P_0 = 0.089$ MPa. The Pasternak foundation parameters are chosen as $k_s = 0.307$ N/mm^3 and $k_g = 2.8$ N/mm according to the values used in [75]. Recall that in the foundation model described in Section 2.1.2, the compliant counter-body is composed of spring elements coupled with bending beam elements (with corresponding parameters k_s and k_g). A bi-material composite system, representative of common annular systems, consists of epoxy (material A) and aluminum (material B). The epoxy is typical of metallographic mounting epoxies and the aluminum is a standard 6061 type. The choice of constituent materials is for convenience in comparison to laboratory studies as well as demonstration of the capability of this model. Based on experimental measurements (see section 2.4), the wear rates are $K_a = 0.266$ mm^3/Nm for the less wear-resistant material (epoxy) and $K_b = 0.024$ mm^3/Nm for the more wear-resistant material (aluminum). The area fractions of material A and B are both 50%. The in-plane material distribution is shown in Figure 2.3, where material A (epoxy) is depicted in dark gray and material B (aluminum) is in light gray with corresponding wear rates K_a

and K_b.

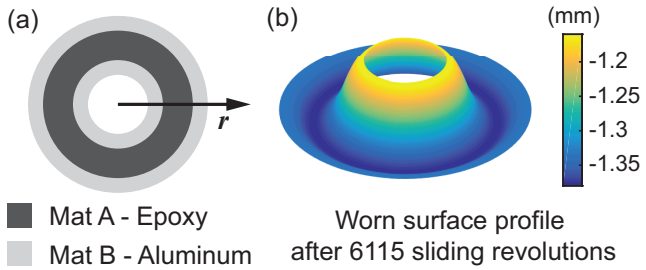

Figure 2.3: Schematic of the bi-material composite and worn surface profile. (a) In-plane material distribution. (b) Worn surface profile after 6115 sliding revolutions.

The simulation starts with initially planar composite surface, i.e. $z_i^0 = 0 (i = 1, 2, ..., M)$. The incremental rotating angle at each iteration is set as $\Delta\theta = 0.05$rad to ensure numerical stability and convergence. The evolution of worn surface profile and contact pressure for the composite surface is shown in Figure 2.4(a) at selected rotating revolutions, i.e. 0,100,500,1000,2000,4000,6000, and 6115 revolutions. Here, the number of computational iterations is converted to number of revolutions between rotating surfaces where one revolution is 2π.

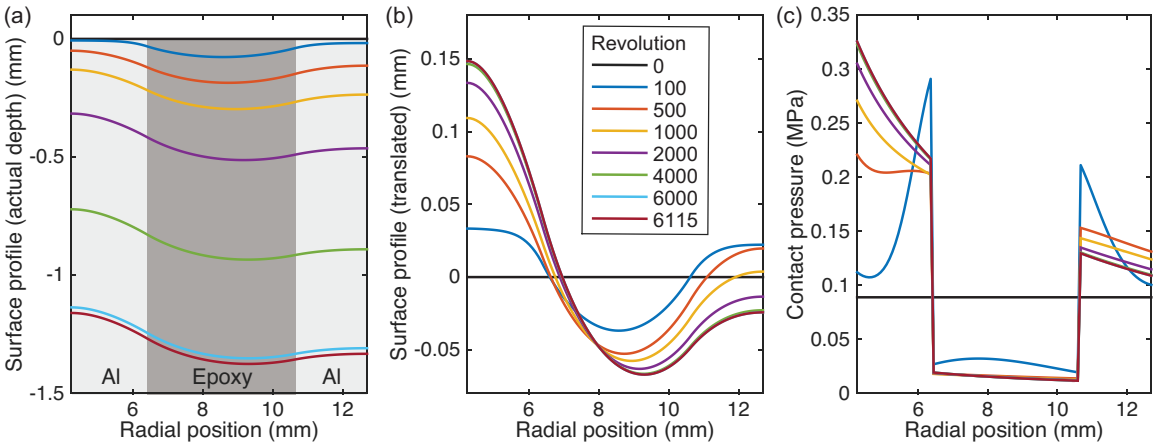

Figure 2.4: Evolutions of worn surface profile and contact pressure distribution. (a) Worn surface profiles at selected sliding revolutions in actually depth. (d) Translated worn surface profiles. (e) Contact pressure evolution.

Figure 2.4 shows the the worn surface and contact pressure distribution along the radial

direction. The worn surfaces are plotted at the exact depths in Figure 2.4(a). The worn surface is recessing and the initially planar surface becomes non-planar as the wear process proceeds. In order to better visualize and cmopare the evolving worn profiles, the profiles in Figure 2.4(a) are all translated to zero-level (with average value of zero) as shown in Figure 2.4(b). It is noticed that, from initialization to 1000 revolutions, the surface undergoes dramatic change in its shape. The worn surface gradually forms a shape that has a low valley in the center occupied by material A (epoxy) and two peaks along the boundaries occupied by material B (aluminum). This dramatic change is also observed in the contact pressure distribution in Figure 2.4(a). At 100 revolutions, high pressure peaks appear near the material interfaces, which are vanishing as the rotating revolution increases. Both the worn surface profile and contact pressure distribution gradually stabilize after 4000 revolutions. It is seen that the surface profiles as well as the contact pressure distributions at 6000 revolutions and 6115 revolutions are almost identical.

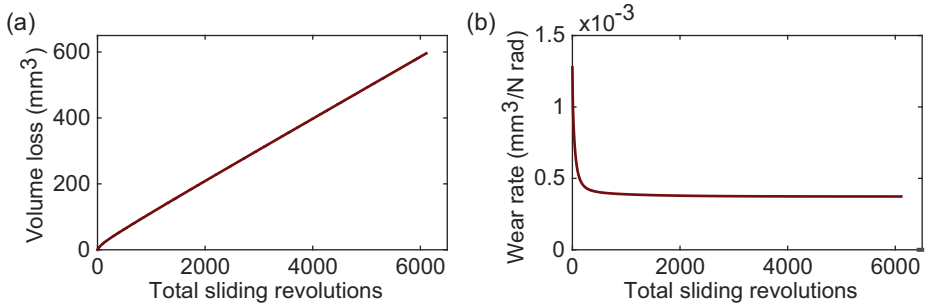

Figure 2.5: History of material volume loss and instantaneous composite wear rate (markers denote the onset of steady-state). (a) Volume loss vs sliding distance. (b) Instantaneous composite wear rate vs sliding distance.

The incremental volume loss is calculated at each step using Equation (2.15). The instantaneous composite wear rate is calculated as the incremental volume loss divided by the product of applied normal force and the incremental rotating angle as Equation (2.17). The accumulated total volume loss and the instantaneous composite wear rate are plotted

against total rotating revolutions in Figure 2.5. Since the normal force and the incremental rotating angle is kept constant, the value of the instantaneous composite wear rate reflects the slope of the total volume loss curve. In general, the total volume loss increases as the rotating revolution increases while the increasing rate is decreasing. The curve gradually becomes an almost linear line. This trend is also reflected in the instantaneous composite wear rate curve. The instantaneous composite wear rate experiences a steep decline at the beginning and converge to a lower constant value.

It is seen that, the evolution of the worn surface profile, contact pressure distribution, volume loss, and instantaneous composite wear rate follow the common trend: dramatic changes (in shape and increase/decrease in number) happen during the initial transient state until a stabilized state is reached. This evolving trend is consistent with the commonly observed wear processes where two wear regimes can be distinguished: run-in wear and steady-state wear.

2.3 Prediction of steady-state wear

The case study in Section 2.2 demonstrates the capacity of the iterative wear simulation algorithm to predict the evolution of key features during the rotary wear process. Transition from the initial run-in wear stage to the steady-state wear stage has been observed from the evolution of the worn surface profile, contact pressure distribution, volume loss, and instantaneous composite wear rate. In this section, a steady-state condition is introduced to the iterative wear simulation to characterize run-in and steady-state wear stages. In addition, a direct method to determine the steady-state wear performance is derived from the PDE system governing the rotary wear process (Equation (2.11)).

2.3.1 Iterative simulation with steady-state condition

It is observed from the previous case study that, after steady-state is reached, after around 6000 rotating revolutions, the worn surface profile reaches a constant shape corresponding to a steady contact pressure distribution and the volume loss increases linearly as the rotation angle increases corresponding to a constant instantaneous composite wear rate. The worn surface profile reaches a constant shape that keeps recessing at a constant rate as wear proceeds. Therefore, in the iterative simulation, steady-state is reached when the difference of the local incremental worn depth at two successive increments are equal at every point within the sliding interface. The wear depth change at a particular position, r_i, between the n^{th} and $(n+1)^{th}$ iterations is, $\Delta z_i^n = z_i^{n+1} - z_i^n$. The steady-state condition can be established as:

$$\max \frac{|\Delta z_i^{n+1} - \Delta z_i^n|}{|\Delta z_i^n|} < \epsilon, \tag{2.18}$$

where ϵ is a small constant chosen according to desired level of precision (e.g. 1×10^{-8}). By incorporating the steady-state condition into the wear simulation algorithm introduced in Section 2.2, the transition from run-in wear stage to steady-state wear stage can be detected after the iterative simulation is run for sufficient iterations.

2.3.2 Direct method for steady-state wear prediction

Alternatively, the steady-state profile can also be directly calculated from initial conditions and material and system properties. As it is often the steady-state performance that is of interest for optimization purposes, computing intermediate states is inefficient. Here a direct method is developed to compute the steady-state surface profile directly from the

initial material distribution.

The derivation of the direct method is based on the characteristic that at steady-state, the surface profile converges to a constant shape that continues to recess without further changes in shape. Moreover, it keeps its shape while recessing at a constant rate. Assuming that the steady-state profile is $u(r)$ and that it recesses at the rate of α, the steady-state profile, $\tilde{z}$, can be expressed as:

$$\tilde{z}(\theta, r) = -P_0 \alpha \theta + u(r). \tag{2.19}$$

It should be noted that $\tilde{z}$ satisfies the governing equation (2.11) only after the system reaches steady-state, when $z(\theta, r) = \tilde{z}(\theta, r)$ is true. In contrast, during the transient run-in process, the surface profile is continuously changing and cannot be described by $\tilde{z}$. The rest of this section is focused on steady-state performance. Substituting Equation (2.19) into the governing wear equation (2.11) gives:

$$-P_0 \frac{\alpha}{K_R} + k_s(u - < u >) - k_g \nabla^2 u = -P_0. \tag{2.20}$$

By taking the average of each side of Equation (2.20), one can analytically determine the constant rate that the steady-state surface profile is recessing at:

$$\alpha = < K_R^{-1} >^{-1} . \tag{2.21}$$

This constant rate can be interpreted as a height loss per average pressure per rotating angle at steady-state, which is the same as the steady-state composite wear rate, $\alpha = K_{R,comp}^{ss}$.

Thus, the steady-state profile, u, is found from:

$$k_s(u - < u >) - k_g \nabla^2 u = -P_0 + P_0 \frac{< K_R^{-1} >^{-1}}{K_R}, \tag{2.22}$$

by letting $u_0 = u - < u >$ and applying the boundary conditions. In this way, the steady-state surface profile of a given rotary wear system can be directly predicted by solving the following system of equations for u_0:

$$\begin{cases} k_s u_0 - k_g \nabla^2 u_0 = -P_0 + P_0 \frac{< K_R^{-1} >^{-1}}{K_R}, \quad r \in (R_1, R_2), \\ \frac{\partial u_0}{\partial r} = 0, \quad \text{at } r = R_1 \text{ and } r = R_2. \end{cases} \tag{2.23}$$

It is noted that the right-hand-side of the above equation is only dependent on the piece-wise distribution of the function, K_R, and the ratio between the wear rates of the two constituent materials, K_a/K_b. As a result, for composite systems consisting of different pairs of materials with the same wear rate ratio and the same in-plane distribution, under the same wear conditions (counter-body and applied load), the steady-state profiles of these composite systems will be the same.

This ordinary differential equation (ODE) system (2.23) can be solved using a finite difference method. The discretization of the 1D domain is the same as for the iterative method (section 2.2.1). Then the finite difference scheme of the above governing equation for the steady-state surface profile, u_0, at the interior nodes, is:

$$k_s u_{0,i} - k_g \left(\frac{u_{0,i+1} - 2u_{0,i} + u_{0,i-1}}{\Delta r^2} + \frac{1}{r_i} \frac{u_{0,i+1} - u_{0,i-1}}{2\Delta r} \right) = -P_0 + P_0 \frac{< K_R^{-1} >^{-1}}{(K_R)_i}. \tag{2.24}$$

Considering Neumann (zero slope) boundary conditions, we have the following equalities

for the two fictitious boundary nodes: $u_{0,0} = u_{0,2}$ and $u_{0,M+1} = u_{0,M-1}$. The steady-state profile, u_0, is then found by directly solving this linear equation system.

2.3.3 Numerical results

In this section, numerical results of three bi-material composites subject to rotary wear are presented. As shown in Figure 2.6, the three bi-material composites have the same material volume fractions but different in-plane distributions. In Case 1, the more wear-resistant material, aluminum (material B), is distributed at the outer edges and the less wear-resistant material, epoxy (material A), is concentrated inside. Case 3 has the opposite distribution, compared to Case 1. Case 2 has epoxy, the less wear-resistant material, distributed between two layers of aluminum, the more wear-resistant material.

Figure 2.6(a) plots the resultant volume loss as a function of total sliding revolutions. Figure 2.6(b) shows the evolution of composite wear rate with increasing sliding revolutions. Note that in Figure 2.6(a) and Figure 2.6(b), the data point denoted by a star for Cases 1-3, represents the value at convergence when the steady-state condition, $\epsilon = 10^{-8}$, has been met. Thus it is seen that Case 1 converges before Case 2 or 3. Figure 2.6(c) gives the contact pressure distributions at steady-state. In Figure 2.6(d), the surface profiles of Cases 1-3 after 6115 revolutions, when all three cases have reached steady-state are shown.

The steady-state surface profiles calculated using the direct method are also plotted in Figure 2.6(d). Since the direct method only determines the shape of the steady-state surface profile, these steady-state profiles are translated the same average depth level as the actually worn surface profiles for all three case. It is seen that, for each case, the directly calculated shape of the steady-state surface profile coincides with the worn surface profile

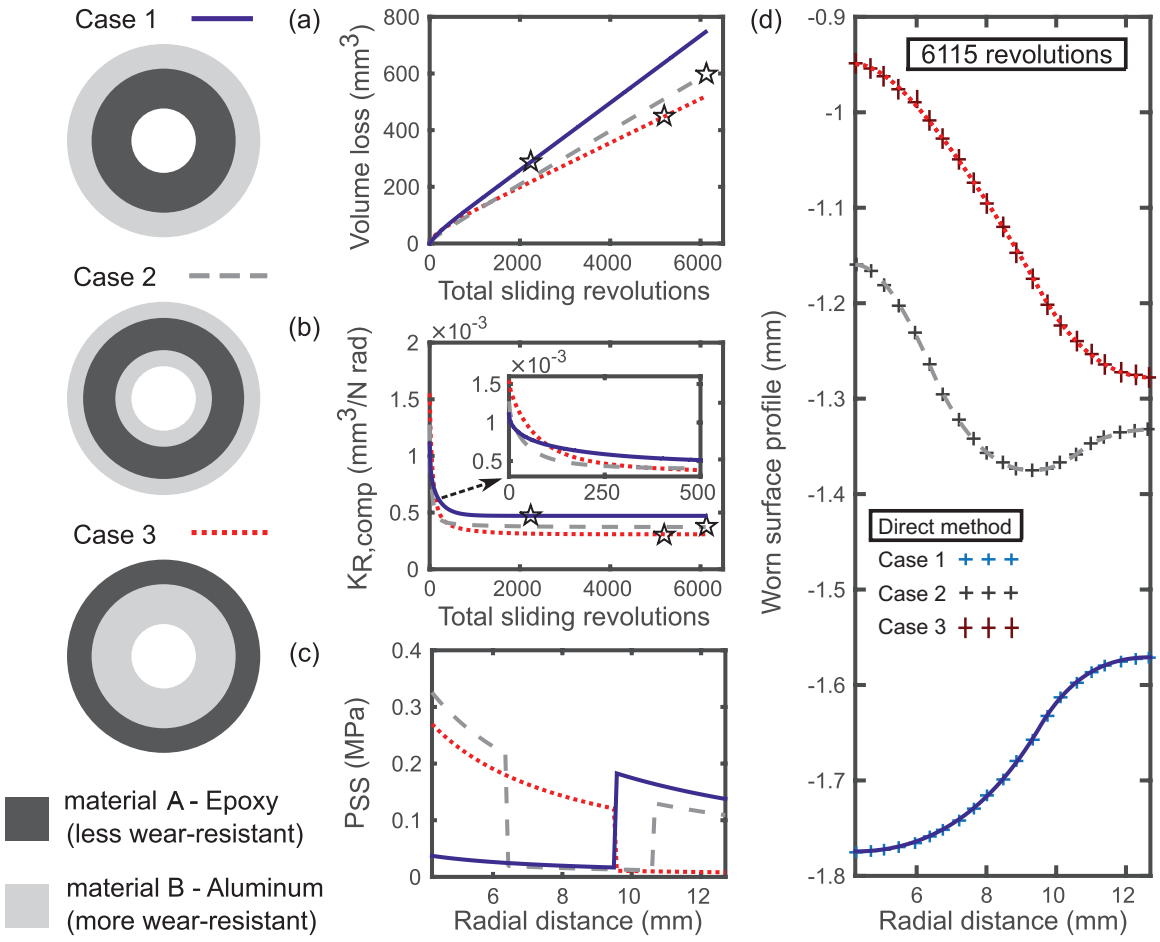

Figure 2.6: Comparison of three material distributions with the same area fraction ($|\Omega_a| = |\Omega_b| = 0.5|\Omega|$). (a) Volume loss versus total sliding revolutions. (b) Instantaneous composite wear rate versus total sliding revolutions. (c) Steady-state contact pressure distributions. (d) Worn surface profiles after 6115 revolutions. Note that in Figure 2.6a and Figure 2.6b, the data point denoted by a star for Cases 1-3, represents the value at convergence when the steady-state condition, $\epsilon = 10^{-8}$, has been met.

from the iterative simulation after steady-state is reached. Table 2.1 displays the steady-state composite wear rate values obtained from direct calculation using Equation (2.21) and from the converged iterative simulation after 6115 revolutions. Both methods give the same steady-state composite wear rate values for all three cases. The good agreement demonstrate the equivalence of the iterative simulation with steady-state condition and the direct method in predicting the steady-state wear performance, i.e. worn surface profile and composite wear rate.

	Steady-state composite wear rate [mm^3/(Nrad)]		
	Case 1	Case 2	Case 3
Iterative method	0.47e-3	0.37e-3	0.31e-3
Direct method	0.47e-3	0.37e-3	0.31e-3

Table 2.1: Comparison of steady-state composite wear rates, $K^{ss}_{R,comp}$ [mm^3/(Nrad)].

2.3.4 Calculation of steady-state composite wear rate

It may seem intuitive that in order to minimize material loss, the more wear-resistant material (which has a smaller value of wear rate) should be distributed at the outer edges of the specimen to accommodate the longer sliding distances. However, numerical results from the previous section show the opposite trend. It is seen in Figure 2.6(b) that the steady-state composite wear rate of Case 1 (which has the intuitive design) is the largest among the three cases considered. The steady-state composite wear rate for Case 3 is the smallest and Case 2 has an intermediate steady-state composite wear rate. The implication is that Case 1 (which might be thought optimal by intuition) will eventually lose more material than Case 2 and Case 3 because of its larger steady-state composite wear rate. It can be seen from Figure 2.6(d) that the surface of Case 1 is at the lowest level and the surface of Case 3 is at the highest level, which implies that after a long sliding process, Case 1 loses the most material while Case 3 loses the least material among the three cases considered. Thus, it is found that for given volume fractions of materials with different wear rates, distributing the less wear-resistant material at the outer annular edges and the more wear-resistant material at inner annular locations leads to the minimal value of steady-state composite wear rate. In this section, an analytical proof of this counter-intuitive finding is presented based on the direct steady-state solution given in Section 2.3.2.

The analytical steady-state composite wear rate determined for a given material distribution derived in Equation (2.21) can be calculated as:

$$K^{ss}_{R,comp} =< K_R^{-1} >^{-1}= \left(\frac{\int_0^{2\pi} \int_{R_1}^{R_2} (K(r)r)^{-1} r dr d\theta}{\int_0^{2\pi} \int_{R_1}^{R_2} r dr d\theta} \right)^{-1} = \frac{R_2^2 - R_1^2}{2} \left(\int_{R_1}^{R_2} K^{-1}(r) dr \right)^{-1}. \tag{2.25}$$

Minimizing the steady-state composite wear rate, $K^{ss}_{R,comp}$, is equivalent to maximizing the integral $\int_{R_1}^{R_2} K^{-1}(r)dr$. As the wear rate, $K(r)$, is a piecewise constant function dependent on the radial position when the material distribution is rotationally symmetric, the integral can be re-written as:

$$\int_{R_1}^{R_2} K^{-1}(r)dr = K_a^{-1} L_a + K_b^{-1} L_b, \tag{2.26}$$

where L_a and L_b represent the total radial "thickness" of the domains occupied by material A and material B, respectively:

$$L_a = \int_{R_1}^{R_2} \delta(r)dr, \text{ and } L_b = \int_{R_1}^{R_2} 1 - \delta(r)dr, \tag{2.27}$$

where $\delta(r)$ is also a piecewise constant function satisfying:

$$\delta(r) = \begin{cases} 1, & if\ K(r) = K_a, \\ 0, & if\ K(r) = K_b. \end{cases} \tag{2.28}$$

A geometric representation of this radial "thickness" is shown in Figure 2.7. In Figure 2.7a, two annular domains with the same area ($|\Omega_1| = |\Omega_2|$) and made of the same single material are shown. The radial thickness for the annulus on the left is smaller than that on the right, $L_1 < L_2$. In Figure 2.7b, the same Cases 2-3 from Figure 2.6 are reproduced

in order to demonstrate the corresponding radial thickness for material B. In Case 2, there are two layers of material B with radial "thicknesses", L_{b1}^{Case2} and L_{b2}^{Case2}, and one layer of material A with radial "thickness", L_a^{Case2}. The total radial "thickness" of material B for Case 2 is $L_b^{Case2} = L_{b1}^{Case2} + L_{b2}^{Case2}$. The whole annular domain is occupied by materials A and B, so L_a and L_b must satisfy:

$$L_a + L_b = R_2 - R_1. \tag{2.29}$$

Then Equation (2.26) can be expressed as a function of L_b:

$$\int_{R_1}^{R_2} K^{-1}(r)dr = K_a^{-1}(R_2 - R_1) + (K_b^{-1} - K_a^{-1})L_b. \tag{2.30}$$

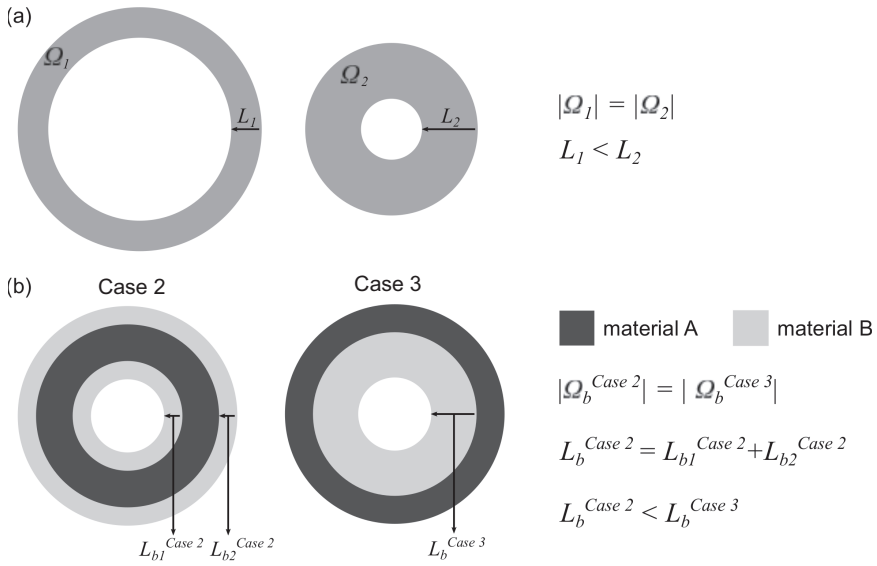

Figure 2.7: Explanation of "radial thickness". (a) Comparison of radial thicknesses of two annuluses with the same area. (b) Comparison of total radial thicknesses of material B for Case 2 and Case 3 from Figure 2.6.

Recall that to minimize the steady-state composite wear rate, $K_{R,comp}^{ss}$ (Equation (2.25)), the integral $\int_{R_1}^{R_2} K^{-1}(r)dr$ must be maximized. For systems where material A is less wear-

resistant than material B, $K_a > K_b$ then $(K_b^{-1} - K_a^{-1}) > 0$, and the above integral is monotonically increasing with L_b. Thus the maximum value of L_b will result in the minimum value of the steady-state overall wear rate $K_{R,comp}^{ss}$, for given volume fractions of material A and B. As shown in Figure 2.7a, for annuli Ω_1 and Ω_2, with the same area, the radial "thickness", L_2, is larger than the radial "thickness", L_1, because of the smaller inner radius of the annulus. Thus, as shown in Figure 2.7b, for a given amount of the more wear-resistant material (material B), the optimal placement of material B is the placement that allows for the maximum L_b (i.e. the more wear-resistant material should be distributed at the inner annulus edge, see Case 3). Then, in general, based on the proposed wear model with Neumann boundary conditions: *for fixed area fractions of bi-material systems with different wear rates, all of the more wear-resistant material should be concentrated at the annulus center in order to minimize the steady-state composite wear rate.*

2.4 Experimental evaluation

In the previous section, numerical predictions of composites subject to rotary wear are presented which demonstrate the utility of the established rotary wear model and simulation procedure. Optimal design to minimize the steady-state composite wear rate of systems with fixed material volume fractions are also identified. The optimal design is not intuitive in that, the more wear-resistant material should be concentrated near the inner edges with the less wear-resistant material placed outside. In order to demonstrate and support the numerical results, a series of preliminary experiments have been conducted to evaluate the established wear modeling and simulation framework. These wear experiments were conducted by Mr. Tomas Grejtak from the Tribology Laboratory at Lehigh University; I helped

to direct the experimental setup, decide relevant parameters, and interpret experimental data.

2.4.1 Experimental setup and methods

In the absence of relevant wear testing standards for the systems of interest, wear tests were conducted on a purpose-built rotary reciprocating. Wear systems with the thrust washer geometry shown in Figure 2.1 are investigated. Specimens composed of epoxy (metallographic mounting epoxy) and aluminum (6061) were used to experimentally obtain wear rates, volume losses, and worn surface profiles. The surface consisted of 50% aluminum and 50% epoxy with material distributions for Cases 1, 2 and 3 as described in Figure 2.6. The aluminum base was machined with a CNC mill and lathe corresponding to the Cases 1, 2 and 3. The void spaces were filled with epoxy resin and cured. The specimens were then machined to ensure flat initial surfaces. A counter-body system comprised of a polydimethylsiloxane (PDMS) pad (6mm thick) and an abrasive paper was used as an abrasive counter specimen. The PDMS pad, Sylgard® 184, was made with a 10:1 ratio of elastomer to cross-linker. The elastic modulus of this pad is 1.8 MPa and the corresponding calculated foundation parameters k_s and k_g are 0.307 N/mm^3 and 2.8 N/mm respectively [75]. Silicone carbide abrasive paper grit 400 (Norton Black Ice T214) was placed on the surface of the PDMS pad and clamped to the load cell of a tribometer (see Figure 2.8).

A purpose-built rotary reciprocating thrust-washer tribometer was used to perform the wear tests. The specimens were mounted to a collet chuck which was connected to a motor that provided rotary reciprocation (Figure 2.8). A compliant system of abrasive paper and PDMS pad was mounted on the load cell and loaded against a specimen. A constant load of

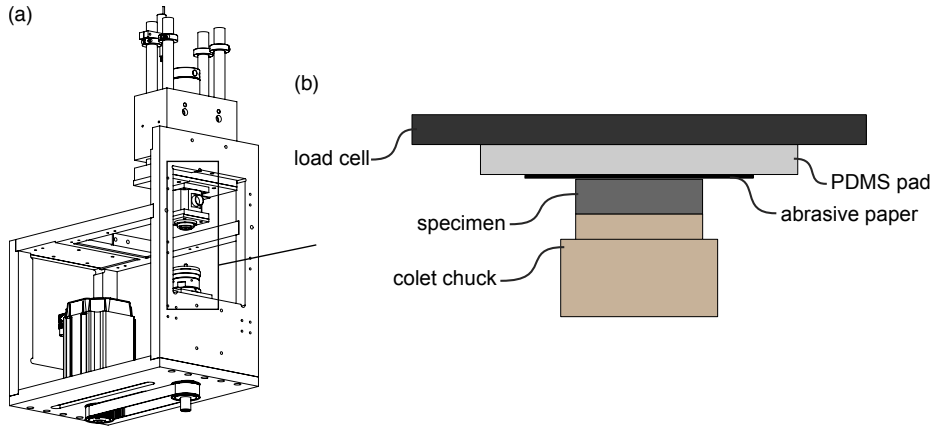

Figure 2.8: Schematic of rotary tribometer used for experiments. (a) Assembly view of the instrument. (b) Schematic of interface between multi-material composite specimen and the PDMS-backed abrasive paper counterspecimen.

40 N and an angular velocity of 0.6366 rev/s was applied throughout all measurements. One cycle was assumed to be a 360° clockwise (CW) and then 360° counter-clockwise (CCW) motion, resulting in 2 revolutions per cycle. Compressed air was used to blow off debris from the surface of the worn specimen before the abrasive paper was changed (after every 20 revolutions (10 cycles)). The abrasive paper was changed due to the accumulated wear debris between the specimen and the abrasive paper. The composite specimen was weighed after every 100 revolutions to determine the mass.

The worn surface profile was measured with a Bruker® Contour GT SWLI machine (using scanning white light interferometry). The profile evolution was measured for the originally flat unworn surface and after 200, 600, 1000, 2000 and 4000 revolutions. A surface profile was created by stitching together multiple scans across the surface of the specimen in one direction resulting in a surface height map. Additional details related to surface microstructure are not reported here as they are beyond the scope of this work where models are presented and evaluated at the macro or continuum scale. The experimental procedure used here is similar to other *linear* wear tests that have been previously reported [78, 79]

where the dominant wear mechanism is unlubricated abrasive sliding wear. These have included studies focused on the detailed surface chemistry and evolving microstructure of composites.

The wear rates of aluminum and epoxy were measured on a linear reciprocating tribometer using the same compliant counter specimen, loading, and sliding conditions as the conditions used for testing the composite specimen described above. A square shaped surface with dimensions of 20×20 mm was loaded against a compliant counter specimen also composed of PDMS and an abrasive paper to a normal load of 40 N. The sliding velocity and sliding stroke were set to 50.8 mm/s and 25.4 mm, respectively. Again, after every 10 cycles the abrasive paper was changed and after every 100 cycles the specimen was weighed to find the mass. This process was repeated for 1000 cycles. From the obtained mass loss, m_{loss} (mg), and the density of the material, ρ (mg/mm^3), the volume loss, V_{loss} (mm^3) was calculated as:

$$V_{loss} = \frac{m_{loss}}{\rho}. \tag{2.31}$$

This volume loss, the constant force, F_n (N), and sliding distance, s (m), were then used to calculate the wear rate, K (mm^3/Nm):

$$K = \frac{V_{loss}}{F_n s}. \tag{2.32}$$

Determination of the wear rate and volume loss of a composite material can be quite challenging. Volume measurements are generally made in one of two ways: indirectly by mass loss or directly with a volume measurement (e.g. profilometer or other dimensional measurement). Both methods are challenging in the case of a multi-material thrust-washer.

Non-uniform height loss and density precludes mass-based wear measurement. Due to the lack of a true reference height, because the entire surface is wearing, profilometry is also difficult. Here, the two methods are combined. A profilometer is used to measure the surface profile ($z_{profile}$). The absolute height of the specimen cannot be measured with appropriate fidelity; thus, it is determined using mass measurements. By knowing the outer surface profile and density distribution of the specimen, the volume can be specified. The initial surface height is defined as $z_{profile,0} = 0$; the worn surface profile, $z_{profile}(r)$, is defined as the scan profile, z_{scan} (with max value set to 0) plus a reference offset height (z_{ref}) to account for the global wear of the surface. Volume (V) can be calculated as the integral of the worn surface profile ($z_{profile}(r)$):

$$V_{loss} = \int_0^{2\pi} \int_{R_1}^{R_2} z_{profile} r dr d\varphi = \int_0^{2\pi} \int_{R_1}^{R_2} (z_{scan} + z_{ref}) r dr d\varphi. \tag{2.33}$$

The unknown reference, z_{ref}, can be solved for using mass loss measurements. Mass is the integration of the worn height times the piecewise constant density, $\rho(r)$, over the whole material domain:

$$m_{loss} = 2\pi \int_{R_1}^{R_2} (z_{scan} + z_{ref}) \rho(r) r dr. \tag{2.34}$$

Using Equation (2.34), z_{ref} was numerically determined and used to calculate the worn volume with Equation (2.33). From the worn volume, the rotary wear rate, K_R, is calculated as:

$$K_R = \frac{V_{loss}}{F_n \theta}, \tag{2.35}$$

where θ is the total rotating angle.

2.4.2 Comparison of experimental results and numerical predictions

In Figure 2.9, experimentally measured surface profiles, mass loss and volume loss are compared to the numerical predictions for three bi-material rotary systems. The repeatability of the results was ensured using multiple specimens under the procedures described above. Each rotary system has a different in-plane material distribution, but the same volume fraction ($|\Omega_a| = |\Omega_b| = 0.5|\Omega|$, 50% Aluminum area fraction for all three cases). Case 1 has epoxy placed at the inner edges and aluminum at the outer edges (Figure 2.9(a)). The material distribution in Case 3 (Figure 2.9(c)) is the opposite to the one in Case 1. In Case 2, epoxy is placed in between two layers of aluminum that are distributed along the inner and outer edges (Figure 2.9(b)). The experimental results support the counterintuitive numerical results (Section 2.3.4), where the optimal design has the more wear-resistant material placed near the inner edges and the less wear-resistant material placed outside (as Case 3).

In Figure 2.9 (d-f), the experimentally worn surface profiles are compared to the numerically predicted surface profiles for Cases 1-3, respectively. The numerical model produces worn surface profiles with comparable features to the experimentally measured worn surface profiles. However, there are differences, most notably at the inner and outer radial boundaries; this points to the importance of boundary conditions in the numerical model. Figure 2.9(g) shows that the numerically and experimentally measured incremental mass loss per (N rad) is the largest in Case 1, smallest in Case 3, and intermediate in Case 2. Beyond 3000 revolutions, as the wear approaches steady-state, the experimentally measured incremental mass loss converges with the numerical predictions. In Figure 2.9h and Figure 2.9(i), the numerically predicted volume loss and composite wear rates from Section 2.3.3

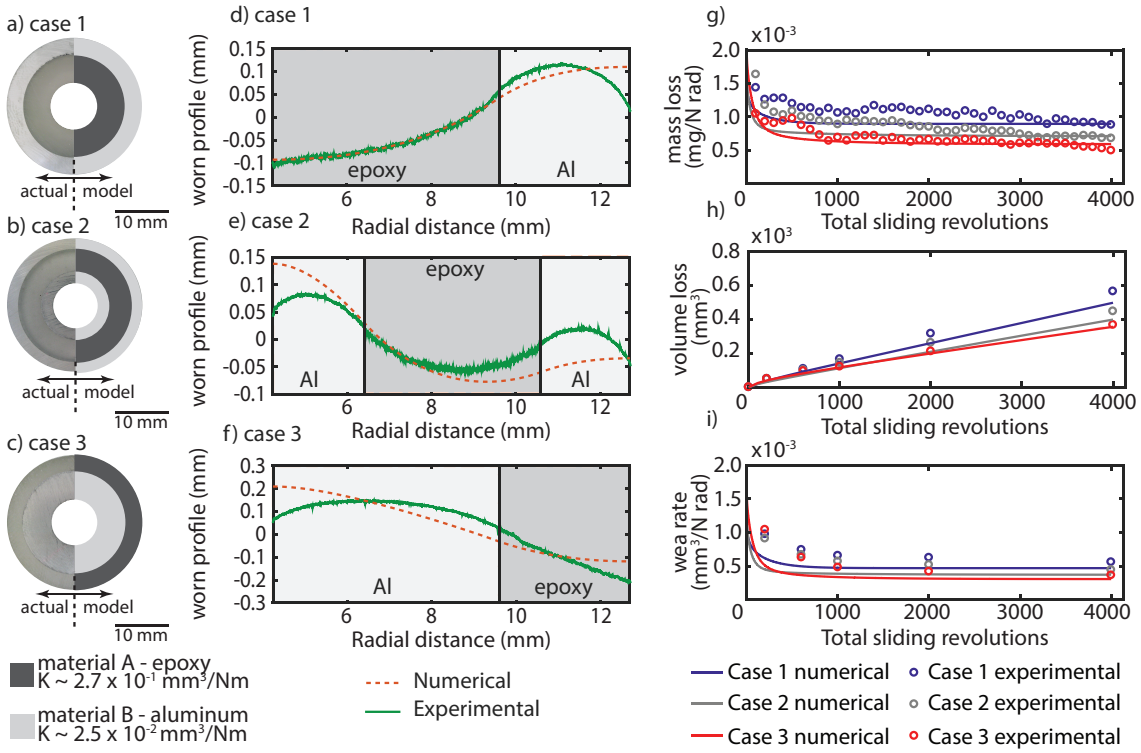

Figure 2.9: Results from rotary wear experiments. (a-c): Design Cases 1-3. *On the left*, an optical photo of one-half of the top surface of the fabricated real test specimens. *On the right*, the corresponding schematic material distributions in the numerical model. (d-f): Worn profiles approaching steady-state (4000 revolutions) as a function of radial distance (all profiles are translated to the same depth level for comparison). (g) Incremental mass loss, (h) accumulated volume loss and (i) composite rotary wear rate throughout the sliding process. Both numerical and experimental results are compared in (d-i).

are compared to the experimentally calculated volume loss and composite wear rates as described above. Figure 2.9(h) shows that the volume loss history has the same trend in the experimental and numerical results. After reaching steady-state, Case 1 has the highest volume loss but Case 3 has the lowest and Case 2 has the intermediate volume loss. Consequently, the composite wear rate, shown in Figure 2.9(i), is the highest in Case 1, the lowest in Case 3 and intermediate in Case 2.

Similar trends of wear development for all three cases have been observed in the numerical predictions and experimental measurements. There are still differences between the experimentally measured and numerically predicted results. It is most noticeable in Figure

2.9(g) and 2.9(i), where the experimentally measured mass loss and composite wear rates are higher than numerical predictions at the early and intermediate sliding revolutions ($\sim$200 to 1000). This difference is also reflected in the larger total volume loss from experimental measurements. One primary cause for these differences is the simplification of boundary conditions in the analytical model. Neumann boundary conditions (zero slope) were applied at the inner and outer edges of the composite surface in the model. One consequence is that the contact pressure depends only on local and nearest neighbor topography within the contact area (annulus domain). However, in the experimental setup, the fully compliant counter-body, a PDMS pad with an abrasive paper on top of it, is much larger than the specimen. The specimen is punched into the counter-body, which causes the deformation of the whole counter-body not only the area in contact. So the contact pressure calculation should be related to the surface deflection of the whole counter-body, especially the area near the boundaries of the contact area. This is why there is a rise and a drop at the boundaries of the surface profiles in Figure 2.9 (d-f), especially noticeable for the specimens that have aluminum at the boundaries (Figure 2.9(e-f)). These non-monotonic shapes are actually expected as they correspond to the high pressure peaks near edges in flat-ended punch problems [80] (Figure 2.4(c)). Modeling improvement could be made by exploring the effects of boundary conditions. The parts of the counter-body that are not in contact with the specimen may also be considered explicitly in the contact pressure calculation.

2.5 On achieving target surface profiles

With the rotary wear models and prediction methods described in Section 2.2 and Section 2.3 and experimental support in Section 2.4, several opportunities for optimization and the

identification of design rules are present. Objectives of interest may include minimizing material loss during the wear process for economic and energy-saving reasons, or achieving target worn surface or pressure profiles for specific uses. It has been shown elsewhere that sliding interfaces with appropriate texture and dimensions can reduce friction and improve sealing efficiency and load capacity [81, 82]. In the following, a range of target surface profiles is explored.

Recall the governing equation (2.23) for the steady-state surface profile that evolves from a known initial material distribution (wear rate distribution). Looking at the right-hand-side of Equation (2.23), the term, $\frac{<K_R^{-1}>^{-1}}{K_R}$ represents the ratio between the steady-state composite wear rate and the local rotary wear rate and it is only dependent on the ratio between the wear rates of the two constituent materials, K_a/K_b. The consequence is that, for wear systems consisting of two materials with the same wear rate ratio, the steady-state profiles of these systems will be the same. Moreover, the material distribution (wear rate distribution) that would correspond to the prescribed target steady-state profile, u_0, can be found directly from Equation (2.23). It is important to note that the solution will give the *relative* wear rate distribution in the design domain. If the wear rate is distributed in a piecewise constant function, the solution corresponds to a discrete material distribution, with a known wear rate ratio between the constituent materials. If the wear rate distribution has continuous changes in the design domain, the corresponding material distribution is graded with a variation in composition or structure, and a known ratio between the wear rate at any location in the domain and the minimum wear rate value.

Figure 2.10 presents some target surface profiles that are used to demonstrate the potential and range of the approach: (a) an arbitrary profile, (b) a flat surface, and (c) a cosine

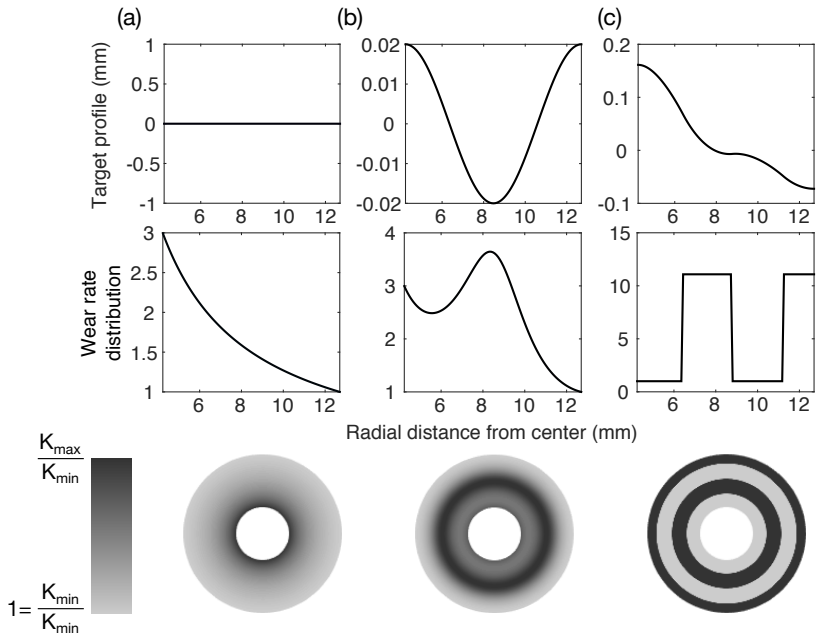

Figure 2.10: Material distributions for target surface profiles showing relative wear rate distribution.

function shape. These examples demonstrate a broad range of potential profiles of interest for tribological applications. For Figure 2.10 (a-c), the plots on the left show the three different target steady-state surface profiles. The plots in the middle column show the wear rate distributions along the radial direction to achieve these target profiles. The vertical axis of these plots represents the relative wear rate; it is normalized by the minimum value, K/K_{min}. The corresponding 2D wear rate distributions are shown in the annular domains on the right. As shown in Figure 2.10(a), the arbitrary target profile can be achieved by distributing two materials in the shown configuration with a specific and discrete wear rate ratio. In the previous sections, only composite systems consisting of two materials with distinct wear rates are considered, resulting in a wear rate distribution that is piecewise constant. It should also be noted that not all steady-state surface profiles of interest have corresponding discrete wear rate distributions. In Figure 2.10(b), the target steady-state profile is flat. The corresponding relative wear rate distribution is proportional to $1/r$ with

the lowest value normalized to 1. This result is expected because the rotary wear rate K_R is then constant over the domain, which is equivalent to a uniform material distribution. And surfaces with uniform material distributions will be worn to a flat surface if Neumann (zero slope) boundary conditions are assumed. With traditional manufacturing processes, this kind of graded material distribution is difficult to produce. However with newly developed additive manufacturing techniques, the possibilities to manufacture graded material distributions that meet the design specifications continue to emerge [83–87]. Another example of an optimal graded material distribution is shown in Figure 2.10(c), with a target steady-state profile of a cosine function shape. It should be noted here that these graded material distributions are still relevant for traditional manufacturing processes. By applying appropriate filtering techniques for post-processing, the graded distributions can be forced towards discrete bi-/multi-material distributions.

2.6 Summary

A rotary wear model that couples Archard's wear equation and the Pasternak foundation model has been developed for the rotary abrasive sliding wear of composites. The wear evolution predicted by the iterative simulation exhibits realistic transition from run-in to steady-state wear regimes. A direct method for steady-state wear performance is used to identify counter-intuitive bi-material designs that minimize their steady-state composite wear rates. This method is also used to provide proof-of-concept for the design of composites with target steady-state surface profiles. It is shown that the rotary steady-state composite wear rate depends on both the area fraction of constituent material and the in-plane material distribution. For rotationally symmetric bi-material composites with fixed material area

fractions, it is surprising that steady-state composite wear rates always reach minimum values when placing the more wear-resistant material (having the smaller wear rate of the two constituents) towards the inner radius and the less wear-resistant material at the outer annulus edges. This counterintuitive optimal design solution has been generally validated by experiments. Nevertheless, some discrepancies between predicted and experimentally measured worn surface profiles are noticeable especially near the inner and outer edges which is due to the assumption of Neumann boundary conditions on the surface profile. This will be further investigated and improved in the next chapter.

Chapter 3

Wear model improvements

This chapter focuses on improving the predictive accuracy and physical relevancy of the foundation-based wear models. Often mathematically convenient periodic or explicit boundary conditions are chosen, while produce discrepancies with experimental measurements. In this chapter, a generalized wear model and simulation framework is developed for both rotary and linear wear systems. An implicit treatment of boundary conditions is proposed by taking both the contact and non-contact regions on the counter-body into account. In addition, an asymmetric elastic foundation model is proposed to better capture experimentally observed non-symmetric worn surface profiles that develop during linear reciprocating or unidirectional wear. Instead of the typical guesses or adoption of legacy foundation parameters (impossible/difficult to directly measure), an optimization routine is developed to calibrate the underlying foundation parameters using experimentally measured steady-state worn surface profiles. Comparison between model predictions and experimental measurements is made to validate the improved wear model.

3.1 Improved wear model and simulation procedure

In this section, the wear model is formulated within a generalized framework that can be applied for single or multi-material composites in both rotary and linear wear systems. In the case of linear reciprocating or unidirectional sliding, the model includes the possibility for asymmetry with respect to sliding direction.

3.1.1 Generalized wear model formulation

The generalized wear model is built based on Archard's wear equation (Equation (1.1)) and the elastic foundation model. Archard's equation is applied on a local scale as:

$$\Delta z = -PKv\Delta t, \tag{3.1}$$

where P is the local contact pressure, v is the local sliding velocity, and z represents the height of the worn surface. The incremental wear depth, Δz, is proportional to the local material wear rate, local contact pressure, and local sliding velocity after a time increment Δt.

The use of Archard's wear equation to predict wear requires a known contact pressure distribution between the interacting bodies. For this purpose, the elastic Pasternak foundation model is adopted (shown in Figure 3.1(a)). The contact pressure at any point on the foundation surface relates not only to the displacement of the spring element at that point, but also to the shear interaction between adjacent elements. The contact pressure-displacement relation is:

$$P = k_s u - k_g \nabla^2 u, \tag{3.2}$$

where u denotes the displacement of the spring elements as well as the deflection of the foundation surface, which is measured from the initial undeformed surface (Figure 3.1(b)); k_s and k_g are the two foundation parameters, and ∇^2 is the second order differential operator, the Laplacian. The surface profile of the specimen, z, is measured from the initial unworn surface (Figure 3.1(b)). Prior to the onset of wear, it is assumed that the specimen and the counter-body are pristine and perfectly flat, i.e., $z = 0$ and $u = 0$. As the specimen surface keeps lowering due to wear, z is becoming more negative. Thus, the distance between the worn surface and the initial flat surface is $(-z)$. Assuming contact between the specimen and counter-body is perfect, the deflection of the foundation, u, and the surface profile of the specimen, z, can be related by a reference depth, h, in the contact region D (on the specimen) and Ω_c (on the counter-body) (Figure 3.1(b)). As illustrated in Figure 3.1(c), h is the sum of u and $(-z)$:

$$h = u + (-z). \tag{3.3}$$

Most of the currently available sliding abrasive wear models [38, 39, 70] including the rotary wear model presented in Chapter 2 require the explicit assumption of relevant boundary conditions at the contact region, D and Ω_c. This ignores the influence of the rest of the counter-body that is not in contact with the specimen, Ω_{nc}, and can cause profile discrepancies (Figure 3.1(b)). For example, in Chapter 2, the assumptions of Neumann boundary conditions are unable to fully capture boundary effects as shown in Figure 2.9. Depending on the relative size of the specimen and counter-body, these boundary effects may be significant.

Here, an implicit treatment of the boundaries is proposed by (i) replacing pre-assumed boundary conditions with continuity conditions for the vertical deflection at the boundaries

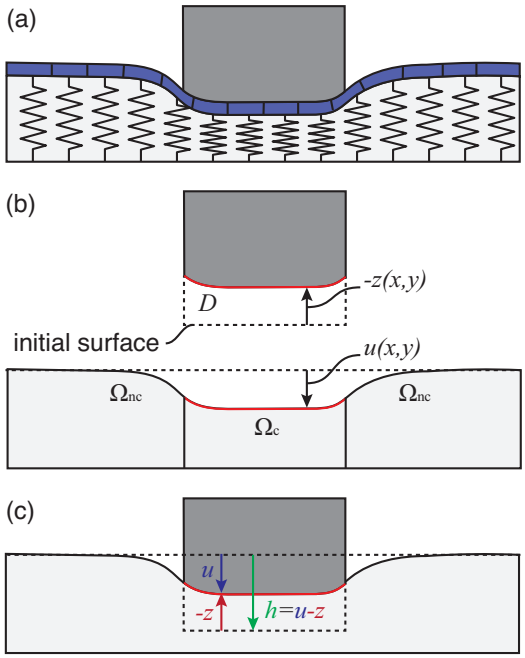

Figure 3.1: Schematics of Pasternak foundation model. (a) Indentation of worn specimen into counter-body (elastic foundation). (b) Separate views of deformed counter-body and worn specimen showing the contact region (Ω_c), the non-contact region (Ω_{nc}) on the deformed counter-body surface, and the worn specimen surface region (D). (c) Graphical illustration of counter-body deformation (u), specimen worn surface profile (z), and reference height (h).

between the contact and non-contact regions and (ii) prescribing, for numerical treatment, that the size of the foundation is much larger than the specimen. Thus the contact problem is considered on the whole foundation surface, $\Omega = \Omega_c \bigcup \Omega_{nc}$. The contact pressure is non-zero in Ω_c and zero in Ω_{nc}. A constant normal load, F_n, is applied on the specimen throughout the whole wear process, which is equal to the integral of the contact pressure over the entire region, Ω:

$$\int_\Omega P dS = \int_\Omega (k_s u - k_g \nabla^2 u) dS = F_n. \tag{3.4}$$

This constraint will later be used as the consistency condition for solving the evolving reference depth, h. It should be noted that only the applied normal force on the specimen

is constant, this means that the local contact pressure distribution will change during wear. Since the size of the counter-body is assumed to be much larger than the size of the specimen, the deflection of the foundation surface at the outer boundaries can be assumed to be zero:

$$u = 0, \quad \text{on } \partial\Omega. \tag{3.5}$$

The model outlined above is now further developed for two common wear systems: rotary and linear abrasive sliding wear systems.

3.1.1.1 Rotary wear systems

One of the wear systems of interest here is the rotary wear system with a rotary axial thrust washer configuration shown in Figure 3.2(a-b). The sliding velocity is distributed non-uniformly along the sliding interface; the velocity is the product of the rotating angular velocity, ω, and the local radial distance from the center of the annular domain, r. Archard's wear equation, Equation (3.1), for a rotary wear system is modified as:

$$\Delta z = -PKr\omega\Delta t, \tag{3.6}$$

which gives the wear depth at a particular location that is caused after a time increment Δt. For a single material or composite configuration that is rotationally symmetric, the wear rate, K, is only a function of the radial distance to the center, $K(r)$, which reduces the computational domain to be one-dimensional. The Pasternak foundation equation,

Equation (3.2), that is rotationally symmetric in a polar coordinate system is simplified as:

$$P = k_s u - k_g\left(\frac{\partial^2 u}{\partial r^2} + \frac{1}{r}\frac{\partial u}{\partial r}\right). \tag{3.7}$$

Besides the boundary condition imposed on the outer boundary by Equation (3.5), another boundary condition is imposed at the center of the foundation due to symmetry:

$$\frac{\partial u}{\partial r} = 0, \quad \text{at the center } (r = 0). \tag{3.8}$$

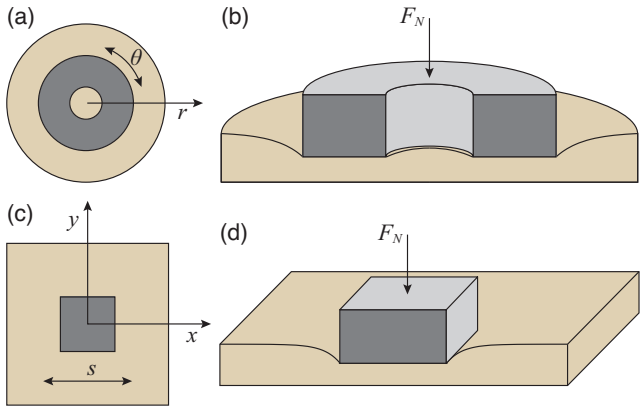

Figure 3.2: Illustration of rotary and linear wear systems. Rotary wear system: (a) top view; (b) side view. Linear wear system: (c) top view; (d) side view.

The model presented above could be easily adapted for non-rotationally symmetric composite configurations. This is achieved by defining a two-dimensional wear rate matrix in polar coordinates. Similarly, the Laplacian term in the Pasternak foundation equation, Equation (3.2), would include two-dimensional dependencies. Non-rotationally symmetric composite systems may be of interest for designing thrust washers that can accommodate heavy loads and are less sensitive to misalignment and oscillating movements [88, 89].

3.1.1.2 Linear wear systems

Another common system is the linear wear system (see Figure 3.2(c-d)), where the specimen is sliding against an abrasive counter-body along one direction in a reciprocating fashion. In this case, sliding velocity is uniformly distributed along the sliding interface; thus v is a constant in Archard's wear equation, Equation (3.1).

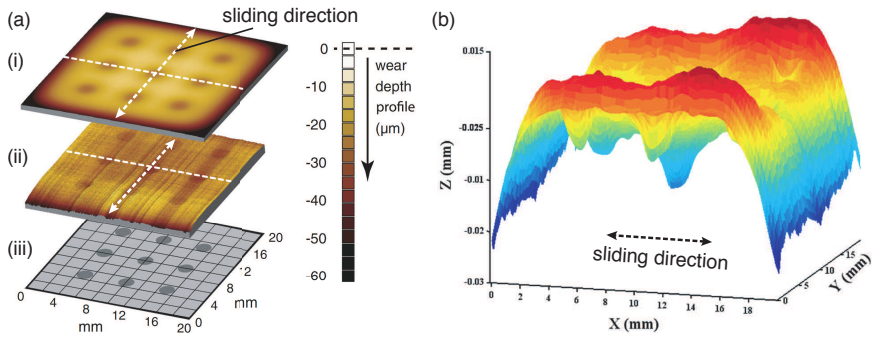

Figure 3.3: (a) Steady-state surface profile of a bi-material composite system from [75] subject to linear abrasive sliding wear. (a-i) Numerical surface profile prediction from a symmetric Pasternak foundation-based linear wear model. (a-ii) Experimentally measured surface profile. (a-iii) Epoxy (dark color) and PEEK (light color) composite configuration. (b) Smoothed experimental surface profile from (a-ii) [75] shown in 3D [90]. Note the asymmetry in surface profile with respect to sliding and counter-sliding directions.

In previous experimental studies of composites subject to linear sliding wear [75,90], the square composite specimen had 9 circular epoxy inclusions evenly distributed in the PEEK matrix (Figure 3.3(a-iii)). The specimen was sliding in a reciprocating fashion along one direction (denoted by the dashed arrows in Figure 3.3). As shown in Figure 3.3(a-ii) and Figure 3.3(b), the worn surface developed a steady-state profile which was not symmetric with respect to the sliding and counter-sliding directions. The surface profile is more uneven in the line-scans along the counter-sliding direction than in the sliding direction. However, this asymmetric profile evolution cannot be predicted by existing Pasternak foundation-based wear models because of their symmetric nature. Thus, here for the first time an

asymmetric foundation model is proposed to better simulate linear sliding wear:

$$P = k_s u - (k_{g,x}\frac{\partial^2 u}{\partial x^2} + k_{g,y}\frac{\partial^2 u}{\partial y^2}). \tag{3.9}$$

The proposed foundation model accounts for asymmetric effects during unidirectional sliding by treating the second order derivative terms separately in the Laplacian through alternative foundation parameters, $k_{g,x}$ and $k_{g,y}$. These account for the shear interactions in the $x-$ and $y-$directions (i.e. sliding and counter-sliding directions), respectively. When the foundation parameters are equal, $k_{g,x} = k_{g,y}$, the proposed foundation model recovers the original symmetric form, Equation (3.2).

3.1.2 Iterative simulation procedure

The wear process is modeled as an initial value boundary problem, which can be solved numerically in an iterative procedure. The computational domain includes the whole foundation surface, Ω, and the specimen surface, D, which corresponds to the contact region on the foundation surface, Ω_c, as shown in Figure 3.1(c). The computational domain is discretized into grids with uniform dimensions. The grids on the specimen surface, D, coincide with the grids at the contact region, Ω_c. Subscript i denotes spatial ordinates and the superscript, n, is a time iteration counter. Here, wear rate, K, is treated as a distinct system parameter specific to the operating conditions, which can be determined experimentally from preliminary wear tests as described in Section 2.4.1. For either a single material or multi-material composite configuration which are both deterministic, wear rates are assigned to each grid in D, denoted by K_i.

At n^{th} iterations, the specimen surface profile is z^n. The remaining problem is to calculate the contact pressure distribution corresponding to the updated specimen surface profile. The discrete form of the foundation model for the *rotary system* can be written as:

$$P_i^n = k_s u_i^n - k_g (\nabla^2 u)_i^n, \tag{3.10}$$

where the discrete Laplacian, $(\nabla^2 u)_i^n$, is approximated using the finite difference scheme corresponding to the spatial discretization. For the *linear system*, the asymmetric three-parameter foundation model can be discretized as:

$$P_i^n = k_s u_i^n - k_{g,x} (\frac{\partial^2 u}{\partial x^2})_i^n - k_{g,y} (\frac{\partial^2 u}{\partial y^2})_i^n, \tag{3.11}$$

where the second-order derivatives are approximated by finite-difference schemes as well. Thus, in general, the relation between $\mathbf{u}^n$ and $\mathbf{P}^n$ can be represented by a coupled linear system:

$$\mathbf{P}^n = \mathbf{C}\mathbf{u}^n, \quad \text{in } \Omega, \tag{3.12}$$

where $\mathbf{u}^n$ and $\mathbf{P}^n$ are vectors composed of all grids in Ω and C is a matrix composed of the coefficients from Equation (3.10) and Equation (3.11). Both $\mathbf{u}^n$ and $\mathbf{P}^n$ are partially known. The deflection of the foundation surface, $\mathbf{u}^n$, is related to the known specimen surface profile, $\mathbf{z}^n$, by the unknown reference depth parameter, h^n:

$$\mathbf{u}^n = \mathbf{z}^n + h^n \mathbf{e}, \quad \text{in } \Omega_c, \tag{3.13}$$

where $\mathbf{z}^n$ is the vector form of the specimen surface profile and $\mathbf{e}$ is an identity vector composed of values of unity. By definition, the specimen surface profile, $\mathbf{z}^n$, has physical

meaning only in D, which coincides with the contact region, Ω_c. Now, the definition of $\mathbf{z}^n$ is extended to the whole domain, Ω, which satisfies the relation with $\mathbf{u}^n$ everywhere:

$$\mathbf{u}^n = \mathbf{z}^n + h^n \mathbf{e}, \quad \text{in } \Omega. \tag{3.14}$$

Substituting $\mathbf{u}^n$ in the pressure-displacement relation, Equation (3.12), gives:

$$\mathbf{C}\mathbf{z}^n + h^n \mathbf{C}\mathbf{e} = \mathbf{P}^n, \quad \text{in } \Omega, \tag{3.15}$$

which relates contact pressure to the specimen surface profile and reference depth though a linear system. The consistency condition from the constant normal load constraint, Equation (3.4), can be written as

$$\int_\Omega [k_s(\mathbf{z}^n + h^n) - k_g(\nabla^2 \mathbf{z})^n] dS = \int_\Omega [k_s \mathbf{z}^n - k_g(\nabla^2 \mathbf{z})^n] dS + k_s|\Omega| h^n = F_n. \tag{3.16}$$

The integral can then be evaluated numerically and is represented by:

$$\mathbf{S}\mathbf{z}^n + k_s|\Omega| h^n = F_n, \tag{3.17}$$

where $\mathbf{S}$ is a row vector of the numerical integration coefficients. Combining Equation (3.15) and Equation (3.17), a linear system results:

$$\begin{bmatrix} \mathbf{C} & \sum_i \mathbf{C} \\ \mathbf{S} & k_s|\Omega| \end{bmatrix} \begin{bmatrix} \mathbf{z}^n \\ h^n \end{bmatrix} = \begin{bmatrix} \mathbf{P}^n \\ F_n \end{bmatrix}, \tag{3.18}$$

where $\sum_i \mathbf{C}$ is a vector with values of the summation of each row of the coefficient matrix $\mathbf{C}$.

All grids in Ω can be divided into two groups: in and outside of the contact area, Ω_c and Ω_{nc}. Using c and nc as subscripts to denote the grids in Ω_c and Ω_{nc}, respectively, Equation (3.18) is partitioned as

$$\begin{bmatrix} \mathbf{C}_{c,c} & \mathbf{C}_{c,nc} & \sum_{i_c} \mathbf{C}_{c,\cdot} \\ \mathbf{C}_{nc,c} & \mathbf{C}_{nc,nc} & \sum_{i_{nc}} \mathbf{C}_{nc,\cdot} \\ \mathbf{S}_c & \mathbf{S}_{nc} & k_s|\Omega| \end{bmatrix} \begin{bmatrix} \mathbf{z}_c^{n+1} \\ \mathbf{z}_{nc}^{n+1} \\ h^{n+1} \end{bmatrix} = \begin{bmatrix} \mathbf{P}_c^{n+1} \\ \mathbf{P}_{nc}^{n+1} \\ F_n \end{bmatrix}, \tag{3.19}$$

where the specimen surface profile, $\mathbf{z}_c^n$, is known from the previous calculation and the contact pressure outside the contact area, $\mathbf{P}_{nc}^n$, is zero. Thus the remaining unknowns, $\mathbf{z}_{nc}^{n+1}$ and h^n can be solved from:

$$\begin{bmatrix} \mathbf{C}_{nc,nc} & \sum_{i_{nc}} \mathbf{C}_{nc,\cdot} \\ \mathbf{S}_{nc} & k_s|\Omega| \end{bmatrix} \begin{bmatrix} \mathbf{z}_{nc}^n \\ h^n \end{bmatrix} = \begin{bmatrix} \mathbf{P}_{nc}^n \\ F_n \end{bmatrix} - \begin{bmatrix} \mathbf{C}_{c,c} \\ \mathbf{C}_{nc,c} \end{bmatrix} \mathbf{z}_c^n. \tag{3.20}$$

As a result, $\mathbf{P}_c^n$ can be calculated from

$$\mathbf{P}_c^n = \begin{bmatrix} \mathbf{C}_{c,c} & \mathbf{C}_{c,nc} & \sum_{i_c} \mathbf{C}_{c,\cdot} \end{bmatrix} \begin{bmatrix} \mathbf{z}_c^n \\ \mathbf{z}_{nc}^n \\ h^n \end{bmatrix}. \tag{3.21}$$

At this point, the contact pressure distribution, $\mathbf{P}_c^n$ is known. After a time increment, Δt, the incremental wear depth relative to the current surface profile and contact conditions at a particular location is:

$$\Delta z_i^n = -P_i^n K_i v_i \Delta t. \tag{3.22}$$

Then the new surface depth is updated according to:

$$z_i^{n+1} = z_i^n + \Delta z_i^n = z_i^n - P_i^n K_i v_i \Delta t. \tag{3.23}$$

The stop criterion can be set as maximum number of iterations or use the steady-state condition as introduced in Section 2.3.1, which is determined by the incremental depth change in Ω_c between two successive increments as:

$$\max \frac{|\Delta z_i^n - \Delta z_i^{n-1}|}{|\Delta z_i^{n-1}|} < \epsilon, \tag{3.24}$$

where ϵ is a very small constant (e.g. 1×10^{-8}). This simulation procedure is shown in Algorithm 1.

Input: system parameters: k_s, k_g, F_n, $\Omega = \Omega_c \bigcup \Omega_{nc}$, D, $\mathbf{C}$, and $\mathbf{S}$

Current state: $\mathbf{z}^n$

while $\max \frac{|\Delta z_i^n - \Delta z_i^{n-1}|}{|\Delta z_i^{n-1}|} < \epsilon$ ***or*** $n < n_{max}$ **do**

solve $\mathbf{z}_{nc}^n$ and h^n from Equation (3.22);

solve $\mathbf{P}_c^n$ from Equation (3.21);

$\Delta z_i^n = -P_i^n K_i v_i \Delta t$; $z_i^{n+1} = z_i^n + \Delta z_i^n$, for $i \in \Omega_c$;

end

Algorithm 1: Algorithm for wear simulation.

3.1.3 Solving for steady-state wear

As discussed in Section 2.3, wear process usually exhibits transitions from run-in stage to steady-state stage. Steady-state wear is characterized by two features: (i) the volume loss of the system increases linearly with increasing sliding time, which means that the wear rate of the system converges to a constant value; and (ii) the surface profile of the specimen surface reaches a shape that stays the same while recessing in depth as wear proceeds. Using the second characteristic of steady-state wear, the steady-state contact pressure distribution can be directly calculated from the wear rate distribution in the specimen (corresponding to the composite configuration). Thus the steady-state surface profile can also be directly solved for. At steady-state, the incremental height loss after a time increment at any position in the specimen surface should be the same.

In a *rotary wear system*, Archard's wear equation, Equation (3.6), gives:

$$P_{ss}Kr = \text{constant}, \tag{3.25}$$

where p_{ss} denotes the steady-state contact pressure distribution in the contact region. Using the condition of constant applied normal load, Equation (3.4), it is found that the steady-state contact pressure distribution is:

$$P_{ss} = F_n \frac{(\int_D (Kr)^{-1} dS)^{-1}}{Kr}. \tag{3.26}$$

The resulting steady-state composite wear rate for the rotary wear system, calculated as incremental volume loss divided by the product of normal load and the incremental rotating

angle, is:

$$K^{ss}_{R,comp} = \frac{|D|}{\int_D (Kr)^{-1} dS} =< (Kr)^{-1} >^{-1}, \tag{3.27}$$

where $< \cdot >$ denotes the average value over the domain D. This expression is consistent with Equation 2.21 derived in Section 2.3.2, which is determined by the wear rate of each material as well as the material distribution within the sliding interface.

In a *linear wear system*, the steady-state contact pressure distribution satisfies:

$$P_{ss} K = \text{constant}, \tag{3.28}$$

which leads to a steady-state contact pressure distribution:

$$P_{ss} = F_n \frac{(\int_D (K)^{-1} dS)^{-1}}{K}. \tag{3.29}$$

The resulting steady-state composite wear rate for the linear wear system, calculated as incremental volume loss divided by the product of normal load and the incremental sliding distance:

$$K^{ss}_{comp} = \frac{|D|}{\int_D (K)^{-1} dS} =< K^{-1} >^{-1} . \tag{3.30}$$

It is seen that the calculation of K^{ss}_{comp} follows the inverse rule of mixtures, which is determined by the wear rate and the area fraction of each material while does not depend on the material distribution within the sliding interface.

Having the steady-state contact pressure information, the steady-state deflection of the foundation surface, u_{ss}, can be directly determined from Equation (3.7) and Equation (3.9) for both rotary and linear wear systems, respectively. The shape of the specimen surface

profile when steady-state is reached, z_{ss}, is then also determined as it shares the same shape as u_{ss} in the contact region, Ω_c.

3.2 Method for experimental validation

In order to validate the proposed wear models and simulation, wear experiments for both rotary and linear wear systems have been performed. These wear experiments were conducted by Mr. Tomas Grejtak from the Tribology Laboratory at Lehigh University; I helped to direct the experimental setup, decide relevant parameters, and interpret experimental data.

The tests have been conducted on purpose-built rotary and linear reciprocating tribometers (Figure 3.4). In the *rotary tests*, the counter-body is a 6mm thick PDMS pad with a silicone carbide abrasive paper cover (grit 400, Norton Black Ice T214). The PDMS pad, Dow Corning Sylgard® 184, is made with a 10:1 ratio of elastomer to cross-linker and has an elastic modulus of 1.8 MPa. The applied normal load is 40N. The specimens were mounted to a collet chuck which is connected to a rotary reciprocating motor. One cycle is set to be 360° clockwise and 360° counter-clockwise with an angular velocity 0.64 rev/s, similar to a linear sliding velocity of 25 mm/s . The abrasive paper is changed after every 10 cycles to eliminate the influence of wear debris. More details for rotary tests can be found in Section 2.4.1. In the *linear tests*, the specimen is loaded against the counter-body at a load of 50N and sliding at a speed 50 mm/s in a reciprocating fashion. The counter-body consists of a 6mm thick PDMS pad with an elastic modulus of 2.3MPa and a silicon carbide abrasive paper cover (grit 1000, MagicW). One reciprocal cycle is set to be one stoke forward and one stroke backwards with a stroke length of 50mm. In the linear sliding test, the

abrasive paper is changed after every 5 cycles. More details for similar linear tests can be foundation in reference [75]. In addition, upon each paper removed, the specimen surface is also blown off with compressed air.

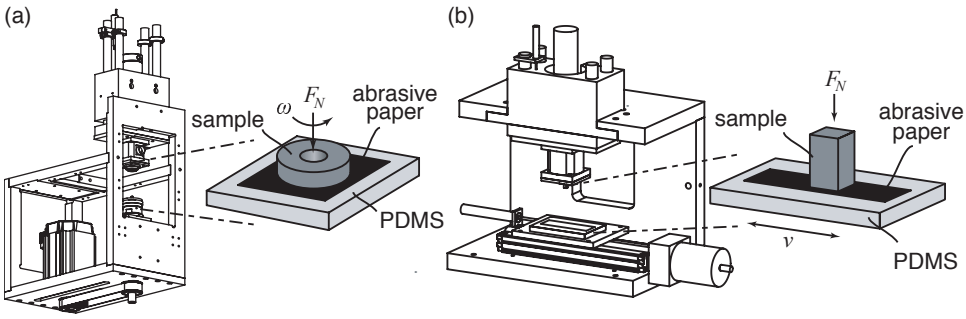

Figure 3.4: Schematic of tribometers used for wear tests. (a) Rotary tribometer. (b) Linear reciprocating tribometer.

The tested composite specimens are all composed of aluminum (6061) and epoxy (metallographic mounting epoxy, Dace Technologies) with different shapes and configurations. The aluminum base is machined with a CNC where vacant space is filled with epoxy resin. The specimen surface is machined flat before wear testing. The worn surface profile of the composite specimen is measured with a Bruker® Contour GT SWLI optical profilometer (scanning white light interferometry). A reference shoulder of the specimen is used to ensure that the specimen is aligned with the optical profilometer during scanning. The wear rate of each constituent material of the composite specimen is determined by wear testing of the single material specimen under the same testing conditions.

3.3 Calibration procedure for foundation model parameters

In order to implement the proposed model and method to simulate wear, the foundation parameters (which describe the reaction of the compliant counter-body) must be determined. Typically, these parameters are based on empirical formulas relating the foundation Young's

modulus and thickness [91]. In contrast, the proposed model and solution procedure outlined in Section 3.1 allows one to use the experimentally measured steady-state response of the wear system itself to calibrate these foundation parameters. This has never previously been done for foundation-based wear models.

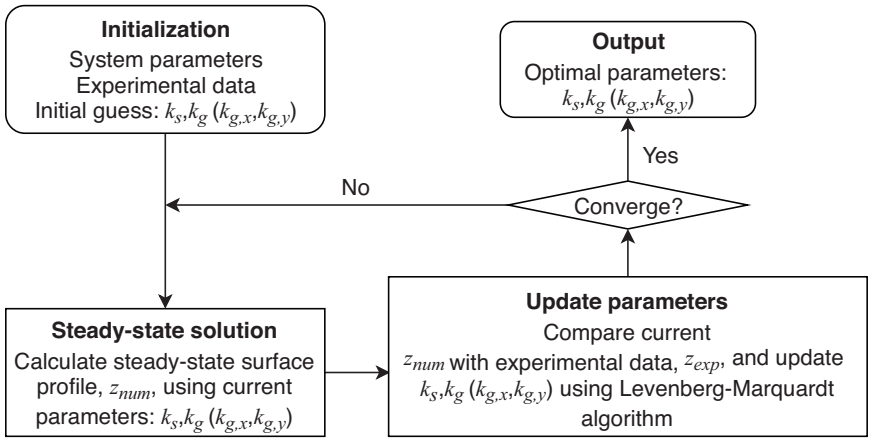

Figure 3.5: Calibration procedure for foundation parameters using the Levenberg-Marquardt algorithm [92].

The calibration is performed in an optimization sequence, where the experimental steady-state surface profile, $z_{ss,exp}$, is used as input profile and the numerical prediction, $z_{ss,num}$, is fitted to the input profile by finding the optimal parameters to minimize the error between the experimental and numerical profiles. The calibration is only based on the shape of the profiles not the actually depth of the worn surface. Thus, both the experimental input profile and the numerically predicted profiles are translated to the same depth level with average of zero, i.e.

$$\tilde{z}_{ss,exp} = z_{ss,exp} - < z_{ss,exp} >, \tag{3.31}$$

$$\tilde{z}_{ss,num} = z_{ss,num} - < z_{ss,num} >, \tag{3.32}$$

where $\tilde{z}_{ss,\cdot}$ denotes the translated profile and $< \cdot >$ represents the average value.

The flow chart in Figure 3.5 shows the iterative calibration procedure. The experimental profile $z_{ss,exp}$, related material and system parameters, and initial guesses for the foundation parameters are the input needed for the calibration. Based on the current parameters, the steady-state surface profile $z_{ss,num}$ is solved according to the method described in Section 3.1.3 and then translated to $\tilde{z}_{ss,num}$. Then the current numerical profile $\tilde{z}_{ss,num}$ is compared with the experimental profile $\tilde{z}_{ss,exp}$ and the error between the two profiles drives the optimization algorithm to update the foundation parameters. Here, a Levenberg-Marquardt algorithm is utilized, which uses the reduced chi-squared error, χ^2, between the experimental and numerical profiles as the objective [92]. The optimization algorithm iteratively reduces the error through a sequence of updates to parameter values until the optimal foundation parameters are found.

3.4 Results and discussion

In this section, numerical results for wear prediction using the proposed models and simulation procedure from Section 3.1 for both rotary and linear wear systems are presented. The foundation parameters for rotary and linear wear systems are calibrated using experimental data following the calibration procedure in Section 3.3. In particular, we focus on experimentally validating worn surface profile evolutions, mass and volume loss for bi-material composite systems, but the models presented above are more general.

3.4.1 Demonstration for rotary wear systems

Three composite specimens are tested on the rotary tribometer following the test procedure described in Section 3.2. The specimens, Cases 1, 2, and 3, shown in Figure 3.6(a), all consist of 50% aluminum and 50% epoxy, with different in-plane configurations. These annular specimens have an inner radius $R_1 = 4.24$mm and an outer radius $R_2 = 12.7$mm. The wear rates of aluminum and epoxy are determined by wear tests under the same operating conditions as for the composite specimen; these are 2.4×10^{-2}mm^3/Nm and 2.66×10^{-1}mm^3/Nm, respectively. The solid curves in Figure 3.6(b-c) show the experimental steady-state surface profiles of these specimens, which are represented by line-scans along the radial direction of the worn surface. The use of this experimental data for the proposed model calibration and validation is explained in Section 3.3 and in the following.

3.4.1.1 Experimental calibration of foundation parameters

In particular, to demonstrate the efficacy of the calibration procedure in Section 3.3, the steady-state surface profile of the composite system, Case 1, shown in Figure 3.6(a) is used to calibrate the foundation parameters of the counter-body used in the wear tests described in Section 3.2 (consisting of a 6mm PDMS pad with an elastic modulus of 1.8MPa and an abrasive paper with grit 400). The foundation parameters, k_s and k_g, are optimized following the calibration procedure in Figure 3.5. The calibration starts with an initial guess for $k_s = 0.3$N/mm^3 and $k_g = 2.8$N/mm, which is based on the empirical formulas typically used [91]. The whole circular foundation domain, Ω, is assumed to be concentric with the sliding region, D, with a radius of $R = 5(R_2 - R_1) = 42.3$mm. The calculated steady-state surface profile is shown in Figure 3.6(b), and compared with the corresponding

experimental results.

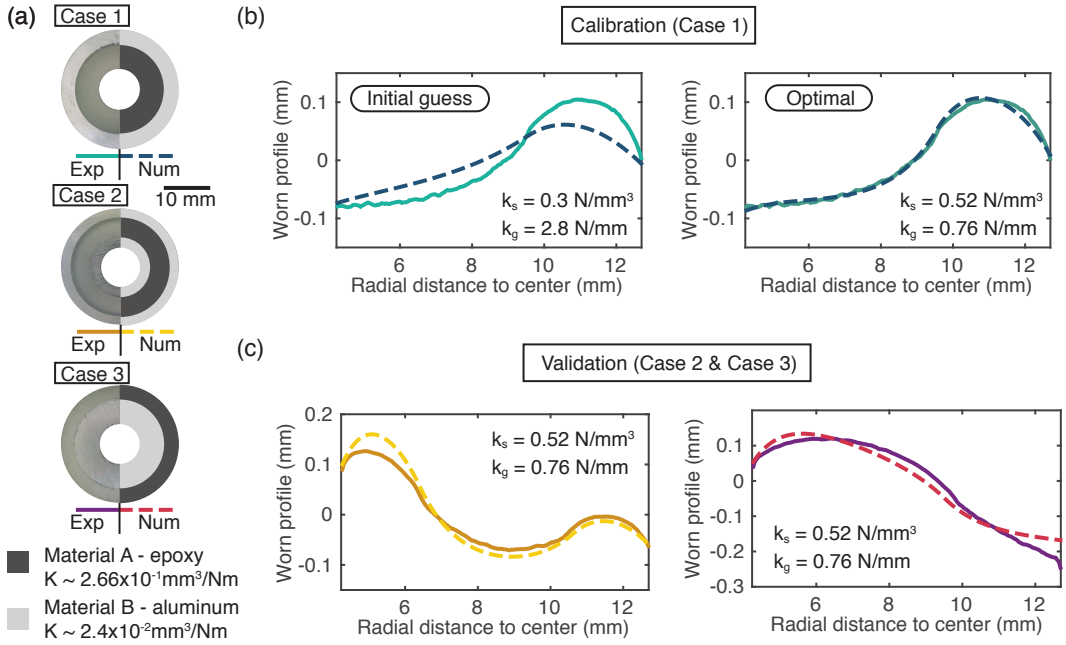

Figure 3.6: Calibration of foundation parameters using experimental data and validation of numerical simulations. (a) Three composite specimens (Cases 1-3); the left image is half of the experimental specimen and the right image is half of the numerical simulation domain. (b) Calibration of foundation parameters using Case 1. (c) Validation of calibrated foundation parameters using Case 2 and 3. Note that experimental data are shown with solid lines and numerical results with dashed lines.

To quantify the quality of the match between the numerical and experimental profiles, the mean percentage error is calculated as:

$$\epsilon_{\text{profile}} = \frac{\text{mean}(|\tilde{z}_{ss,exp} - \tilde{z}_{ss,num}|)}{\max(\tilde{z}_{ss,exp}) - \min(\tilde{z}_{ss,exp})} \times 100\%. \tag{3.33}$$

The mean percentage error between the initial guess and experimental profile is 16%. The calibration procedure converges at the optimal values of $k_s = 0.52\text{N/mm}^3$ and $k_g = 0.76\text{N/mm}$, which represents both 73% differences compared to the empirical formulas. It is observed that the steady-state surface profile predicted by the optimal foundation parameters fits well with the experimental profile as shown in Figure 3.6(b). The mean percentage

error of Case 1, using the calibrated parameters, reduces to 3%.

Next, the foundation parameters that were calibrated based on Case 1 results are then fixed and used to simulate Cases 2 and 3. In particular, the steady-state surface profiles of Cases 2 and 3 are calculated. The comparisons with experimental results are shown in Figure 3.6(c). Good agreement between the experimental and numerical results for both cases can be observed. The mean percentage errors are calculated as 8% and 6% for Cases 2 and 3, respectively. *These results demonstrate that the calibration procedure could be performed once for a given counter-body and operating conditions and then be used to predict the wear of general composite specimens. In particular, it could be used with arbitrary material layouts (as long as the specimen materials can be approximated as isotropic and as being rigid compared to the counter-body; similarly, the compliant counter-body must be isotropic and remain elastic).*

3.4.1.2 Prediction of material removal

In addition to surface profile, other key features of wear, such as mass and volume loss, can be numerically predicted by the proposed wear model and simulation procedure. Numerically, mass and volume loss are calculated at every time step based on the full-field height loss of the specimen surface and known material densities. The numerical predictions are shown with solid lines in Figure 3.7(a-b). For comparison, the experimental results are shown as open circles for the 3 Cases. The experimentally measured material removal during the wear process is presented by the total mass loss measured directly after a certain number of rotating cycles. The corresponding experimental volume loss is calculated at selected cycles based on the mass loss and surface profiles. The numerical results predict

the same trends as the experimental results. That is, after the initial run-in stage, Case 1 loses the most mass and volume while Case 3 loses the least. Good agreement is found especially for Case 3. Percentage errors are calculated for both mass and volume loss at 4000 cycles in Figure 3.7(c), which are all below 15%.

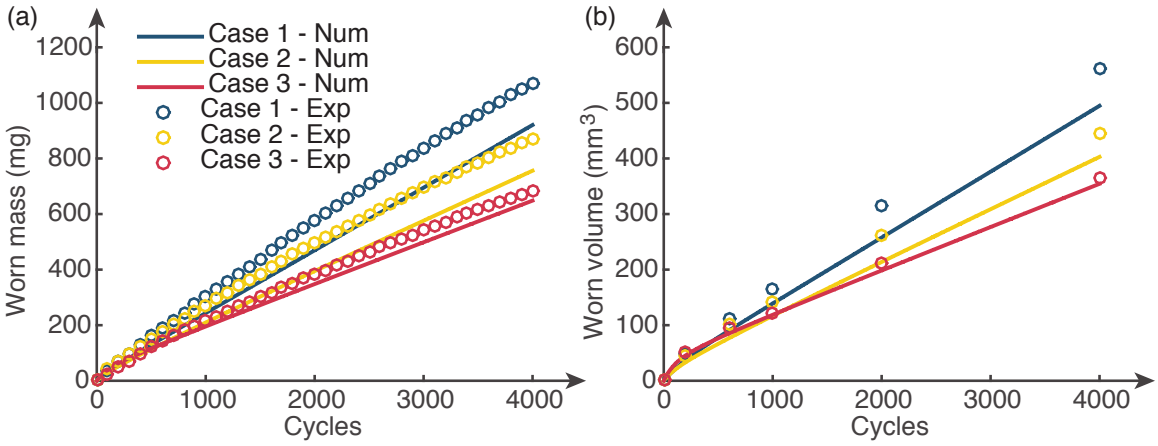

(c) Percentage Error at 4000 cycles

	Case 1	Case 2	Case 3
% error (mass)	14%	13%	5%
% error (volume)	12%	10%	3%

Figure 3.7: Material removal histories of Case 1-3. (a) Mass loss. (b) Volume loss. (c) Errors of numerical predictions comparing experimental data.

3.4.1.3 Comparison of models based on surface profile evolution predictions

In order to demonstrate the improved prediction capability of the proposed calibrated model compared to previous model described in Chapter 2, a comparative study is presented in this section. Here, the composite configuration, Case 2 from Figure 3.3 is studied. The following parameters are assumed. The annular specimen has an inner radius $R_1 = 4.24$mm and an outer radius $R_2 = 12.7$mm. The wear rates of epoxy and aluminum are set as $K_a = 0.266\text{mm}^3/\text{Nm}$ and $K_b = 0.024\text{mm}^3/\text{Nm}$, respectively. The foundation parameters (based on the calibration presented above in Section 3.4.1) are $k_s = 0.52\text{N}/\text{mm}^3$ and $k_g =$

0.76N/mm. For comparison, the same values for geometry, wear rates, and foundation parameters are used in the model previously presented in Chapter 2.

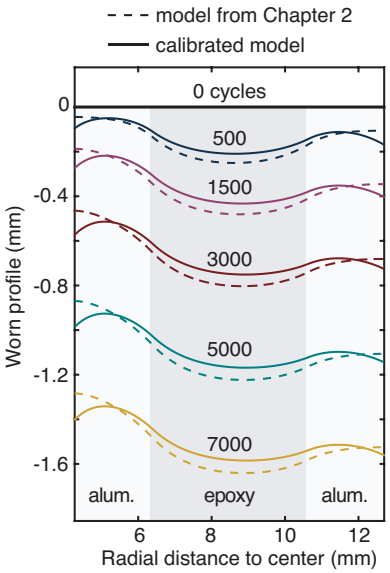

Figure 3.8: Case study: specimen surface profile evolutions at selected cycles using the experimentally calibrated proposed and the previously established (Chapter 2) simulation procedures.

Figure 3.8 shows the evolutions of worn surface profiles from both the proposed model and simulation procedure (solid curves) and the model from Chapter 2 (dashed curves) at selected rotating cycles. In both cases, the surface evolves from an initially flat to an uneven profile and eventually reaches steady-state with the shape of the surface profile unchanged. However, due to the assumption of zero-slope Neumann boundary conditions in Chapter 2, the profiles satisfy the boundary condition during the whole simulation process. As a result, there are significant edge differences compare to the experimental observations as seen in Figure 3.6(b). The proposed simulation procedure does not impose the zero-slope Neumann boundary conditions thus the surface profile is evolving with changing slopes at the boundaries, which better reflects the response of the whole foundation system (Figure 3.6).

3.4.2 Demonstration for linear wear systems with asymmetry

This section presents two examples which demonstrate the effectiveness of the parameter calibration and wear simulation procedures for linear wear systems. In the first example, a bi-material composite with a relative simple in-plane material distribution is presented. The second example presents an application of the linear wear simulation in predicting the wear evolution of three topology optimized bi-material composites for minimal run-in material volume loss.

3.4.2.1 Example: bi-material composite with simple configuration

The experimental results for a bi-material composite specimen subject to linear wear is shown in Figure 3.9. A square specimen consisting of aluminum and epoxy has been tested by sliding along a horizontal direction against an abrasive counter-body. Due to the different counter-body properties, the wear rate of aluminum and epoxy have slightly higher values than in the rotary wear tests above (2.9×10^{-2}mm^3/Nm and 3.0×10^{-1}mm^3/Nm, respectively).

Figure 3.9(a) shows the in-plane configuration and denotes the sliding direction. The steady-state in-plane height distribution of the specimen surface is shown in Figure 3.9(b). Line scans are made along the two directions through the center (Figure 3.9(d)). Both profiles share the same general shape that contains two peaks in the aluminum region and a valley in the epoxy region. The profile along the sliding direction is flatter than that of the counter-sliding direction. It is seen that the composite configuration is symmetric with respect to the sliding and counter-sliding directions, while the steady-state surface profile

is not.

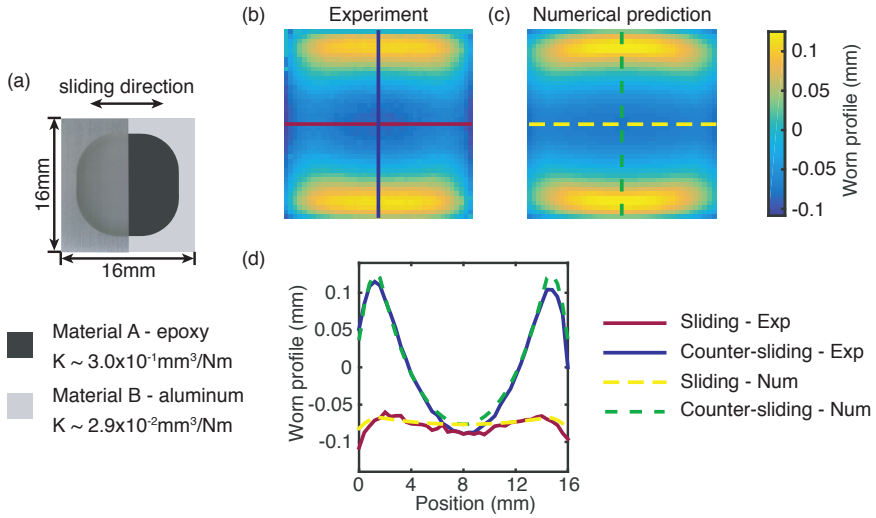

Figure 3.9: Case study for a linear wear system. (a) Composite specimen under linear wear; the left image is half of the experimental specimen and the right image is half of the numerical simulation domain. (b) Experimental steady-state surface profile. (c) Numerical steady-state surface profile. (d) Comparison of line-scans of experimental (solid lines) and numerical (dashed lines) steady-state surface profiles. Results for both sliding and counter-sliding directions are shown.

The foundation parameter calibration procedure from Section 3.3 is applied to calibrate the proposed three-parameter asymmetric foundation model. In this case, the experimental data for the steady-state surface profile shown in Figure 3.9(b) is taken as the target. The values of the three foundation parameters, (k_s, $k_{g,x}$, and $k_{g,y}$) in Equation (3.9), are updated according to the optimization algorithm (Figure 3.5) until convergence is reached. The initial guess for the foundation parameters is chosen based on the empirical formulas typically used [91] as $k_s = 0.38\text{N/mm}^3$ and $k_{g,x} = k_{g,y} = 3.42\text{N/mm}$. Calibrated foundation parameters are $k_s = 0.23\text{N/mm}^3$, $k_{g,x} = 25.06\text{N/mm}$, and $k_{g,y} = 1.64\text{N/mm}$, representing 40%, 633%, and 52% differences compared to the empirical formulas, respectively. Note also that the difference between the calibrated $k_{g,x}$ and $k_{g,y}$ is large, which is assumed to relate to the sliding conditions, e.g. sliding velocity. That is, it is presumed that a higher sliding velocity would exacerbate differences in the calibrated $k_{g,x}$ and $k_{g,y}$, whereas a lower

sliding velocity would reduce this difference. Future work is needed to investigate this relationship between the asymmetry of the foundation model and the sliding conditions. Figure 3.9(c) shows the predicted steady-state in-plane height distribution using the experimentally calibrated values of the foundation parameters and Figure 3.9(d) compares the line-scans of sliding and counter-sliding directions. Good agreement between the numerical prediction and experimental data is found, which gives a mean percentage error calculated using Equation (3.33) of 4%.

3.4.2.2 Example: optimized composites for minimizing run-in volume loss

In this section, the foundation parameter calibration and wear simulation procedures are demonstrated for three bi-material composites. Figure 1.13 displays the in-plane material distributions of the unit-cells for three periodic composites. These designs were produced by a level-set based topology optimization routine that minimized material volume loss during run-in wear. The optimizations were performed with a very basic and indirect consideration of manufacturability (where geometric complexity was influenced by a perimeter penalization parameter, τ) [41,70]. The optimization routine was developed based on the symmetric Pasternak foundation model with empirical foundation parameters and the assumption of periodic boundary conditions. As a result the optimal unit cell designs identified have symmetric material distributions (Figure 3.10). The composite configurations can be seen as periodic arrays by repeating the unit cells.

These optimized composites have been fabricated and tested to validate the optimization routine. However, due to limitations in fabrication and wear testing processes, each of the composite specimens consisted of only 9 unit-cells (3×3) as shown in Figure 3.10. The

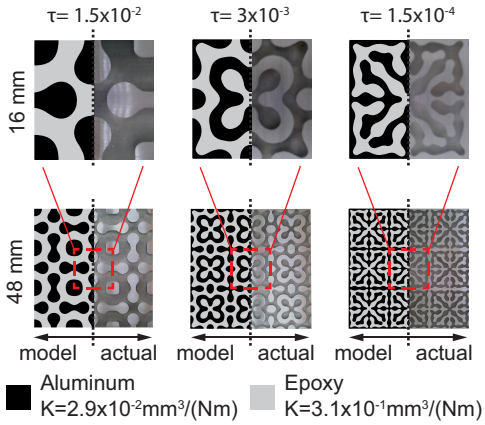

Figure 3.10: Optimized periodic composites (shown in unit-cell and 3×3 layout) for minimal run-in volume loss with different feature complexity increasing as τ decreases [41].

dimensions of the fabricated specimens are 48mm$\times$48mm and the applied normal load is 350N (0.152MPa average contact pressure). Figure 3.11(a) shows the experimental measured surface profiles of the whole composite surfaces. It is seen that the worn surfaces all develop asymmetric worn profiles with respect to sliding direction and rounded features near the edges. Figure 3.11(b) shows the surface profiles of the central unit-cell, which is the only cell of interest for purposes of experimental assessment of the topology optimization routine. Note that the assumed periodic boundary conditions are not fully satisfied for the central unit-cell. Asymmetry of the worn surface profiles caused by unidirectional sliding is apparent.

The calibration procedure is performed using the experimentally measured steady-state surface profiles. The profiles of the central unit-cells of the three cases are taken as input for the calibration procedure so that the foundation parameters are optimized for all three cases at the same time. This is done because the complex features of the composites and the resulting worn surface profiles can increase the chance of converging to local optima in the optimization-based calibration procedure. Taking three experimental profiles as inputs for the calibration can increase the probability of approaching a global optimum.

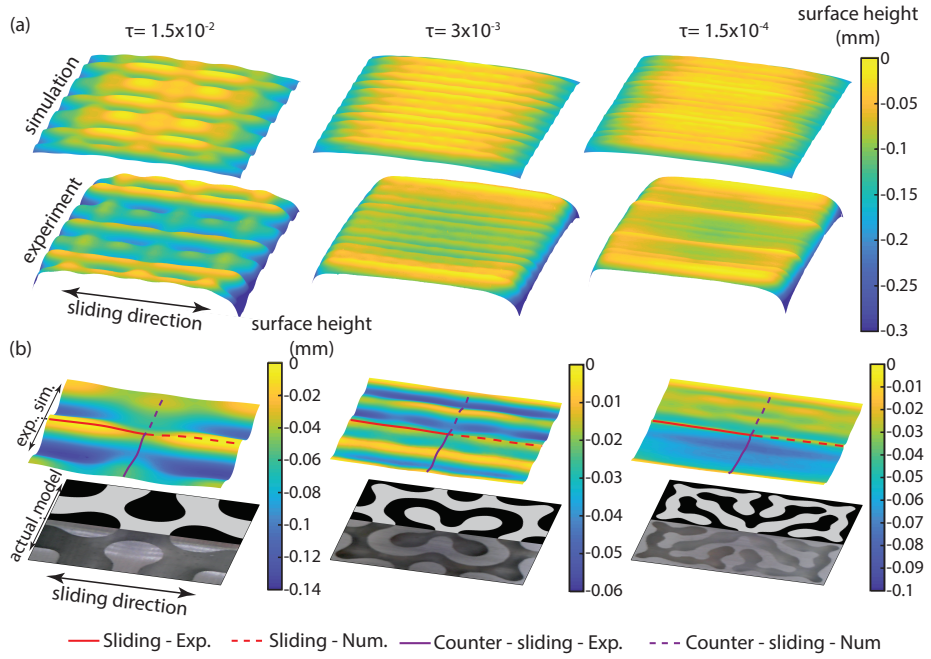

Figure 3.11: Experimental and numerical worn surface topographies after 1000 sliding cycles. (a) Whole surface (3x3 layout). (b) Unit-cell.

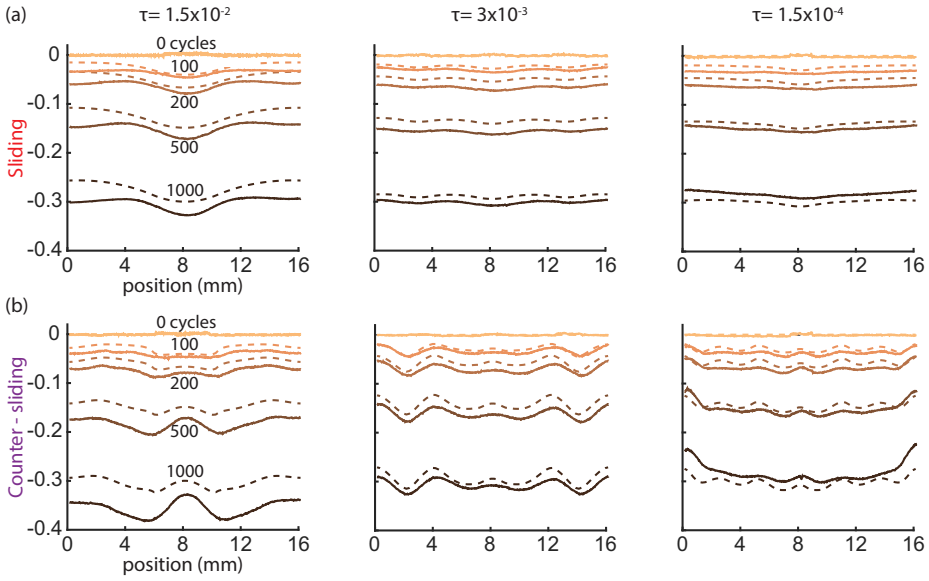

Figure 3.12: Surface profile evolution of the unit-cell at selected sliding cycles. (a) Line-scan along the sliding direction. (b) Line-scan along the counter-sliding direction.

The calibrated foundation parameters are $k_s = 0.48\text{N/mm}^3$, $k_{g,x} = 26.10\text{N/mm}$, and $k_{g,y} = 1.34\text{N/mm}$. The predicted surface profiles using calibrated foundation parameters are shown in Figure 3.11 comparing to the experimental profiles. The iterative wear simulations

of the three cases are performed using calibrated parameters which can provide the evolution of the worn surface profiles in shape and depth. In Figure 3.12(b-c), the experimental and numerical profiles are plotted along two line-scans (sliding and counter-sliding directions) and at selected sliding cycles (numerical iterations). Good agreement is seen between the experimental and numerical results. Not only the shape of the numerical profiles matches well with the experimental profiles, but also the depth of the worn profiles can be predicted accurately by the numerical simulation during the whole wear process including run-in and steady-state stages.

3.5 Summary

A generalized foundation-based wear model and simulation framework has been proposed for both rotary and linear wear systems that allows for more accurate and realistic predictions of wear evolution. Improvements have been made through incorporating implicit boundary conditions for the contact analysis, proposing an asymmetric elastic foundation model for linear wear, and formulating an optimization-based calibration procedure for the elastic foundation models. The capability of the proposed framework has been demonstrated for both rotary and linear wear systems. It is shown that the foundation parameters can be effectively calibrated based on experimentally measured steady-state surface profiles. The wear simulation is able to capture the evolution of worn surface profile and material loss with improved accuracy. It is found that, by incorporating the asymmetric foundation model and calibrating the foundation parameters, the wear simulation is able to predict the evolution of worn surface profile and material loss during run-in and steady-state regimes with improved accuracy.

Chapter 4

Frictional heating and thermomechanical wear model

So far, abrasive sliding wear has only been considered and simulated from a mechanical perspective. However, wear is always complicated by multiphysical phenomena occurring at sliding interfaces. This chapter focuses on one of the most critical of these: frictional heating. The thermal analysis for frictional heating is formulated based on a three-dimensional steady-state heat transfer model with frictional heat flux boundary conditions. The finite volume method is used to solve for the elevated thermal field within the sliding body and verified by finite element analysis performed in the commercial software Abaqus. The frictional heating analysis is then integrated into the wear models established in Chapter 3 to model thermomechanical wear by incorporating temperature-dependent wear rates. An iterative procedure consisting of sequential contact and frictional heat analyses and wear calculations is established for thermomechanical wear simulation. An example of a bi-material composite subject to linear wear is presented and a comparative study is conducted to address the

differences between thermomechanical and mechanical-only wear simulations.

4.1 Model for frictional heating

Depending on the temperature-sensitivity of materials, frictional heating can significantly impact tribological performance and reduce component lifetimes. Therefore, to accurately predict wear, especially in systems with high sliding velocities, large applied loads, and friction, it is necessary to take the thermal effects into consideration. There have been extensive analytical studies of frictional heating problems based on the pioneering work of Blok [94] and Jaeger [95], where heat source methods were used to determine the flash temperature component of contact temperatures. Flash temperature refers to the short-duration temperature rise at asperities within the contact region. These analytical solutions obtained using heat source methods are based on the assumption that the sliding body is a homogeneous, semi-infinite half-space. However, in reality, sliding bodies are not infinitely large and they often are made of more than one material. In addition, the available analytic solutions are only for uniform, parabolic and semi-ellipsoidal heat flux distributions with simple contact shapes (bands and circles). Numerical methods such as finite element analysis (FEA) have also been utilized to solve frictional heating problems. Some of the advantages of using FEA include being able to model sliding bodies with finite dimensions and irregular geometries, thus broadening the range of practical applicability [96]. A large amount of FEA work has focused on the disc brake system [97–99] and total hip implants [100, 101] where frictional heating can play a key role in the performance. For example, frictional heating at the head-cup interface in the implants causes temperature rise in the bearing components and surrounding tissues, which increases the risk of damage to surrounding tissues and can

lead to long-term aseptic loosening failure.

In this section, a simplified model for frictional heating at sliding interfaces is developed that incorporates aspects from both analytical and FEA based approaches. This model offers convenience for integration into the previously established mechanical wear models (Chapter 2 and Chapter 3). A balance in computational costs and model accuracy and flexibility is needed for the purpose of efficient thermomechanical wear simulation in an optimization framework.

4.1.1 Frictional heating calculations

Frictional heating is related to the contact pressure, coefficient of friction, and relative velocity between sliding bodies. As shown in Figure 4.1, frictional heating is considered at the sliding interface of a two-body linear sliding system. Body 1 is sliding against a motionless counter-body (Body 2) with a constant velocity, v. The frictional heat flux generated at a specific position within the sliding interface, $\dot{q}_0(x, y)$, can be computed by:

$$\dot{q}_0(x, y) = v\mu(x, y)P(x, y), \tag{4.1}$$

where v is the relative sliding velocity, $\mu(x, y)$ is the local coefficient of friction, and $P(x, y)$ is the local contact pressure. The total frictional heat generation is partitioned between the two sliding bodies. A heat partitioning factor, α, is used to represent the portion of frictional heat that goes into Body 1, $\dot{q}(x, y)$:

$$\dot{q}(x, y) = \alpha(x, y)\dot{q}_0(x, y) = \alpha(x, y)v\mu(x, y)P(x, y). \tag{4.2}$$

The heat partition between contacting bodies is a relatively complicated process which depends on the relative sliding and contact conditions, as well as the material properties of the sliding bodies [102]. Here, in order to simplify the problem, it is conservatively assumed that the counter-body (Body 2) is non-conductive so that heat flux can only enter the sliding Body 1, which corresponds to the case of $\alpha = 1$.

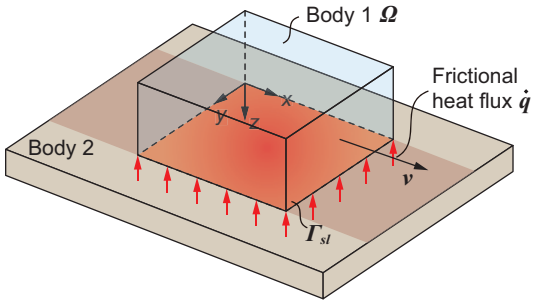

Figure 4.1: Schematic of frictional heating in a two-body sliding system.

Similar to the wear calculation using Archard's wear equation, the local frictional heat flux depends on the local contact pressure as well as the local tribological properties. Thus, when surface profiles and contact pressure distributions evolve simultaneously during wear processes, frictional heating flux distributions at the sliding interface will also change.

4.1.2 Heat transfer analysis

4.1.2.1 Heat transfer model

Figure 4.1 shows the two-body linear sliding system where Body 1 is of interest to investigate wear and frictional heating. The heat transfer problem is formulated to obtain the temperature field within Body 1 caused by frictional heating at the sliding interface. The bottom face of Body 1 is the sliding interface where wear occurs and frictional heat is generated. It is assumed that the contact between the two sliding bodies is perfect with no

separation.

The heat transfer within Body 1 is modeled by a three-dimensional steady-state heat transfer equation with or without an internal volumetric heat source. The governing equation in the cubic domain, Ω, as shown in Figure 4.1, is

$$\nabla \cdot (\boldsymbol{k} \nabla \boldsymbol{T}) = \boldsymbol{q}_{vol} \text{ in } \Omega, \tag{4.3}$$

where $\boldsymbol{k}$ is the thermal conductivity, $\boldsymbol{T}$ is the temperature field, and $\boldsymbol{q}_{vol}$ is the internal volumetric heat source. Different boundary conditions can be imposed according to the actual environmental and operating conditions of the tribological system. The boundary conditions of interest in this dissertation include prescribed temperature, surface heat flux, as well as boundary convection and insulation conditions, which can be mathematically formulated as:

- Prescribed temperature boundary condition is applied to surface in contact with a heat sink with fixed temperature T_0:

$$\boldsymbol{T} = T_0 \text{ on } \Gamma_{\text{sink}}; \tag{4.4}$$

- Surface heat flux boundary condition is applied to surface with heat input (e.g. frictional heat flux):

$$-\boldsymbol{k} \nabla \boldsymbol{T} \cdot \boldsymbol{n} = \dot{\boldsymbol{q}}_{surf} \text{ on } \Gamma_{\text{flux}}; \tag{4.5}$$

- Convective boundary condition is applied to surface undergoing convective exchange

with the surrounding media at T_{ref} with a heat transfer coefficient h:

$$-\boldsymbol{k}\nabla\boldsymbol{T}\cdot\boldsymbol{n} = h(\boldsymbol{T} - T_{\text{ref}}) \text{ on } \Gamma_{\text{conv}}; \tag{4.6}$$

- Insulated boundary condition is applied to adiabatic surfaces or surfaces with thermal symmetry:

$$-\boldsymbol{k}\nabla\boldsymbol{T}\cdot\boldsymbol{n} = 0 \text{ on } \Gamma_{\text{ins}}. \tag{4.7}$$

4.1.2.2 Finite volume method

The finite volume method (FVM) [103] is applied to solve the above governing equation (Equation (4.3)) with appropriate boundary conditions to obtain the thermal field within Ω. The cubic domain Ω is discretized uniformly into cubic control volumes and each of them has a uniform thermal conductivity (material A or B) which is determined by the node located at the center. Each control volume with dimensions is identified by its central node with spatial locations in x, y, and $z-$directions. The governing equation for each control volume is derived based on a balance of heat flux. Figure 4.2 shows an interior volume, represented by its central node C and its six neighbors, denoted as N, S, W, E, T, and B at the directions of 'north', 'south', west', 'east', 'top', and 'bottom', respectively. The FVM form of the heat transfer equation based on a heat balance for node C is

$$q_{\text{nc}}dxdz + q_{\text{sc}}dxdz + q_{\text{wc}}dydz + q_{\text{ec}}dydz + q_{\text{tc}}dxdy + q_{\text{bc}}dxdy = 0. \tag{4.8}$$

The heat flux q_{nc} between node C and its northern neighbor N is calculated as

$$q_{\mathrm{nc}} = (T_{\mathrm{n}} - T_{\mathrm{c}})/R_{\mathrm{nc}}, \tag{4.9}$$

where R_{nc} is the thermal resistance between nodes N and C (Figure 4.2), determined by

$$R_{\mathrm{nc}} = \frac{dy/2}{k_{\mathrm{n}} dx dz} + \frac{dy/2}{k_{\mathrm{c}} dx dz}. \tag{4.10}$$

Similarly, the heat flux between node C and its other neighbors can be calculated by the thermal conductivity and temperature of each node and relative geometric dimensions. Boundary nodes are handled separately based on the prescribed boundary conditions using finite difference approximations.

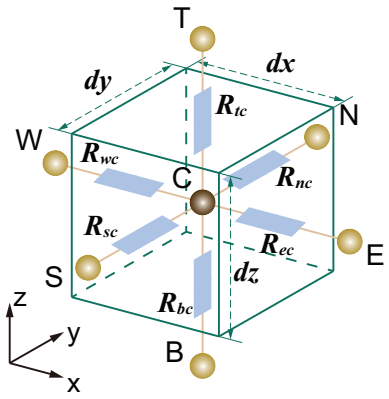

Figure 4.2: Schematics of a representative volume cell for the FVM.

Finally, the established nodal governing equations can be assembled into a linear equation system, represented in matrix form as:

$$\mathbf{AT} = \mathbf{b}, \tag{4.11}$$

where matrix $\mathbf{A}$ contains the parameters of conductivity, convection, and geometry and

vector **b** contains boundary condition information including frictional heat fluxes. The temperature field can be obtained from Equation (4.11) using appropriate solvers.

4.1.2.3 Numerical verification

In this section, a test case is presented in order to verify the established heat transfer model and finite volume method. The numerical solutions are compared with those obtained from the commercial finite element software, Abaqus 6.14-1, (SIMULIA, Providence, RI).

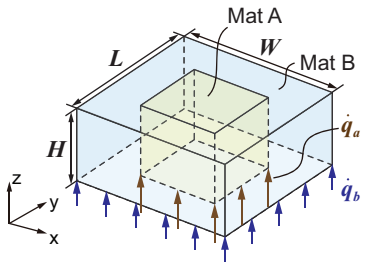

Figure 4.3: Schematic of the test case model.

Figure 4.3 shows the bi-material composite domain and boundary conditions for the test case. The cubic domain has dimensions $L = W = 0.18$m and $H = 0.09$m and consists of material A and B with thermal conductivities of $k_a = 100$W/(mK) and $k_b = 1$W/(mK). The material distribution is as shown in Figure 4.3, where the matrix (material B) has a cuboidal inclusion of material A. There is no volumetric heat generation within the domain. Boundary conditions include fixed temperature at the top face, convective boundary conditions at all side faces, and surface heat flux at the bottom face. The surface heat flux has a piecewise constant distribution, which has the value of $\dot{q}_a = 2000$ W/m^2 in the area occupied by material A and has the value of $\dot{q}_b = 4000$W/m^2 in the area occupied by material B. Utilizing the symmetry of the geometry and boundary conditions, only a quarter of the domain is needed for computations. The quarter domain is discretized into

$30 \times 30 \times 30$ elements in the x-, y-, and z-directions.

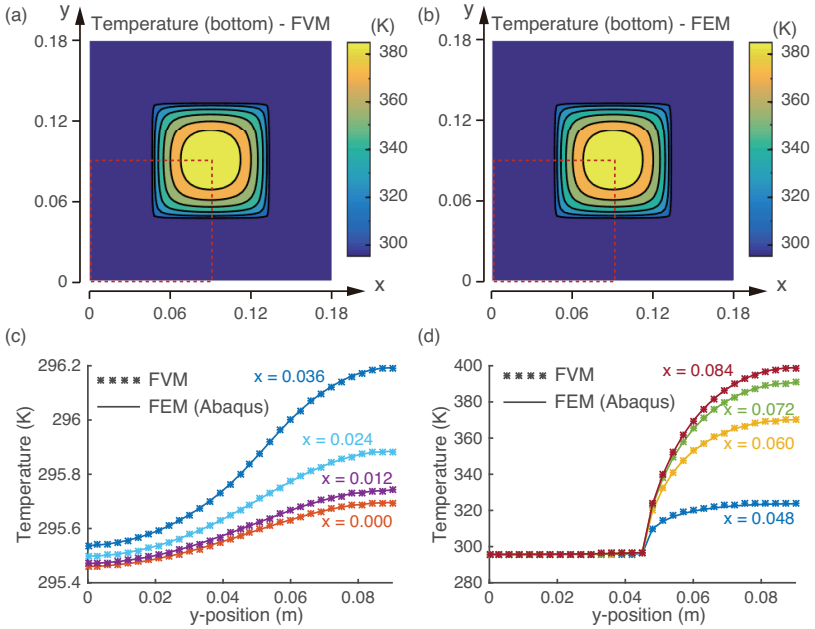

Figure 4.4: Numerical verification of the FVM. Temperature distribution at the bottom face obtained using the (a) FVM and (b) FEM (Abaqus). (c-d) Temperature distribution along line-scans at the bottom face (plotted only in the quarter domain).

Figure 4.4(a) and (b) display temperature distributions at the bottom face (shown in the full domain) obtained from the in-house finite volume code (FVM) and Abaqus (FEM), respectively. Figure 4.4(c) and (d) plots the temperatures along several line-scans across the bottom face from both methods. Good agreement between the FVM and Abaqus results is observed which verifies the effectiveness and accuracy of the established heat transfer model and the finite volume code.

4.2 Thermomechanical wear simulation

In the wear models presented in Chapter 2 and Chapter 3, it is assumed that each material has a distinct wear rate which remains constant during the simulation process. However, the wear rate associated with a material is in reality not typically a constant; it is a system

parameter that depends on temperature, pressure, environment and many other factors. This simplifying assumption could be relaxed to address modeling needs for more complex scenarios, such as the influence of multiphysics at sliding interfaces on wear. The proposed heat transfer model for frictional heating in Section 4.1 enables the incorporation of temperature-dependent wear rates into the established wear simulation framework. This is a first step towards thermomechanical wear investigations, so for now, the effects of thermal stress on contact pressure and surface profile changes due to thermal expansion are neglected. In addition, all other thermal and tribological parameters are treated as temperature-independent.

To formulate the simulation conditions, one additional assumption made here is that the sliding process can be treated as a quasi-steady process where the heat transfer within the sliding body can reach steady-state at each time increment when the relative sliding velocity is slow. However, this assumption might not be suitable for high-speed sliding or rotating cases. Regarding the computational domain, Ω, although wear leads to uneven worn surface, it is assumed that the surface height losses and profile changes are relatively small compared to the overall dimensions of the sliding body and thus Ω remains the same throughout the entire wear simulation.

The iterative thermomechanical simulation procedure consists of sequential contact analysis, frictional heating analysis, and wear calculation. The contact pressure distribution is computed using the elastic foundation model as a function of worn surface profile. At each increment, contact temperatures can be obtained by performing steady-state heat transfer analysis with frictional heat generation at the sliding interface that is proportional to the local contact pressure, coefficient of friction and relative sliding velocity. The local

wear rate is then updated according to the predefined wear rate-temperature relation using the local contact temperature information.

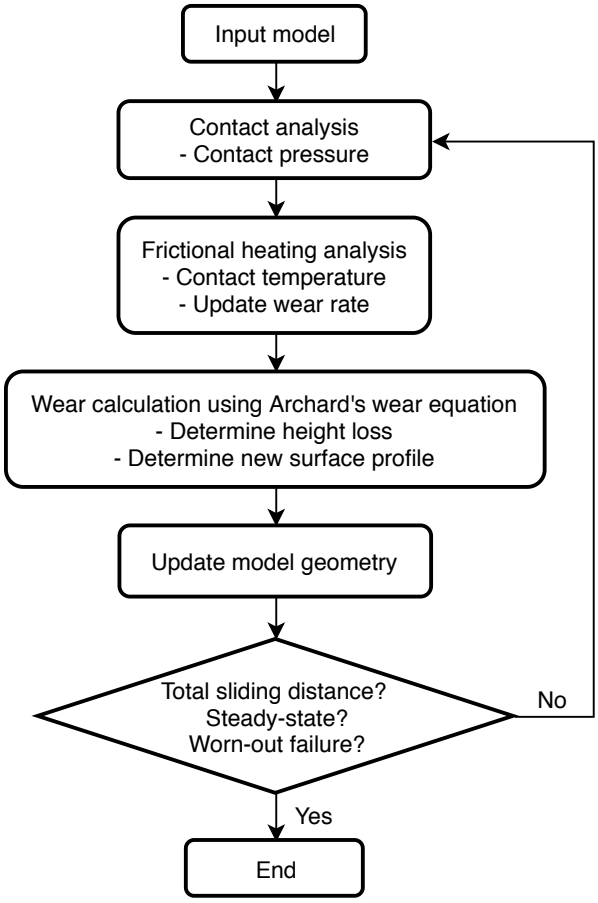

Figure 4.5: Flow chart of thermomechanical wear simulation.

The local incremental wear depth caused by an incremental sliding distance is calculated using the Archard's wear equation. In linear wear systems, the incremental wear depth at a particular position at the n^{th} iteration is

$$\Delta z_i^n = -P_i^n K_i^n(T_i^n) v \Delta t, \tag{4.12}$$

where the local wear rate, $K_i^n(T_i^n)$, is determined by the local material and temperature. The temperature dependence of wear rates associated with materials is an input required for

the proposed wear model and this must be experimentally determined. The contact pressure distribution, $\mathbf{P}_c^n$, follows the same method described in Section 3.1.2 for mechanical wear, based on an asymmetric elastic foundation model with large foundation assumption. The contact temperatures are obtained from the steady-state heat transfer analysis with appropriate boundary conditions including frictional heat flux. Then the wear rate distribution within the sliding interface can be updated according to the material distribution and current contact temperature distribution. The above steps are conducted in an iterative procedure until a stop criterion is met. Similar to the mechanical wear simulation, a steady-state condition parameter, ϵ (Equation (3.24)), which quantifies surface shape changes between two successive iterations, is used to detect whether steady-state wear is reached or not. The iterative procedure is depicted in the flow chart of Figure 4.5.

4.3 Case study for thermomechanical wear simulation

This section presents a case study for a bi-material composite subject to linear wear using the established thermomechanical wear simulation routine. The evolution of key wear features (volume loss and worn surface profile) are monitored during the wear process. In addition, the evolution of contact temperature and the resulting evolving wear rate distribution at the sliding interface are investigated. Comparisons are made between the thermomechanical wear case and two mechanical wear cases.

4.3.1 Problem setup

The bi-material composite of interest in the case study is shown in Figure 4.6(a); it consists of two materials with different thermal and tribological properties. It is meant to be generally representative of a typical polymer (Material A) and metal (Material B) composite. The material distribution throughout the volume of the composite is an extrusion from the sliding interface (Figure 4.6(b)) such that the x-y planar distribution remains the same along the z-direction. The thermal conductivity and coefficient of friction for each material are assumed to be temperature-independent and the values are given in Table 4.1. The temperature-dependency of the wear rate associated with each material is set only according to reported trends in the literature. The relation specifying temperature-dependence of wear rates is discussed further in the next section.

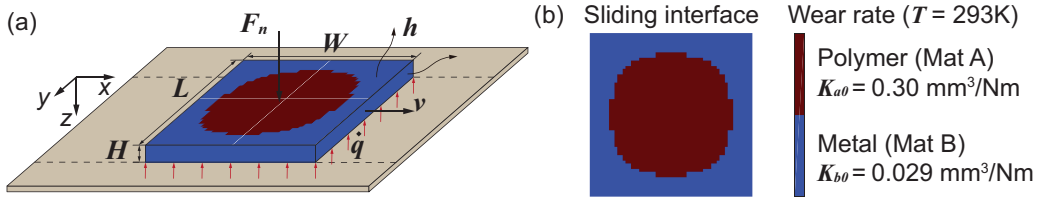

Figure 4.6: Schematic of a bi-material composite subject to thermomechanical wear. (a) Setup of the linear wear system. (b) Material distribution at the sliding interface.

The dimensions of the composite domain are $L = W = 0.2$m and $H = 0.02$m. The constant normal load applied on the composite is $F_n = 200$N resulting in a constant average pressure within the sliding interface of $P_0 = 0.005$MPa. The constant relative sliding velocity is $v = 2$m/s. The bottom face is the sliding interface where wear occurs and frictional heat is generated. The top and side faces are subject to convective conditions with the ambient environment. The ambient temperature is kept at $T_{ref} = 293$K and the heat transfer coefficient is $h = 10\text{W}/(\text{m}^2\text{K})$. The initial temperature of the composite is

$T_0 = 293K$ and the sliding interface is initially flat. The foundation parameters of the elastic foundation model are set as $k_s = 0.3\text{N/mm}^3$, $k_{g,x} = 10\text{N/mm}$, and $k_{g,y} = 3\text{N/mm}$, which allows for asymmetric effects in linear wear systems. The domain is discretized into a uniform mesh with 60, 60, and 6 elements in the x-, y-, and z-directions, respectively. By symmetry, only a quarter of the whole domain is needed for computations. The time increment is set as $\Delta t = 0.05\text{s}$, corresponding to an incremental sliding distance of $\Delta s = v\Delta t = 0.1\text{m}$.

Property	Polymer (Material A)	Metal (Material B)
Thermal conductivity, k [W/(mK)]	1	100
Coefficient of friction, μ	0.1	0.4

Table 4.1: Representative thermal conductivities and coefficients of friction for polymer (Material A) and metal (Material B).

4.3.2 Temperature-dependent wear rates

Thermal effects on wear are considered by incorporating temperature-dependent wear rates. Figure 4.7(a) plots the wear rates of unfilled PEEK and its carbon fiber reinforced composites as a function of contact temperature [104]. It is seen that slight changes in wear rate are detected for the unfilled PEEK while the wear rate of the PEEK composites with different fiber volume fractions increase with increasing temperature, in particular, by about 1.5 orders of magnitude within the range 20-220°C. The wear rates of the Al-Si alloy and Al-Si/graphite composite decreased with increasing temperature as shown in Figure 4.7; this is due to the rapid formation of oxide film on sliding components at higher temperatures [105].

Based on these reported trends of wear rate-temperature relations [104, 105], it is as-

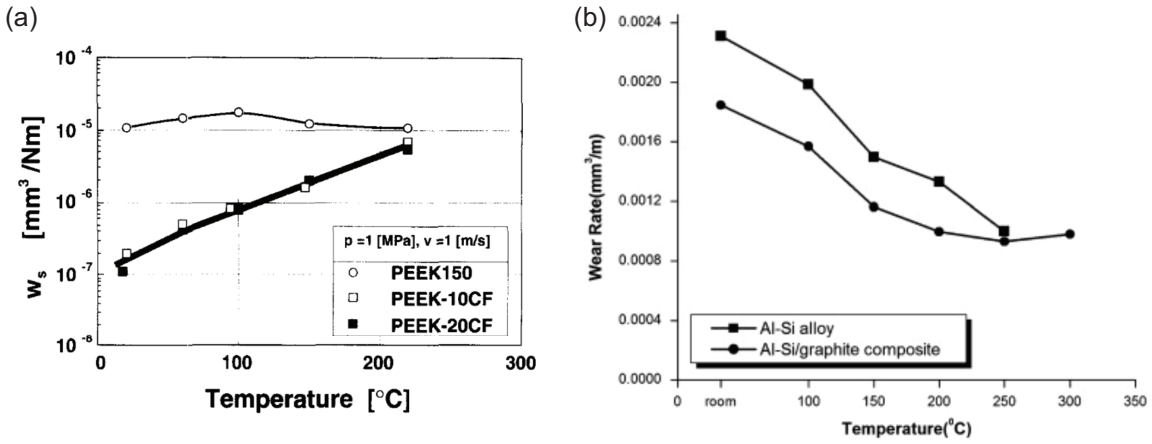

Figure 4.7: Wear rate as a function of temperature for: (a) PEEK composites with different volume fractions of short carbon fibers [104] and (b) Al-Si alloy and its composite [105].

sumed here that the wear rate of polymer (Material A) increases linearly with increasing temperature while the wear rate of metal (Material B) decreases linearly with increasing temperature. Figure 4.8 shows the wear rate of the generalized materials as a function of temperature. The room-temperature ($T_0 = 293$K) wear rates of polymer (Material A) and metal (Material B) are $K_{a0} = 0.3\text{mm}^3/\text{Nm}$ and $K_{b0} = 0.029\text{mm}^3/\text{Nm}$, respectively.

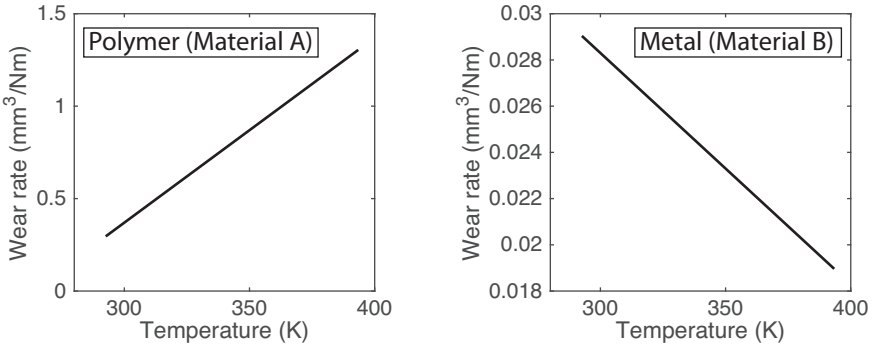

Figure 4.8: Wear rate-temperature relations for polymer (Material A) and metal (Material B).

4.3.3 Numeral results for thermomechanical wear evolution

Figure 4.9 plots the total volume loss and instantaneous composite wear rate against the total sliding distance. The instantaneous composite wear rate measures the overall wear

rate of the composite surface. It is found by taking the total incremental volume loss divided by the product of the applied normal load and incremental sliding distance, which reflects the slope of the total volume loss vs sliding distance curve. The total volume loss increases rapidly in the beginning and the volume loss curve becomes linear. Correspondingly, the composite wear rate is initially high and gradually decreases to a constant lower value. The evolution of the total volume loss and composite wear rate exhibit the typical experimentally-based observation of a transition from run-in to steady-state wear. After 6306 iterations, equivalent to a sliding distance of 630.6m, the steady-state condition of $\epsilon = 1 \times 10^{-6}$ is met; this is denoted by 'star' markers in the two plots of Figure 4.9.

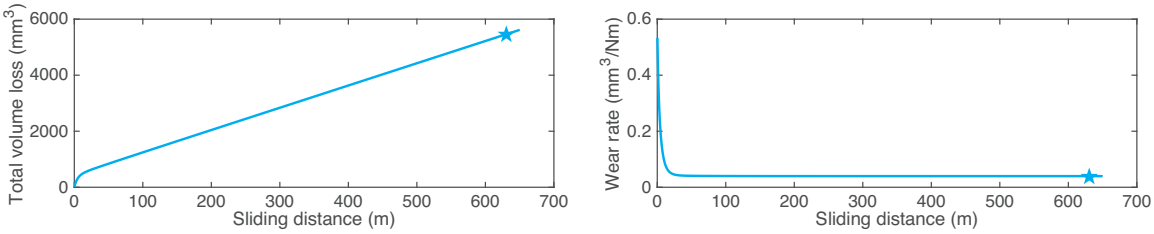

Figure 4.9: Total volume loss and instantaneous composite wear rate vs sliding distance.

Figure 4.10 shows the evolution of the worn surface profile, contact pressure, temperature and wear rate distribution at the sliding interface for select iterations. As wear proceeds, the composite surface develops a non-planar shape. The central part of the sliding interface occupied by the less wear-resistant polymer (Material A) generally wears more than the outer area occupied by the more wear-resistant metal (Material B). The surface height different between the two material area increases until the surface reaches a constant shape at steady-state. The contact pressure and frictional heat flux distributions evolve with changing surface profile profile; as a result the thermal field within the sliding body also changes. It is seen that, in contrast to the piecewise constant steady-state contact pressure distribution obtained from the mechanical wear simulation, the contact pressure

distribution in each material domain is non-uniform (Figure 4.10(b)). The temperature distribution at the sliding interface is shown in Figure 4.10(c). At the onset of run-in wear, the temperature in polymer (Material A) is higher than it is in metal (Material B). However, the distribution reverses quickly and eventually converges to a steady-state where the temperature decreases from the boundaries to the center of the sliding interface and metal (Material B) has higher temperatures than polymer (Material A). The average steady-state temperature in polymer (Material A) and metal (Material B) are $< T_{a,ss} >= 361$K and $< T_{b,ss} >= 369$K, respectively. This corresponds to a 23% increase in temperature for the polymer (Material A) compared to the initial $T_0 = 293$K and a 26% decrease in temperature for the metal (Material B).

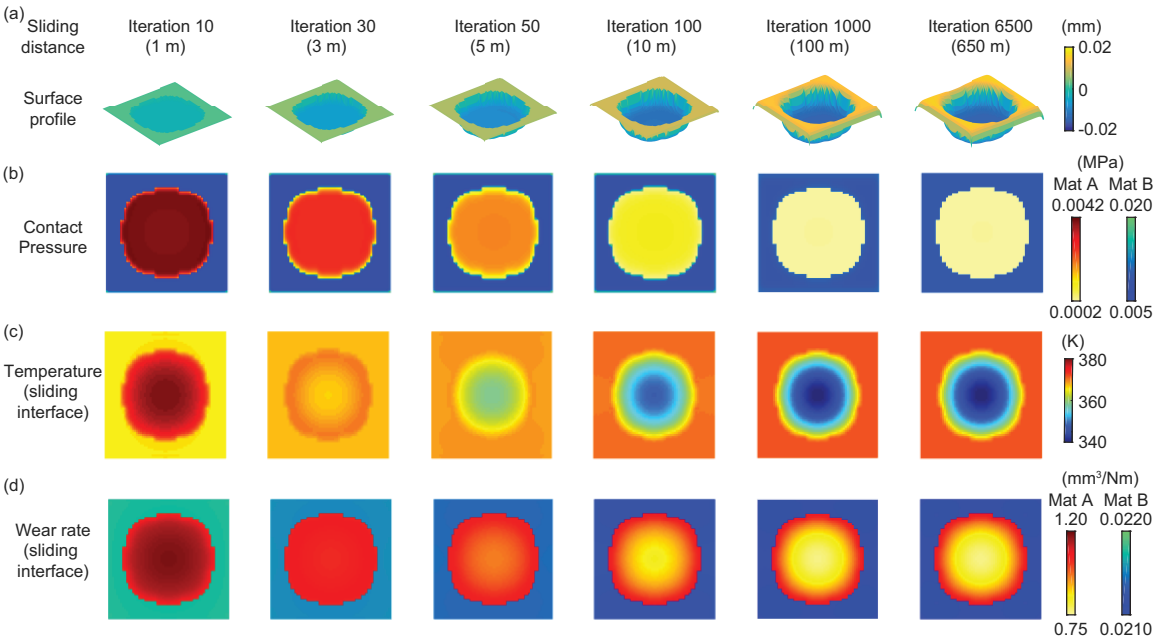

Figure 4.10: Thermomechanical wear evolution at selected iterations. (a) Worn surface profile. (b) Contact pressure distribution. (c) Contact temperature distribution. (d) Wear rate distribution.

Similar to the temperature distribution, the distribution of wear rates within the sliding interface undergoes a major transition as the wear process evolves from run-in to steady-state regimes (Figure 4.10(d)). Comparing the steady-state wear rate distribution with

the initial distribution at room temperature (Figure 4.6), it is expected that the steady-state wear rate values are all higher than the initial values because of the rise in contact temperature that is experienced. At steady-state, the wear rate distribution converges to a non-piecewise constant distribution, where the wear rate distribution in each material is non-uniform due to the non-uniform temperature distribution (Figure 4.10(d)). The average steady-state wear rates in Material A and Material B are $< K_{a,ss} >= 0.92\text{mm}^3/\text{Nm}$ and $< K_{b,ss} >= 0.021\text{mm}^3/\text{Nm}$, respectively. This corresponds to a 207% increase in wear rate for the polymer (Material A) compared to the initial $K_{a,0} = 0.3\text{mm}^3/\text{Nm}$ and a 27% decrease for the metal (Material B) compared to the initial $K_{b0} = 0.029\text{mm}^3/\text{Nm}$. In this way, in the thermomechanical wear simulation, wear affects contact pressure and temperature, which in turn determine wear rate and wear.

4.3.4 Comparison of thermomechanical and mechanical wear

In this section, a comparative study is conducted to evaluate the significance of thermal effects on wear. Two additional cases are examined using the mechanical wear simulation routine from Chapter 3 without incorporating the temperature-dependent wear rates. In Mechanical Case 1, the wear rate of each material is constant and remains at it room temperature value, i.e. the initial wear rate used in the thermomechanical wear simulation, $K_{a0} = 0.30.3\text{mm}^3/\text{Nm}$ and $K_{b0} = 0.029\text{mm}^3/\text{Nm}$ (Figure 4.11(a)). In Mechanical Case 2, the wear rate distribution within the sliding interface is also temperature-independent with the same distribution as the final steady-state non-uniform wear rate distribution obtained from the iterative simulation of the Thermomechanical Case at iteration 6500 (Figure 4.11(b)). The rest of the simulation set-up and parameters are kept the same as

the thermomechanical wear case as described in Section 4.3.1.

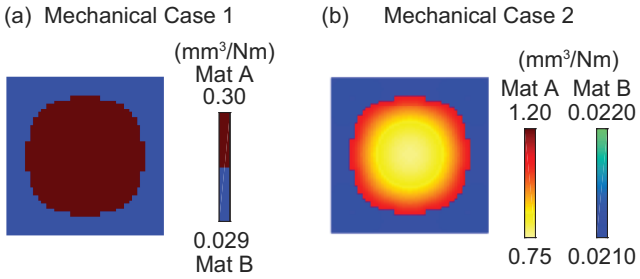

Figure 4.11: Wear rate distribution of Mechanical Case 1 and 2.

Figure 4.12 compares the total volume loss and instantaneous composite wear rate evolution of the three cases. The same steady-state condition, $\epsilon = 1 \times 10^{-6}$, is utilized for all simulations and the 'star' markers are again used to denote the first iteration where the condition is met (steady-state is achieved). It is seen that all three cases exhibit the typical transition from run-in to steady-state. Steady-state is first reached in the Mechanical Case 1 after 4943 iterations (494.3m). The Thermomechanical Case and Mechanical Case 2 reach steady-state around the same time, after 6306 iterations (630.6m) and 6303 iterations (630.3m), respectively.

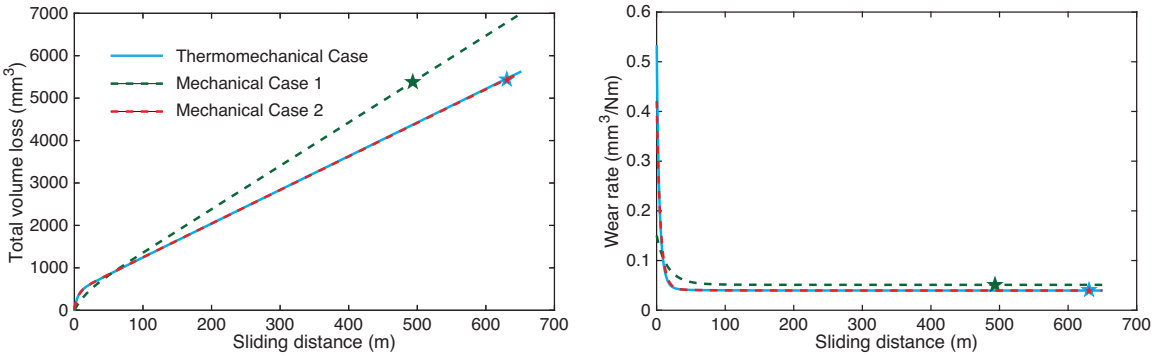

Figure 4.12: Total volume loss and instantaneous composite wear rate as a function of sliding distance.

By comparing the Thermomechanical Case and Mechanical Case 1, it is seen that the former experiences more severe wear at the very beginning of the run-in wear regime. This is manifested by the much higher composite wear rate and steeper total volume loss curve

for the Thermomechanical Case. The underlying cause is the significant increase in temperature at the sliding interface, especially in polymer (Material A, for which the wear rate increases with temperature). However, the composite wear rate of the Thermomechanical Case decreases rapidly and eventually converges to a lower steady-state value than the Mechanical Case 1, although the average wear rate increase in Material A (207%) is more significant than the average wear rate decrease in Material B (27%) and the area fraction ratio of the two materials is around 1:1. It is clear that the "Thermomechanical Case and Mechanical Case 2 converge to the same steady-state composite wear rate (Figure 4.12). Note also that the run-in evolution of these two cases is almost the same despite a slightly higher composite wear rate for the Thermomechanical Case at the onset of sliding.

The trend in the steady-state composite wear rate of these three cases is further confirmed by the direct calculation using Equation (3.30) derived in Section 3.1.3, which is equivalent to the inverse rule of mixtures. Table 4.2 displays the steady-state composite wear rate values of each case obtained from both the iterative simulation ("Iterative method") and the direct calculation using Equation (3.30) ("Direct method"). For the Thermomechanical Case, the steady-state composite wear rate is calculated based on the non-uniform steady-state wear rate distribution (Figure 4.10(d)). The same wear rate distribution is used to calculate the steady-state composite rate for the Mechanical Case 2. For the Mechanical Case 1, the steady-state composite wear rate is calculated based on the piecewise constant wear rate distribution which is the same as the initial wear rate distribution of the Thermomechanical Case (Figure 4.6(b)).

Figure 4.13(a) shows the in-plane steady-state worn surface profiles for the Thermomechanical Case/Mechanical Case 2 and the Mechanical Case 1 and Figure 4.13(b) plots

	Steady-state composite wear rate [mm^3/(Nm)]		
	Thermomechanical	Mechanical Case 1	Mechanical Case 2
Iterative method	0.0397	0.0511	0.0397
Direct method	0.0397	0.0511	0.0397

Table 4.2: Comparison of steady-state composite wear rates.

profiles along two perpendicular line-scans across the center of the sliding interface for these cases. These profiles are translated to the same level with an average surface height of zero to compare the shapes. The steady-state worn surfaces of the Thermomechanical Case and the Mechanical Case 2 have the same shape because of the same steady-state wear rate distributions. Due to the asymmetric elastic foundation model utilized for simulations, the surfaces develop asymmetric shapes with respect to the sliding direction for both cases. The height difference between the two material domains is higher in the Thermomechanical Case/Mechanical Case 2; this is due to the increased difference in wear rates of the constituent materials.

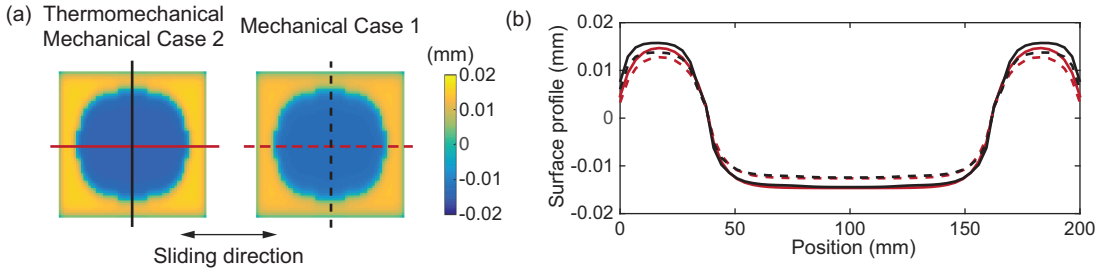

Figure 4.13: Comparison of steady-state surface profile between Thermomechanical Case/Mechanical Case 2 and Mechanical Case 1. (a) In-plane steady-state surface profiles. (b) Surface profiles along line-scans.

The thermomechanical wear simulation (incorporating temperature-dependent wear rates) gives vastly different predictions of wear evolution (volume loss, composite wear rate, and worn surface profile) from the mechanical wear simulation that employs static

room-temperature wear rates (independent of temperature). This indicates that ignoring the temperature-dependence of wear rates could lead to over-or-under estimates of these important wear features. However, a detailed set of thermomechanical wear experiments is required to further investigate this.

The Mechanical Case 2 (mechanical wear simulation performed using a temperature-independent wear rate distribution that is identical to the steady-state wear rate distribution developed in the Thermomechanical Case) results in an almost identical prediction of both run-in and steady-state compared to the Thermomechanical Case. Thus, if the steady-state contact pressure, temperature, and wear rate distribution of a thermomechanical wear process could be explicitly determined from the materials and operating conditions of a particular wear system, performing the mechanical wear simulation using these steady-state parameters could give a good and efficient estimate of the thermomechanical wear evolution of material volume loss and worn surface profile. The thermomechanical model also provides opportunity to explore the effects of thermal expansion and thermal stresses on wear performance.

4.4 Summary

In this chapter, a first analysis of frictional heating associated with wear has been presented by incorporating temperature-dependent wear rates in a thermomechanical wear model. An iterative procedure consisting of sequential contact and frictional heating analysis and wear calculations is established. An example of a bi-material composite subject to linear wear has been presented as a proof-of-concept for the thermomechanical wear simulation tool. Using this thermomechanical wear model, the expected transitions from run-in to steady-state

wear regimes are still predicted, despite the complex coupling of contact pressure, frictional heat generation, temperature and wear rate at the sliding interface. Upon reaching steady-state, the contact pressure, temperature and wear rate all develop steady distributions, the worn surface profile converges to a constant shape, and the composite wear rate stabilizes at a constant value. Dramatic differences in the predictions of material volume loss (especially during run-in) and worn surface profile have been observed between the thermomechanical and mechanical-only wear simulation cases, indicating the importance of including thermal effects. The proposed sequential thermomechanical wear simulation routine lays the foundation for including thermal expansion, thermal stresses, and temperature-dependence for more than just the wear rates.

Chapter 5

Topology optimization for frictional heat dissipation with wear constraints

Contact temperature is one of the most critical factors that affect the performance and lifespan of tribological systems. As such, the management of frictional heat generated at sliding interfaces should be considered in the design process. Current practices often use material selection or cooling strategies as a means of addressing concerns about thermal management. This chapter presents the first application of topology optimization to design composites for efficient frictional heat dissipation during wear. Three-dimensional bi-material composites are optimized to minimize the average steady-state contact temperature. The optimization problem is formulated based on the steady-state heat transfer model with frictional heat flux boundary conditions presented in Chapter 4. Wear constraints are incorporated in

the optimization problem by prescribing fixed material area fractions or distributions at the sliding interface. The material thermal conductivity and frictional heat flux are interpolated using the Solid Isotropic Material with Penalization optimization method. The optimization problem is solved using a gradient-based optimizer, the Method of Moving Asymptotes, and sensitivities obtained by the adjoint method. Two case studies are presented to demonstrate the utility of the established optimization framework. The influence of several factors on the optimized designs are investigated, including: design-dependent frictional heating boundary conditions, material volume fraction constraints, as well as material tribological and thermal properties.

5.1 Topology optimization for thermal management

In many engineering systems such as electronic devices, heating appliances, combustion engines, and braking systems, thermal management is a critical design consideration along with other design requirements such as weight, stiffness and strength. During the past two decades, TO has been extensively applied for problems involving heat transfer, multiphysics, and manufacturing processes [106]. Many studies have focused more fundamentally on the development of appropriate optimization methods that involve both two- and three-dimension conduction, convection, and design-dependent and independent thermal loads and boundary conditions [106]. Yoon et al. [107] optimized a heat dissipating structure within a coupled thermo-hydraulic system under forced convection. Alexandersen et al. [108] designed passive cooling heat sinks for light-emitting diode (LED) lamps. Pizzolato et al. [109] unitlized topology optimization to design conductive fins for heat transfer enhancement in latent heat thermal energy storage systems. Related to additive manufacturing (AM)

processes, Zhou et al. [110] presented the design of support structures with efficient heat conduction capabilities for powder-bed-based laser AM. Allaire et al. [111] addressed the undesired thermal deformation and residual stresses caused by high temperatures during metallic AM in the topology optimization formulation.

However, to date, no previous work has exploited topology optimization in designing materials and structures for the dissipation of frictional heat generated at sliding interfaces. To address this opportunity, in this section, a topology optimization formulation, using the density-based SIMP approach, is presented. While the fundamental methods and algorithms of density-based topology optimization for general heat dissipation problems are well established, this dissertation presents a new application to both topology optimization and tribology communities.

5.1.1 Heat transfer model

The physical model that governs the frictional heating problem is the steady-state heat transfer model with appropriate boundary conditions. For convenience, the same heat transfer model, assumptions, and boundary conditions described in Section 4.1.2.1 are adopted:

$$\nabla \cdot (\boldsymbol{k} \nabla \boldsymbol{T}) = \boldsymbol{q}_{vol} \text{ in } \Omega, \tag{5.1}$$

$$\boldsymbol{T} = T_0 \text{ on } \Gamma_{\text{sink}}; \tag{5.2}$$

$$-\boldsymbol{k} \nabla \boldsymbol{T} \cdot \boldsymbol{n} = \dot{\boldsymbol{q}}_{surf} \text{ on } \Gamma_{\text{flux}}; \tag{5.3}$$

$$-\boldsymbol{k} \nabla \boldsymbol{T} \cdot \boldsymbol{n} = h(\boldsymbol{T} - T_{\text{ref}}) \text{ on } \Gamma_{\text{conv}}; \tag{5.4}$$

$$-\boldsymbol{k}\nabla\boldsymbol{T}\cdot\boldsymbol{n}=0 \text{ on } \Gamma_{\text{ins}}, \tag{5.5}$$

where $\boldsymbol{k}$ is the thermal conductivity, $\boldsymbol{T}$ is the temperature field, $\boldsymbol{q}_{vol}$ is the internal volumetric heat source, and $\dot{\boldsymbol{q}}_{surf}$ is the surface heat flux. By adopting the same finite volume method described in Section 4.1.2.2, the above governing equation can be represented in matrix form as:

$$\mathbf{AT}=\mathbf{b}, \tag{5.6}$$

where $\mathbf{A}$ is the global coefficient matrix depending on the conductivity distribution within the design domain and $\mathbf{b}$ is the thermal load vector containing both volumetric heat source and surface heat flux terms.

5.1.2 Frictional heat flux during steady-state wear

While in Section 4.2, sequential coupling of thermomechanical wear was investigated through temperature-dependent wear rates, here the wear rates are independent of temperature. Additionally, bi-material composite designs (materials A and B) are only optimized for steady-state wear conditions. For the bi-material composite systems of interest, It is assumed that each material has its own distinct wear rate, K_a and K_b. Then the wear rate distribution function, K, is piecewise constant and defined according to the material distribution at the sliding interface. Recall the discussion of steady-state in linear wear systems in Section 3.1.3: the contact pressure at the sliding interface reaches a steady distribution without further change, which can be directly calculated

$$P_{ss}=F_n\frac{(\int_{\Gamma_{sl}}(K)^{-1}dS)^{-1}}{K}, \tag{5.7}$$

where Γ_{sl} denotes the sliding interface. The resulting contact pressure distribution within the sliding interface is also piecewise constant with values of P_a in material A and P_b in material B (Figure 5.1(b))

$$P_a = \frac{F_n K_b}{K_a S_b + K_b S_a} \text{ and } P_b = \frac{F_n K_a}{K_a S_b + K_b S_a}, \tag{5.8}$$

where S_a and S_b are, respectively, the surface area occupied by material A and B at the sliding interface. The resulting steady-state composite wear rate is calculated using Equation 3.30

$$K^{ss}_{comp} = \frac{K_a K_b}{K_a S_b + K_b S_a}. \tag{5.9}$$

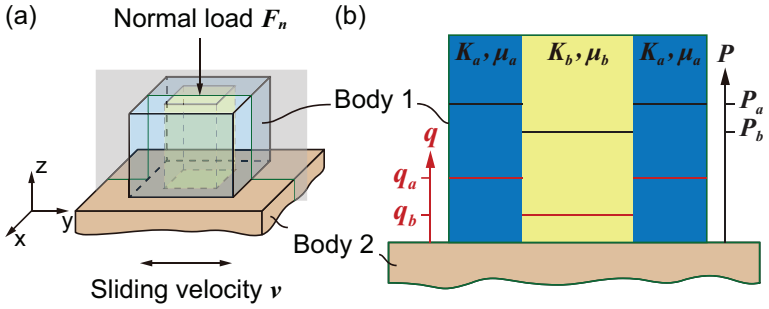

Figure 5.1: Schematic of linear sliding wear system. (a) Bi-material composite and operating conditions. (b) Cross-section view showing contact pressure and frictional heat flux distributions at the steady-state wear regime.

The frictional heat flux generated in each material domain can be calculated as the product of relative sliding velocity, coefficient of friction, and contact pressure. Upon reaching steady-state wear, the frictional heat generation rate in each material can be directly determined from the contact pressure distribution (Equation 5.8):

$$\dot{q}_a = v\mu_a P_a(K_a, S_a) \text{ and } \dot{q}_b = v\mu_b P_b(K_b, S_b), \tag{5.10}$$

where v is the relative sliding velocity, and μ_a and μ_b are the coefficient of friction between each material and the counter surface. The same conservative assumption for the heat partitioning explained in Chapter 4 is made here: the counter-body (Body 2) is non-conductive so that the frictional heat flux can only enter the sliding body (Body 1). Thus, the total frictional heat entering the sliding body is

$$q_{total} = \dot{q}_a S_a + \dot{q}_b S_b. \tag{5.11}$$

From the above calculation of frictional heat flux generated at the sliding interface, it is seen that (at steady-state and similar to contact pressure distributions) the frictional heat flux has a piecewise constant distribution corresponding to the material distribution within the sliding interface. In addition, the magnitude of the frictional heat flux in each material is determined by relative velocity between the sliding bodies, the tribological properties (coefficient of friction and wear rate) of the each material, and the area fraction of each material at the sliding interface. Thus, for a given material pair, the frictional heat flux distribution at the sliding interface depends on the material distribution. In Figure 5.1(b), the steady-state contact pressure (right) and frictional heat flux (left) at the sliding interface are plotted schematically illustrating the piecewise constant distributions.

5.1.3 Density-based topology optimization formulation

The topology optimization framework is formulated using the density-based method, Solid Isotropic Material with Penalization (SIMP; see Section 1.3) [112]. The design domain is discretized and each element is represented by a density variable, ρ_e, which corresponds to

its material composition. For an element occupied by material A, its density value is $\rho_e = 1$; for an element occupied by material B, its density value is $\rho_e = \rho_{\min}$. Element density can take any value between $\rho_{\min}$ and 1. Here, $\rho_{\min} = 10^{-3}$ is chosen to avoid computational difficulties such as singularity in the finite volume method [49].

The thermal conductivity of each element is interpolated by its density following the SIMP representation:

$$k_e = k_a \rho_e^p + k_b (1 - \rho_e^p), \tag{5.12}$$

where p is the penalization parameter that suppresses the formation of intermediate densities [112].

From the calculation in Section 5.1.2, it is known that, when the area fraction of each material is prescribed at the sliding interface, the magnitude of the frictional heat flux in each material is also prescribed (Equation (5.10)). Then the steady-state frictional heat flux distribution is piecewise constant corresponding to the material distribution at the sliding interface. Then, the same interpolation scheme used for thermal conductivity is also applied to the frictional heat flux at the sliding interface:

$$\dot{q}_e = \dot{q}_a \rho_e^p + \dot{q}_b (1 - \rho_e^p), \tag{5.13}$$

where $\dot{q}_a$ and $\dot{q}_b$ are the frictional heat flux generated at each material at steady-state from Equation (5.10). Thus, the heat flux boundary condition (Equation (4.5)) is design-dependent (if the material distribution at the sliding interface is not prescribed).

As the sliding interface will usually be most critical in terms of absolute temperatures,

the objective function of interest is minimizing the average temperature at the sliding interface, Γ_{sl}. The objective function is formulated as:

$$f = \frac{1}{|\Gamma_{sl}|} \int_{\Gamma_{sl}} \mathbf{T} dS = \mathbf{c}^T \mathbf{T}. \tag{5.14}$$

This is chosen as a first objective to address because it it straightforward, tractable, and physically relevant to the thermal performance. In addition, it has been noted in previous studies that using the average temperature as the objective function is also effective for reducing the maximum temperature [113, 114]. Maximum temperature is often of concern and should remain below transition or critical temperatures specific to particular materials. While not used explicitly in the objective function here, later in the analysis the maximum temperature in each material at the sliding interface will also be monitored to evaluate thermal performance of the optimized composites.

Besides the box constraint on the element density ($\rho_{\min} \leq \rho_e \leq 1$), another constraint considered is the volume occupied by material A in the design domain:

$$g_1(\boldsymbol{\rho}) = \int_{\Omega} \boldsymbol{\rho} dV - V_a = 0. \tag{5.15}$$

This constraint represents a typical material resource constraint that could be related to considerations of cost, environment, recyclability, etc. In addition, the material area fraction of material A at the sliding interface can also be constrained to maintain target wear performance:

$$g_2(\boldsymbol{\rho}) = \int_{\Gamma_{sl}} \boldsymbol{\rho} dS - S_a = 0. \tag{5.16}$$

Recall that for the assumptions and conditions outlined in Section 5.1.2, prescribing ma-

terial area fractions at the sliding interface effectively determines the steady-state wear performance for the composite (Equation (5.9)) and the total heat generated at the sliding interface (Equation (5.11)). Lastly, a total heat generation constraint at the sliding interface is enforced :

$$g_3(\boldsymbol{\rho}) = \int_{\Gamma_{sl}} \dot{\boldsymbol{q}} dS - q_{total} = 0. \tag{5.17}$$

This constraint is equivalent to the material area fraction constraint (Equation (5.16)) and is needed to suppress formation of intermediate (non-physical) densities at the sliding interface.

Therefore, the topology optimization problem can be written as:

$$\begin{aligned} \min_{\boldsymbol{\rho}} \quad & f(\mathbf{T}) = \mathbf{c}^{\mathrm{T}}\mathbf{T}, \\ \text{s.t.} \quad & \mathbf{AT} = \mathbf{b}, \\ & \boldsymbol{g}(\boldsymbol{\rho}) = \mathbf{0},\ \rho_{\min} \leq \rho_e \leq 1,\ e = 1, 2, ..., N_e, \end{aligned} \tag{5.18}$$

where $\boldsymbol{g}(\boldsymbol{\rho})$ is the vector containing all of the equality constraints applied.

5.1.4 Implementation

In this section, the detailed implementation of the topology optimization formulation established in the previous section is described, including the adjoint sensitivity analysis, sensitivity filter, and optimization algorithm. The topology optimization procedure is implemented in MATLAB 2017a (The MathWorks, Inc., Natick, MA).

5.1.4.1 Sensitivity analysis

To implement a gradient-based optimization algorithm to solve Equation (5.18), sensitivity analysis is performed using the adjoint method. The sensitivity of the objective function $f(\mathbf{T}) = \mathbf{c}^{\mathrm{T}}\mathbf{T}$ with respect to the design variable ρ_e can be written as:

$$\frac{\partial f}{\partial \rho_e} = \frac{\partial \mathbf{c}^{\mathrm{T}}}{\partial \rho_e}\mathbf{T} + \mathbf{c}^{\mathrm{T}}\frac{\partial \mathbf{T}}{\partial \rho_e}. \tag{5.19}$$

In this expression, the direct evaluation of $\frac{\partial \mathbf{T}}{\partial \rho_e}$ is cumbersome because $\mathbf{T}$ depends on $\partial\rho_e$ implicitly. The temperature vector, $\mathbf{T}$, is solved from the linear equation system, $\mathbf{AT} = \mathbf{b}$ governing the heat transfer problem (Equation 5.1), where both the matrix $\mathbf{A}$ and the vector $\mathbf{b}$ are dependent on ρ_e.

An adjoint state, $\boldsymbol{\lambda}$, is introduced. The objective function $f(\mathbf{T})$ is rewritten by adding an zero function as:

$$f(\mathbf{T}) = \mathbf{c}^{\mathrm{T}}\mathbf{T} - \boldsymbol{\lambda}^{\mathrm{T}}(\mathbf{AT} - \mathbf{b}), \tag{5.20}$$

where $\boldsymbol{\lambda}^{\mathrm{T}}$ can be any arbitrary vector since $(\mathbf{AT} - \mathbf{b})$ always gives zero vectors. Differentiating Equation (5.20) gives

$$\frac{\partial f}{\partial \rho_e} = \frac{\partial \mathbf{c}^{\mathrm{T}}}{\partial \rho_e}\mathbf{T} + \mathbf{c}^{\mathrm{T}}\frac{\partial \mathbf{T}}{\partial \rho_e} + \boldsymbol{\lambda}^{\mathrm{T}}(\frac{\partial \mathbf{A}}{\partial \rho_e}\mathbf{T} + \mathbf{A}\frac{\partial \mathbf{T}}{\partial \rho_e} - \frac{\partial \mathbf{b}}{\partial \rho_e}). \tag{5.21}$$

The above equation can be rearranged into

$$\frac{\partial f}{\partial \rho_e} = \frac{\partial \mathbf{c}^{\mathrm{T}}}{\partial \rho_e}\mathbf{T} + \boldsymbol{\lambda}^{\mathrm{T}}(\frac{\partial \mathbf{A}}{\partial \rho_e}\mathbf{T} - \frac{\partial \mathbf{b}}{\partial \rho_e}) + (\mathbf{c}^{\mathrm{T}} + \boldsymbol{\lambda}^{\mathrm{T}}\mathbf{A})\frac{\partial \mathbf{T}}{\partial \rho_e}. \tag{5.22}$$

Since $\boldsymbol{\lambda}$ is arbitrary, it can be chosen to be the solution of $\mathbf{A}^{\mathrm{T}}\boldsymbol{\lambda} = -\mathbf{c}$, which gives $\mathbf{c}^{\mathrm{T}} + \boldsymbol{\lambda}^{\mathrm{T}}\mathbf{A} = \mathbf{0}$. Here, $\boldsymbol{\lambda}$ is the adjoint state. Sensitivities of the objective function with respect to design variables can be calculated as:

$$\frac{\partial f}{\partial \rho_e} = \frac{\partial \mathbf{c}^{\mathrm{T}}}{\partial \rho_e}\mathbf{T} + \boldsymbol{\lambda}^{\mathrm{T}}\left(\frac{\partial \mathbf{A}}{\partial \rho_e}\mathbf{T} - \frac{\partial \mathbf{b}}{\partial \rho_e}\right). \tag{5.23}$$

The objective function to minimize is the average temperature at the sliding interface (Equation (5.14)), where the definition of the coefficient vector $\mathbf{c}^{\mathrm{T}}$ is constant resulting in

$$\frac{\partial \mathbf{c}^{\mathrm{T}}}{\partial \rho_e} = 0. \tag{5.24}$$

The dependence of $\mathbf{A}$ on ρ_e is determined through through the interpolation of thermal conductivity:

$$\frac{\partial \mathbf{A}}{\partial \rho_e} = \frac{\partial \mathbf{A}}{\partial k_e}\frac{\partial k_e}{\partial \rho_e}, \tag{5.25}$$

where $\frac{\partial k_e}{\partial \rho_e} = p(k_a - k_b)\rho_e^{p-1}$ is found according to the interpolation scheme in Equation (5.12). When the frictional heat flux is the only heat input and its distribution is not prescribed but dependent on the material distribution at the sliding interface, the dependence of the thermal load vector $\mathbf{b}$ on ρ_e is found through the interpolation of frictional heat flux:

$$\frac{\partial \mathbf{b}}{\partial \rho_e} = \frac{\partial \mathbf{b}}{\partial \dot{q}_e}\frac{\partial \dot{q}_e}{\partial \rho_e}, \tag{5.26}$$

where $\frac{\partial \dot{q}_e}{\partial \rho_e} = p(\dot{q}_a - \dot{q}_b)\rho_e^{p-1}$ is found according to the interpolation scheme in Equation (5.13).

5.1.4.2 Sensitivity filter

In order to eliminate mesh dependency and encourage discrete designs, a filter technique is used on the obtained sensitivities of the objective function and constraints [112, 115]. The sensitivity filter utilized here is the one originally proposed by Sigmund [116].

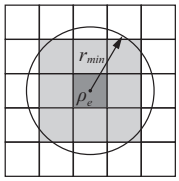

Figure 5.2: Schematic of sensitivity filter neighborhood defined by filter radius r_{min}.

The sensitivities are modified as weighted averages of the sensitivities within a fixed neighborhood. As illustrated in Figure 5.2, the neighborhood of an element, e, named N_e, includes the elements that are within a given filter radius r_{min} of the element e, i.e.

$$N_e = \{i \mid ||\mathbf{x}_i - \mathbf{x}_e|| \leq r_{min}\}, \tag{5.27}$$

where $\mathbf{x}_i$ denotes the spatial location of the element, i. Then the sensitivity of the design variable, ρ_e, is modified as

$$\frac{\widetilde{\partial f}}{\partial \rho_e} = \frac{\sum\limits_{i \in N_e} w(\mathbf{x}_i)\rho_i \frac{\partial f}{\partial \rho_i}}{\rho_e \sum\limits_{i \in N_e} w(\mathbf{x}_i)}, \tag{5.28}$$

where the weighting function $w(\mathbf{x}_i)$ is defined as a linearly decaying function

$$w(\mathbf{x}_i) = r_{min} - ||\mathbf{x}_i - \mathbf{x}_e||. \tag{5.29}$$

5.1.4.3 Optimization algorithm

With the derived and filtered sensitivities, the optimization problem for the given objective function and constraints can be iteratively solved by an optimizer until a stop criterion is reached. Topology optimization problems are usually nonlinear optimization problems with a large number of design variables. Various optimization methods have been developed and applied to solve these problems, including the Optimality Criteria (OC) method [49], Sequential Quadratic Programming (SQR) [117], the primal-dual interior point method [118], etc. In this dissertation, the standard Method of Moving Asymptotes (MMA) is applied. MMA was initially developed to solve nonlinear structural optimization problems by Svanberg [119]. It has been widely utilized in density-based topology optimization problems and has been demonstrated as a robust and versatile method for large scale problems [49].

5.1.4.4 Topology optimization procedure

The topology optimization procedure is shown in the flow chart of Figure 5.3. Provided with all the necessary input parameters and boundary conditions, the algorithm is initialized by an initial guess for the design variables. Based on the initialization, the numerical analysis yields the initial temperature field within the sliding body. Then the objective function and constraints are evaluated. Using the adjoint method, the sensitivities of the objective function and prescribed constraints are computed and subsequently filtered. Based on the calculation of the objective function, the design variables, and sensitivities, the design variables can be updated using the optimization solver. These steps are repeated until the convergence criterion is met or a maximum number of optimization steps is reached. Although in applying the SIMP method, it is possible to discourage the formation of inter-

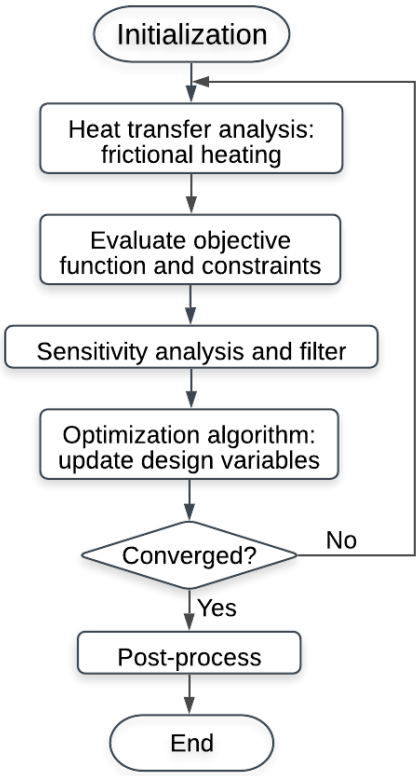

Figure 5.3: Flow chart of the topology optimization procedure.

mediate densities, it is not guaranteed that the final design is free of intermediate densities. Thus, post-processing is typically needed in order to obtain a discrete black/white final design with no intermediate densities. Here, a thresholding method with a threshold of 0.5 is applied. The final density of an element, $\tilde{\rho}_e$, is determined by

$$\tilde{\rho}_e = \begin{cases} 0, & \text{if } \rho_e < 0.5, \\ 1, & \text{if } \rho_e \geq 0.5. \end{cases} \tag{5.30}$$

5.1.5 Initial check: heat conduction with volumetric heat source

A test case is presented in this section to proof the established topology optimization routine. The problem of interest is a classical heat conduction optimization problem, where the distribution of conductive material in a design domain with internal heat generation is optimized for cooling purpose.

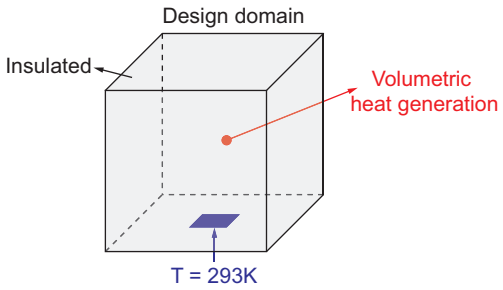

Figure 5.4: Design domain and boundary conditions of the test case.

In this test case, a fixed cubic design domain is used (as shown in Figure 5.4) with dimensions of 0.1m $\times$ 0.1m $\times$ 0.1m and it is discretized into 20 $\times$ 20 $\times$ 20 elements. All boundaries of the design domain are insulated except for a square region located at the center of the bottom face. This square region has a constant uniformly distributed temperature of $T_0 = 297$K. A volumetric heat source is uniformly distribution within the domain, $q = 0.005\text{W/m}^3$. The design domain consists of two materials: Material A with thermal conductivity $k_a = 100\text{W/(mK)}$ and Material B with thermal conductivity $k_b = 0.1\text{W/(mK)}$. The volume fraction constraint on the high-conductivity Material A is set as 20%. The objective is to find the optimal material distribution that minimizes the steady-state average temperature within the whole design domain.

Figure 5.5 shows the optimized composite structure, separately highlighting Material A in blue and Material B in yellow. It is seen that the high-conductivity Material A forms

a tree-like structure with branches extending into the design domain. The origin of the structure is located at the square region with fixed temperature. This type of design is expected because the square heat sink is the only region where heat can escape from the domain and the high-conductivity branches form conduction paths towards the heat sink.

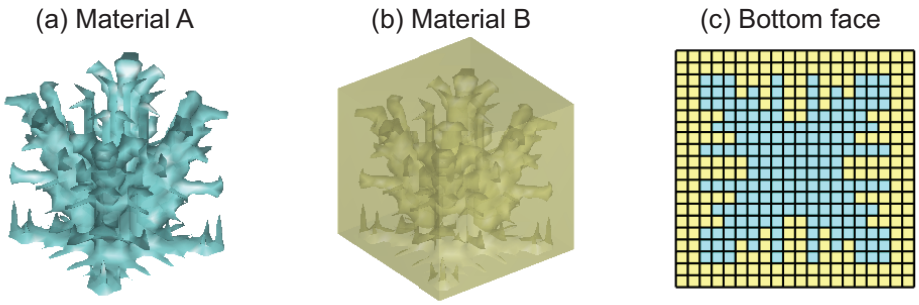

Figure 5.5: Optimization results of heat conduction teat case. (a) Material distribution of material A. (b) Material distribution of material B. (c) Material distribution at the bottom face.

In addition, the optimized design is symmetric with respect to the orthogonally oriented planes, which is consistent with the symmetric nature of the heat conduction problem. This symmetry is leveraged to reduce computational costs in later optimization cases where only a quarter of the whole design domain is need for computation (Figure 5.7).

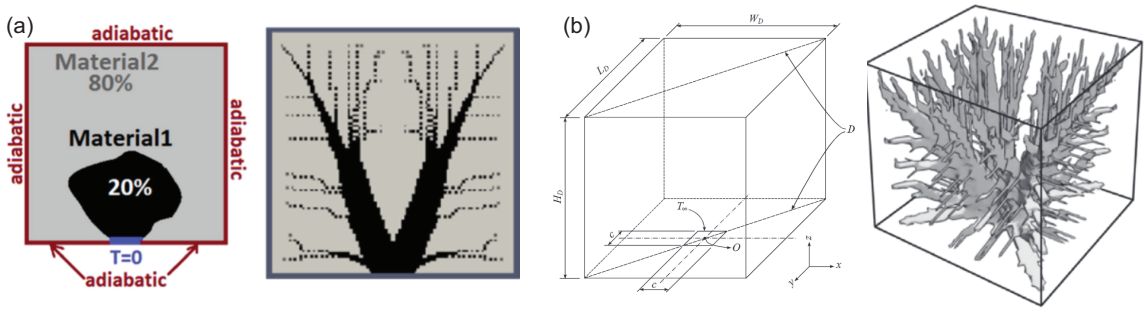

Figure 5.6: Results for optimal heat conduction problems. (a) Two-dimensional example from [106]. (b) Three-dimensional example from [120].

The tree-like structure observed in Figure 5.5 is a common feature in optimal heat conduction problems solved via topology optimization [49, 106, 120, 121]. Figure 5.6 shows two selected optimization results for two-dimensional [106] and three-dimensional [120] heat

conduction problems from the literature. This test case is used for initial trouble-shooting of the optimization framework in MATLAB. That similar results to cases published in the literature are achieved, suggests that the framework is ready for use in the following sections. The components of the optimization have already been independently verified or validated in previous sections.

5.2 Case studies for frictional heat dissipation

In this section, two case studies are presented to demonstrate the utility of the proposed topology optimization framework. The design domain and thermal boundary conditions are illustrated in Figure 5.7. Dimensions of the full design domain in Figure 5.7(a) are $L = W =$ 0.2m and $H = 0.1$m. Only a quarter of the domain is optimized due to symmetry (Figure 5.7(b)), with dimensions of $L_Q = W_Q = H = 0.1$m; the quarter domain is discretized into $30 \times 30 \times 30$ elements. The normal load applied on the whole sliding body is $F_n = 25000$N resulting in an average contact pressure of $P_0 = 0.625$MPa. The relative sliding velocity is $v = 0.2$m/s and the heat partitioning factor is set as $\alpha = 1$. The heat sink temperature is $T_0 = 293$K and ambient temperature is $T_{\text{ref}} = 293$K. For the case with convective boundary conditions, the heat transfer coefficient is set as $h = 50\text{W}/(\text{m}^2\text{K})$ representing typical convective heat transfer with air. These geometric, loading, and sliding parameters are chosen so that realistic heat flux for the material pairs will be achieved.

The optimization will be performed for two different material pairs: a metal/polymer and a metal/ceramic, which represent two common composite systems in tribological applications [122]. The material properties are displayed in Table 5.1 using representative values so the analysis remains general. In both pairs, the representative metal (Material A) is the

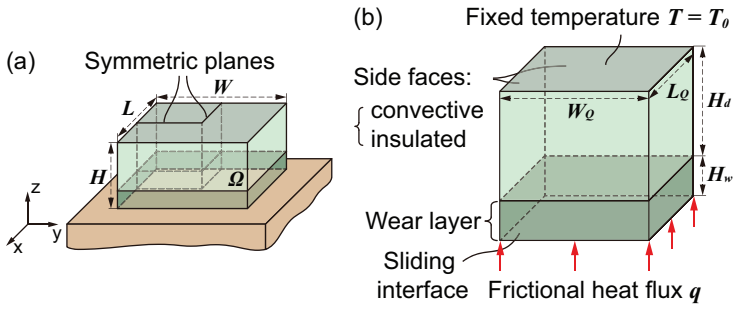

Figure 5.7: Schematic of the design domain for topology optimization. (a) Full design domain. (b) Quarter computational domain with boundary conditions.

Property	Pair 1		Pair 2	
	Metal (A)	Polymer (B)	Metal (A)	Ceramic (B)
Thermal conductivity, k [W/(mK)]	250	0.5	250	2.5
Wear rate, K [mm^3/(Nm)]	1e-5	1e-4	1e-5	1e-6
Coefficient of friction, μ	0.4	0.1	0.4	0.8

Table 5.1: Material properties for Pair 1 and Pair 2.

more thermally conductive material. In Pair 1, the metal has a lower wear rate (more wear resistant) and a higher coefficient of friction than the polymer (material B). In Pair 2, the ceramic (material B) is more wear resistant and has a higher coefficient of friction than metal.

5.2.1 Case Study 1: heat dissipation optimization with constrained steady-state wear performance

As discussed in Section 5.1.2, the steady-state wear performance of composite surfaces (measured by K^{ss}_{comp}, Equation (5.9)) and the magnitude of frictional heat flux generated within each material domain at the sliding interface (Equation (5.10)) can be calculated from the area fraction and properties of each constituent material at the sliding interface. However, how the materials are distributed at the sliding interface determines the piecewise

distribution of the frictional heat flux, which directly relates to the thermal field within the composite body. In this case study, the role of the material distribution at the sliding interface on the heat dissipation optimization is investigated by incorporating the design-dependent frictional heating boundary conditions as discussed in Section 5.1.3.

5.2.1.1 Case Study 1: problem setup

The design domain is shown in Figure 5.7, where the side faces are convective with the ambient environment. Composite structures using both material pairs (Table 5.1) are optimized with a total volume fraction constraint on the amount of metal (Material A) available. The area fraction of each material at the sliding interface is fixed to be 50%, which results in maintaining a target steady-state composite wear rate of the composite surface (Equation (5.9)) and also the frictional heat flux within each material (Equation (5.10)). However, there is no pre-assumption of the material arrangement or distribution at the sliding interface, only the surface area fraction is fixed. The design domain including the sliding interface is subject to change during the optimization. However, in order to guarantee an acceptable target wear performance of the final composite, a wear layer with a thickness of $H_w = 10\%H$ is created in the design domain, Ω, as shown in Figure 5.7(b). The material distribution within the wear layer is always a vertical extrusion of the current design at the sliding interface during the optimization. This is realized by proposing additional constraints on the design variables within the wear layer. The optimization process starts with an initial structure made up entirely of material A (metal), i.e. all densities are equal to 1 in the first iteration. Following standard practices [112], the penalization parameter, p, increases linearly from 1 to 3 during the first 50 iterations and then is kept at 3 afterwards.

For Pair 1 (metal/polymer), the frictional heat flux in each material is calculated by Equation (5.8) as $\dot{q}_a = 4.55 \times 10^4 \mathrm{W/m}^2$ and $\dot{q}_b = 1.14 \times 10^3 \mathrm{W/m}^2$, and the total heat generation rate is $q_{total} = 932.8\mathrm{W}$. Two examples are optimized with a metal volume fraction in the whole design domain set as 30% and 50%. For both of these examples, since metal occupies 50% in the wear layer with a thickness of $H_w = 10\%H$ (which is equivalent to 5% of the total volume), the metal above the wear layer is effectively constrained to be 25% and 45%, respectively. The same two examples are performed for Pair 2 (metal (A) and ceramic (B)), where the metal volume fraction in the whole design domain set as 30% and 50% while the area fraction of each material at the sliding interface is fixed to be 50%. The frictional heat flux for each material is found as $\dot{q}_a = 4.55 \times 10^3 \mathrm{W/m}^2$ and $\dot{q}_b = 9.09 \times 10^4 \mathrm{W/m}^2$, and the total heat generation rate is $q_{total} = 1909\mathrm{W}$. Here, the ceramic generates more frictional heat but is less conductive.

5.2.1.2 Case Study 1: results and discussion

Convergence curves of the objective function and constraint on the total heat generation are shown in Figure 5.8. For both cases, the objective function increases initially and decreases after the total heat generation constraint is satisfied. All of the equality constraints are active and satisfied when convergence is reached after 200 optimization iterations. The final optimized composite structures are presented in Figure 5.9. Both the quarter design domain and the full structure are shown; the constituents are shown separately - metal (blue) and polymer (gray). The material and temperature distributions at the sliding interface are also shown.

Similar optimized structures are obtained for both prescribed total volume fractions

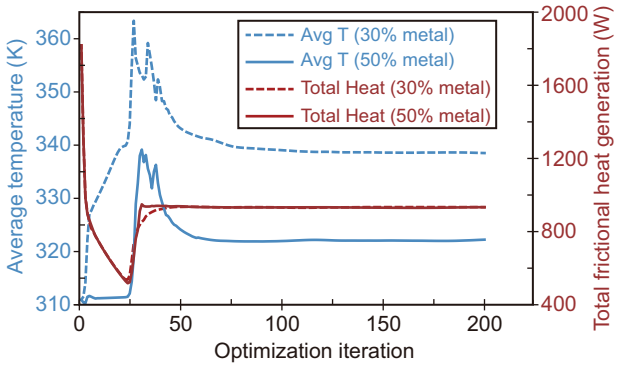

Figure 5.8: Convergence curves showing the objective function and the total frictional heat generation rate constraints for Pair 1 (metal/polymer) with total metal volume fractions of 30% and 50%.

(30% and 50% metal). From the results one can see that, at the sliding interface, metal is distributed near the boundaries and polymer is concentrated in the center with slight differences in the shape. This is expected as convection improves the dissipation of the high frictional heat generated in the metal (compared to the polymer). Above the wear layer, the metal forms a conductive path to the heat sink at the top surface. Four metal columns are formed with branches spreading out over the central polymer domain in the wear layer. The effectiveness of the design can be observed from the temperature distribution shown in Figure 5.9(c) and (f). The temperature in the polymer is generally higher than in the metal while in the area connected with the metal columns, the temperature is reduced. The average temperature at the sliding interface and the maximum interface temperature in each material for both optimized structures are displayed in Table 5.2. The results are as expected in that for the optimized structures, increasing the metal volume fraction would enhance the heat dissipation capacity of the composites resulting in a lower average temperature at the sliding interface. In addition, the maximum temperature in each material drops with increased metal volume fraction, which shows that choosing average temperature as an objective function is also effective for decreasing the maximum temperature in both

materials.

For comparison, a reference composite structure with a metal volume fraction of 50% as shown in Figure 5.10(a) is also analyzed. The material distribution of the reference structure is a direct extrusion from the sliding interface with 50% metal distributed outside and 50% polymer concentrated inside. The optimized structure with 50% metal achieves lower average temperature than the reference structure and the optimized structure with 30% metal achieves comparable average temperature to the reference structure. Despite the maximum temperatures in the metal being higher in the two optimized structures than the reference structure, both optimized structures provide significant reduction in the maximum temperatures in the polymer compared to the reference structure.

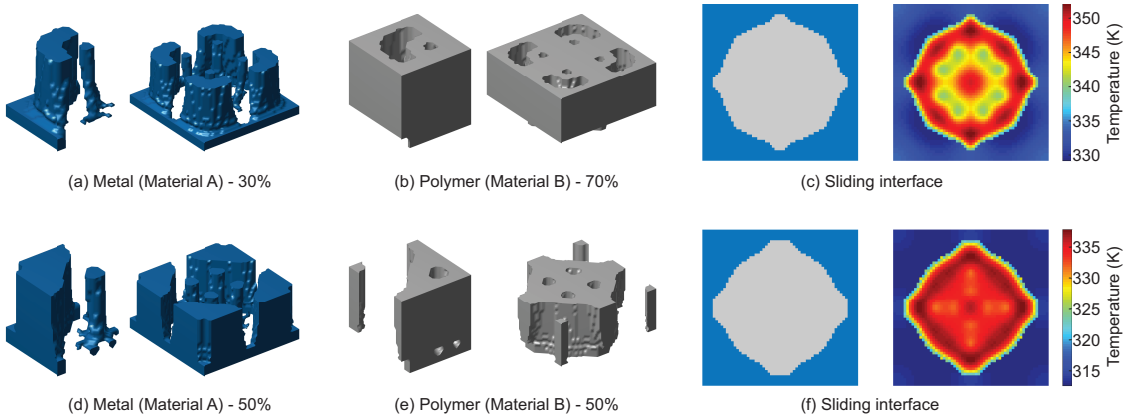

Figure 5.9: Optimization results for Case Study 1 of Pair 1 (metal/polymer) with metal total volume fractions of 30% (a,b,c) and 50% (d,e,f). The composite structure is shown in the quarter (left) and full (right) domains, highlighting separately the metal (a,d) and polymer (b,e) constituents. (c,f) Temperature distribution at the sliding interface of the optimized structures.

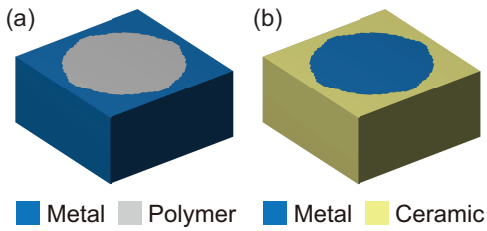

Figure 5.10: Reference composite structures with a metal total volume fraction of 50% for both material pairs. (a) Pair 1: metal/polymer. (b) Pair 2: metal/ceramic.

The optimized composite structures for Pair 2 are shown in Figure 5.11 with the metal volume fractions again set as 30% and 50% in the whole design domain. At the sliding interface, metal is mainly placed at the center surrounded by ceramic. This is consistent with the previous results in that the material generating more heat (this time being the ceramic) is placed along the convective boundaries. At the sliding interface, there are also small metal inclusions distributed in the ceramic, which end up forming connected root-like conduction paths through the height of the structure at the four corners. These interfacial inclusions also increase the contact area between the two materials which enhances heat conduction from the ceramic to the metal. The temperature at the sliding interface is much higher in the ceramic than the metal while lower temperature values are observed near material interfaces. The temperature results in Table 5.2 show the same trends as for material Pair 1 (metal/polymer), i.e. average and maximum temperatures at the sliding interface decrease as the metal volume fraction increases.

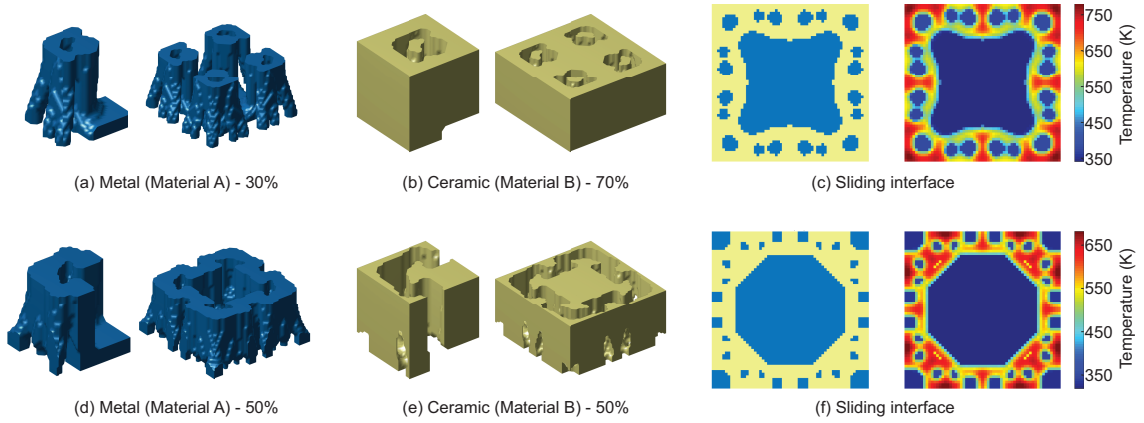

Figure 5.11: Optimization results for Case Study 1 of Pair 2 (metal/ceramic) with metal total volume fractions of 30% (a,b,c) and 50% (d,e,f). The composite structure is shown in the quarter (left) and full (right) domains, highlighting separately the metal (a,d) and ceramic (b,e) constituents. (c,f) Temperature distribution at the sliding interface of the optimized structures.

A reference structure with 50% metal as shown in Figure 5.10(b) is analyzed for com-

parison, where metal is concentrated inside surrounded by ceramic. Significant reductions of average temperature and maximum temperature in the ceramic are obtained in the two optimized structures compared with the reference structure. In particular, there is a 22% reduction of the average temperature and a 37% reduction of the maximum temperature in the ceramic domain of the optimized structure with a total metal volume fraction of 30% compared to the reference structure. For the optimized structure with a total metal volume fraction of 50%, 29% and 45% reductions in the average temperature and maximum temperature in the ceramic domain are achieved.

Materials	Volume fraction metal	Average T [K] (sliding interface)	Maximum T [K]	
			metal	polymer/ceramic
Pair 1 (metal/polymer)	30%	339	334	352
	50%	323	314	338
	50% (Ref)	338	311	399
Pair 2 (metal/ceramic)	30%	485	383	779
	50%	441	347	681
	50% (Ref)	623	325	1228

Table 5.2: Summary of temperature values monitored in the optimized structures for Case Study 1.

Comparing the optimization results (Table 5.2) for the two material pairs, it is noted that the optimized composite structure for frictional heat dissipation depends strongly on the prescribed total material volume fractions, as well as on the relative thermal and tribological properties of the constituents. When the materials are allowed to distribute freely at the sliding interface with constrained area fractions (i.e. constrained steady-state wear performance) and frictional heat dissipation is the only design consideration, vastly different composite configurations are obtained at the sliding interface depending on the particular material pair and material volume fraction constraints. This is an indication of the

strong correlation between the design-dependent frictional heating boundary condition and the optimized composite design for heat dissipation performance. In this case study, the steady-state wear performance of the sliding interface is constrained by the fixed area fractions of the constituents; however, it is known that the run-in performance (run-in volume loss) for linear abrasive wear is also dependent on the material distribution (with fixed area fractions) [76, 77, 93]. The optimized structures with different material distributions at the sliding interface may lead to different run-in wear performance. Thus for future studies, it is necessary to couple both wear (including run-in) and frictional heat dissipation in the design process to achieve optimal multifunctionality of the composites. A first attempt at doing this in a sequentially coupled fashion is presented next.

5.2.2 Case Study 2: sequentially coupled wear and heat dissipation optimization

This section presents a case study of a sequentially coupled wear and heat dissipation optimization. First, a wear-optimal material distribution is determined at the sliding interface and within the wear layer. Based on this, prescribed distribution, the remainder of the design domain is optimized for heat dissipation. A unit-cell of a periodic 3D composite structure consisting of metal and ceramic (Material Pair 2) is optimized for frictional heat dissipation.

5.2.2.1 Case Study 2: problem setup

It has been noted previously in Section 5.1.2 that for linear abrasive composite wear systems, the steady-state wear performance only depends on the material area fractions and not on

the material distribution, while the run-in performance changes with material distribution [76, 77, 93]. Figure 5.12(a) illustrates schematically the typical volume loss versus sliding distance curves for two composite surfaces with the same material area fractions but different configurations (representing the surfaces of initial guess and iteration 100 shown in Figure 5.12(a), respectively). Both curves converge to lines with the same slope (i.e. same steady-state wear rate) at steady-state wear conditions. The run-in volume loss is shown as the y-intercept of the steady-state volume loss lines, which, however, differ for the different composite configurations; the run-in volume loss is also an important criteria for evaluating the wear performance of composites. A topology optimization framework based on the level-set method was previously proposed for optimizing periodic bi-material composite surfaces to minimize the run-in volume loss [40]. This tool has also been validate by extensive wear tests [123]. From Gretjak et al. [123], an optimization sequence (showing select iterations) of the unit-cell design of a periodic bi-material composite surface is shown in Figure 5.12(b). The objective was to minimize run-in volume loss subject to material resource constraints (50% metal and 50% ceramic) and a basic manufacturing complexity constraint [123].

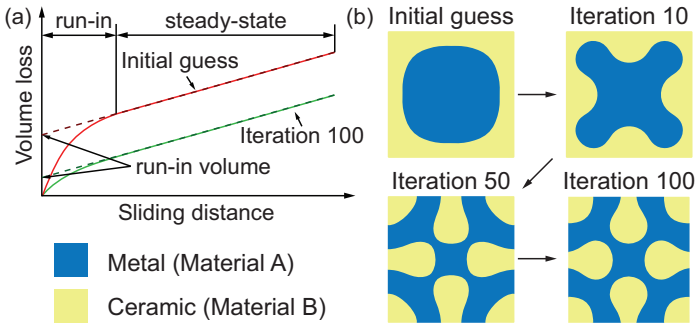

Figure 5.12: (a) Typical wear volume loss versus sliding distance curves showing run-in and steady-state regimes. (b) Optimization sequence (showing select iterations) of a bi-material composite surface for minimal run-in volume loss [123].

The design domain is shown in Figure 5.7. Periodic boundary conditions are applied to all side faces. These side faces can be treated as insulated boundaries because the

optimized material distributions are always symmetric within the unit-cell and thus also result in thermal symmetry. The previously obtained 2D composite configuration in Figure 5.12(b) [123] is taken as the pre-defined material distribution at the sliding interface and extruded through the wear layer with a thickness of $H_w = 10\%H$: this time the prescribed interface and the entire wear layer are not subject to change during the optimization while the remainder of the design domain is optimized for heat dissipation. The frictional heat flux generated in each material is calculated using Equation (5.10): for the metal $\dot{q}_a = 4.55 \times 10^3 \mathrm{W/m^2}$ and for the ceramic $\dot{q}_b = 9.09 \times 10^4 \mathrm{W/m^2}$, and the total heat generation rate is $q_{total} = 1909\mathrm{W}$.

5.2.2.2 Case Study 2: results and discussion

The optimized unit-cell composite structure as well as a 2-by-2 layout of the metal portion of the unit-cell is shown in Figure 5.13(a-c) where a total metal volume fraction constraint of 30% was applied. It is seen that, in general, the distribution of metal and ceramic flips immediately above the wear layer (see cross-sectional material distributions at two selected positions shown in Figure 5.13(d) both within and directly above the wear layer). Metal forms root-like structures which connect with the ceramic in the wear layer to conduct the heat out through the top face (the sides are no longer available for heat dissipation as they are insulated).

The optimization procedure for this case study was repeated under different total volume fraction constraints on the metal ranging from 20% to 80%. For comparison, a reference case with a metal volume fraction of 50% is also analyzed, where the material distribution is a direct extrusion from the original optimized sliding interface, as shown in Figure 5.14.

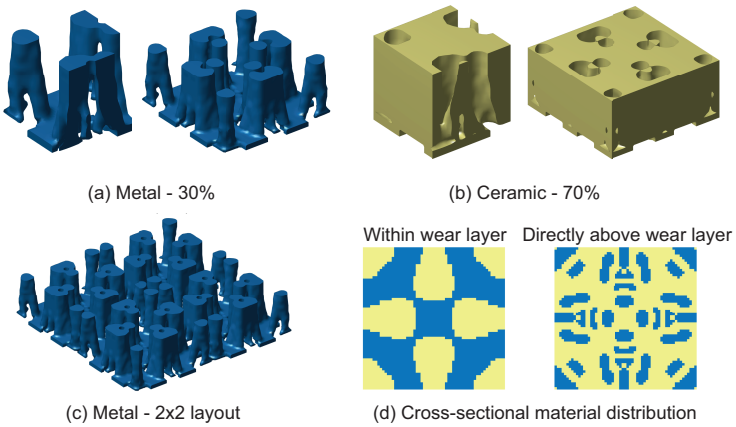

Figure 5.13: Optimization results for Case Study 2 with a metal total volume fraction of 30%. (a,b) Unit-cell composite structure is shown in the quarter (left) and full (right) domains, highlighting separately the metal (a) and ceramic (b) constituents. (c) 2-by-2 layout of optimized unit-cell, showing only the metal. (d) Cross-sectional material distribution at two selected positions: within the wear layer (left) and directly above the wear layer (right).

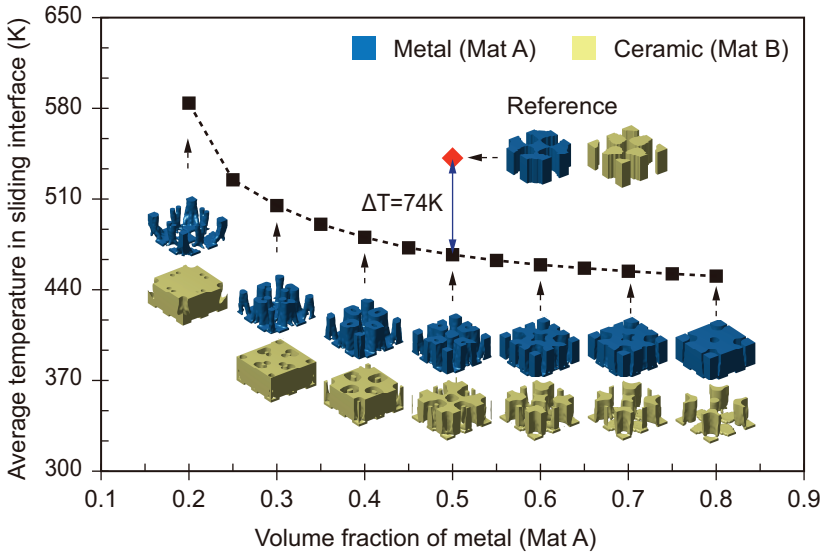

Figure 5.14: Objective function results for Case Study 2 with metal total volume fraction ranging from 20% to 80%. A reference case is included for comparison.

Figure 5.14 also plots the objective function versus the total volume fraction of metal and displays several of the corresponding optimized composite structures (highlighting the constituents separately: metal in blue and ceramic in yellow). The maximum temperatures in both the metal and ceramic at the sliding interface are plotted against the metal volume fraction in Figure 5.15. Generally, the optimized material distributions follow a common

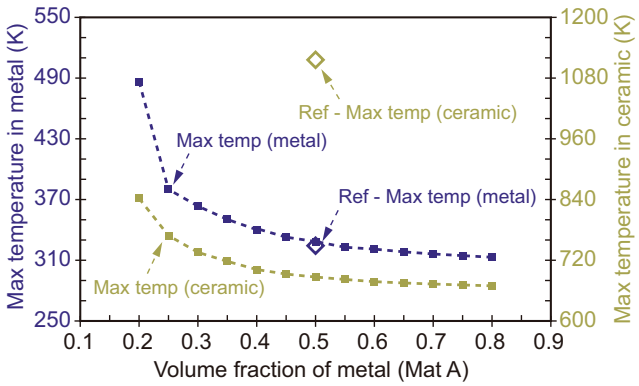

Figure 5.15: Maximum temperature in each material for Case Study 2 with a metal total volume fraction ranging from 20% to 80% and reference case.

trend: above the wear layer, metal tends to be distributed on top of the ceramic and forms connected conduction paths to the top face (heat sink).

Significant improvement in heat dissipation is observed by comparing the temperature values of the optimized structures and also taking the reference case into consideration. The average temperature at the sliding interface (Figure 5.14) of the reference case with 50% metal (542K) is higher than the multifunctional optimized structure with only 25% metal (525K) as well as higher than the multifunctional optimized structure with 50% metal (467K). The maximum temperature in the ceramic at the sliding interface (Figure 5.15) is significantly reduced by the heat dissipation optimization compared to the wear-optimal reference structure. In particular, the optimized structure with only 20% metal obtains a maximum temperature of 850K, which is a 25% reduction compared to the reference case with 50% metal (1132K). For the optimized structure with 50% metal (694K), there is a 39% reduction of the maximum temperature compared to the reference case with the same amount of metal. In addition, the average and maximum temperatures at the sliding interface all decrease as the metal volume fraction is increased, but at a decreasing rate with diminishing returns. After the metal volume fraction reaches up to 50%, adding more

metal in the domain only results in a small decrease in the temperatures, 467K (50%) - 451K (80%), which offers limited improvement in terms of heat dissipation capability. The observation of the diminishing returns in heat dissipation improvement provides important information for the design of tribological composites especially when cost or material resources are critical factors.

5.3 Summary

A density-based topology optimization framework has been presented to design three-dimensional bi-material composites for frictional heat dissipation associated with wear at sliding interfaces. The first case study investigates the influence of design-dependent frictional heat flux boundary conditions on the optimized designs for both metal/polymer and metal/ceramic composites. It is found that the optimized composite designs highly depend on the relative tribological and thermal properties as well as volume fractions of the constituent materials. The results highlight the coupling between materials, the sliding interface configuration (determines wear performance and frictional heat generation), and the heat dissipation efficiency of the overall composite. This indicates the necessity to take all related factors into design consideration for simultaneously addressing wear and thermal design requirements. The second case study presents a sequentially coupled optimization procedure where the sliding interface is prescribed and fixed based on a prior mechanical wear-only optimization for minimal run-in volume loss. Metal/ceramic composites have been optimized for the dissipation of design-independent frictional heat under different material volume fraction constraints. It is observed that the improvements offered by increasing the volume fraction of the high-conductivity material are subject to diminishing returns. In

both case studies, significant reductions in both the average and maximum temperatures can be achieved at sliding interfaces. This framework can provide guidance for the design of tribological composites in order to more efficiently and effectively use available materials.

Chapter 6

Conclusions and future work

Conclusions

This dissertation presents a systematic design framework for tribological composites. The framework integrates efficient and accurate predictive wear models with topology optimization to design composites that will meet ever more demanding multifunctional performance requirements.

A promising foundation-based wear model has been extended to simulate wear of composites in rotary sliding systems. The rotary wear model combines Archard's wear equation (with modifications for rotary sliding) with the Pasternak foundation model. The evolution of key wear features including material volume loss, composite wear rate, and worn surface profile predicted by the iterative simulation exhibit the experimentally observed transitions from run-in to steady-state wear regimes. A direct solution method for steady-state rotary wear performance has been developed and used to identify counterintuitive bi-material com-

posite designs for minimal steady-state composite wear rates. This direct solution was used to provide demonstrations of designing composite surfaces for target steady-state surface profiles.

For composites subject to rotary wear, it is shown that the steady-state composite wear rate depends both on the area fraction of each constituent and the in-plane material distribution. For rotationally symmetric bi-material composites with fixed material area fractions, it is surprising that steady-state composite wear rates always reach minimum values when placing the more wear-resistant material (having the lower wear rate of the two constituents) towards the inner radius and the less wear-resistant material at the outer annulus edges. This counterintuitive optimal design solution has been validated by experiments.

The foundation-based wear model has also been formulated into a generalized wear simulation framework with improved accuracy and physical relevancy for both rotary and linear wear systems. Improvements have been made through incorporating implicit boundary conditions for the contact analysis, proposing an asymmetric elastic foundation model for linear wear, and formulating an optimization-based calibration procedure for the elastic foundation parameters (that are difficult to directly determine via experiment). The effectiveness of the proposed framework has been demonstrated by examples on both rotary and linear wear systems.

Analysis for the frictional heating associated with wear has been presented and integrated into a thermomechanical wear model through the incorporation of temperature-dependent wear rates. An iterative simulation procedure, consisting of sequential contact and frictional heat transfer analysis and wear calculations, has been established for thermomechanical wear. It is seen that the composite surfaces predicted by this thermomechanical

model undergo the typical transition from run-in to steady-state wear regimes despite the complex coupling of contact, thermal, and wear processes.

A density-based topology optimization framework has been presented, for the first time, to design three-dimensional bi-material composites for efficient dissipation of frictional heating with constraints on wear performance at sliding interfaces. Significant reductions in both the average and maximum contact temperatures are achieved by the optimized composite design. It is found that the optimal solutions are highly dependent on the relative tribological and thermal properties as well as on the volume fractions of the constituent materials. The results highlight the coupling between materials, the sliding interface configuration (which determines wear performance and frictional heat generation), and the heat dissipation efficiency of the overall composite. In addition, a sequentially coupled optimization for wear and frictional heat dissipation has been performed on metal/ceramic composites where the material layout at the sliding interface is fixed based on a solution from a mechanical-only wear optimization for minimal run-in volume loss. It is observed that the improvements offered by increasing the volume fraction of the high-conductivity material are subject to diminishing returns. This framework is used to guide the design of tribological composites in order to more efficiently and effectively use available materials.

Future work

Future work should focus on tailoring and improving the modeling and design framework for specific real-world applications. That is, the suitability of the models and assumptions presented in Section 2.1 and Section 3.1 (for applications beyond chemical mechanical polishing [10] and dinosaur dentition [36, 37]) must be considered on a case-by-case basis. For

example, the elastic foundation models assume perfect and conformal contact between a rigid wearing body and a fully compliant elastic abrasive counter-body. Alternative contact models (such as viscoelastic foundation models) that are suitable for particular applications could be introduced into the wear simulation framework presented in this dissertation.

Instead of assuming quasi-steady heat transfer, transient heat transfer analysis could be performed to obtain the evolving thermal field within the sliding body, especially for high-speed sliding systems. Additionally, the evolving geometry caused by material loss during wear should be taken into account in the heat transfer analysis. Wear experiments with specialized thermal measurements are needed to assess the established frictional heat transfer analysis and obtain temperature-dependent wear rates of materials. Other thermally-induced phenomena, such as thermal expansion and thermal stresses, could also be studied based on the modeling framework established in this dissertation.

For the topology optimization component, alternative objective functions, such as the maximum temperature at the sliding interface or in a particular material domain, could be of interest. Multiobjective topology optimizations that simultaneously address wear and frictional heat dissipation performance could be established. This would require a fully coupled thermomechanical wear model. It is also of interest to consider the optimization of frictional heating dissipation during the transient run-in wear regime which involves dramatic changes in contact pressure and surface profile. Manufacturing constraints such as minimum or maximum feature sizes and uncertainties could also be incorporated into the optimization procedure for practical applications. Finally, the presented optimized multifunctional composite designs could be fabricated and experimentally tested to validate the topology optimization protocol for heat dissipation with wear constraints.

Bibliography

[1] Robert Carpick, Andrew Jackson, Peter Lee, Nicolas Argibay, Angela Pachon Garcia, Gregory Sawyer, and Kristin Bennet. Tribology Opportunities for Enhancing America's Energy Efficiency. Technical Report February, 2017.

[2] Ian M. Hutchings and Philip Shipway. *Tribology : friction and wear of engineering materials*.

[3] H. Peter. Jost. *Lubrication (tribology) education and research : a report on the present position and industry's needs*. H.M. Stationery Off., London, 1966.

[4] Kenneth Holmberg and Ali Erdemir. Influence of tribology on global energy consumption, costs and emissions. *Friction*, 5(3):263–284, 2017.

[5] G. W. (Gwidon W.) Stachowiak. *Wear–materials, mechanisms and practice*. Wiley, 2005.

[6] I. M. Hutchings. Abrasion processes in wear and manufacturing. *Proceedings of the Institution of Mechanical Engineers, Part J: Journal of Engineering Tribology*, 216(2):55–62, 2002.

[7] A.I. Vakis, V.A. Yastrebov, J. Scheibert, L. Nicola, D. Dini, C. Minfray, A. Almqvist, M. Paggi, S. Lee, G. Limbert, J.F. Molinari, G. Anciaux, R. Aghababaei, S. Echeverri Restrepo, A. Papangelo, A. Cammarata, P. Nicolini, C. Putignano, G. Carbone, S. Stupkiewicz, J. Lengiewicz, G. Costagliola, F. Bosia, R. Guarino, N.M. Pugno, M.H. Müser, and M. Ciavarella. Modeling and simulation in tribology across scales: An overview. *Tribology International*, 125:169–199, 2018.

[8] D. Majcherczak, P. Dufrenoy, and Y. Berthier. Tribological, thermal and mechanical coupling aspects of the dry sliding contact. *Tribology International*, 40(5):834–843, 2007.

[9] H. Uetz and J. Föhl. Wear as an energy transformation process. *Wear*, 49(2):253–264, 1978.

[10] W.G. Sawyer. Surface Shape and Contact Pressure Evolution in Two Component Surfaces: Application to Copper Chemical Mechanical Polishing. *Tribology Letters*, 17(2):139–145, 2004.

[11] W Gregory Sawyer, Nicolas Argibay, David L Burris, and Brandon A Krick. Mechanistic Studies in Friction and Wear of Bulk Materials. 2014.

[12] G. W. (Gwidon W.) Stachowiak and A. W. (Andrew W.) Batchelor. *Experimental methods in tribology*. Elsevier, 2004.

[13] Francis E. Kennedy. Thermal and thermomechanical effects in dry sliding. *Wear*, 100(1-3):453–476, 1984.

[14] Kyle G Rowe, Alexander I Bennett, Brandon A Krick, and W Gregory Sawyer. In

situ thermal measurements of sliding contacts. 2013.

[15] J. F. Archard and W. Hirst. The wear of metals under unlubricated conditions. *Proceedings of the Royal Society of London. Series A. Mathematical and Physical Sciences*, 236(1206):397–410, 1956.

[16] J.A. Williams. Wear modelling: analytical, computational and mapping: a continuum mechanics approach. *Wear*, 225-229:1–17, 1999.

[17] Igor Viktorovich. Kragelskii, M. N. (Mikhail Nikolaevich) Dobychin, and V. S. (Viacheslav Sergeevich) Kombalov. *Friction and wear : calculation methods*. Pergamon Press, 1982.

[18] S.M. Hsu, R.G. Munro, M.C. Shen, and R.S. Gates. Boundary Lubricated Wear. In *Wear - Materials, Mechanisms and Practice*, pages 37–70. John Wiley & Sons Ltd, Chichester, England, 2014.

[19] J. A. Sierra Suarez and C. F. Higgs. A Contact Mechanics Formulation for Predicting Dishing and Erosion CMP Defects in Integrated Circuits. *Tribology Letters*, 59(2):36, 2015.

[20] H.C. Meng and K.C. Ludema. Wear models and predictive equations: their form and content. *Wear*, 181-183:443–457, 1995.

[21] Liangchi Zhang and Hiroaki Tanaka. Towards a deeper understanding of wear and friction on the atomic scalea molecular dynamics analysis. *Wear*, 211(1):44–53, 1997.

[22] Inkook Jang, David L. Burris, Pamela L. Dickrell, Peter R. Barry, Catherine Santos, Scott S. Perry, Simon R. Phillpot, Susan B. Sinnott, and W. Gregory Sawyer. Sliding

orientation effects on the tribological properties of polytetrafluoroethylene. *Journal of Applied Physics*, 102(12):123509, 2007.

[23] K. Cheng, X. Luo, R. Ward, and R. Holt. Modeling and simulation of the tool wear in nanometric cutting. *Wear*, 255(7-12):1427–1432, 2003.

[24] K L Johnson. Contact mechanics and the wear of metals. *Wear*, 190:162–170, 1995.

[25] A. Kapoor. Wear by plastic ratchetting. *Wear*, 212(1):119–130, 1997.

[26] Yushu Wang and Stephen M. Hsu. Wear and wear transition mechanisms of ceramics. *Wear*, 195(1-2):112–122, 1996.

[27] K. Komvopoulos and S.-S. Cho. Finite element analysis of subsurface crack propagation in a half-space due to a moving asperity contact. *Wear*, 209(1-2):57–68, 1997.

[28] A. Faulkner and R.D. Arnell. The development of a finite element model to simulate the sliding interaction between two, three-dimensional, elastoplastic, hemispherical asperities. *Wear*, 242(1-2):114–122, 2000.

[29] Rong Liu and D.Y Li. A finite element model study on wear resistance of pseudoelastic TiNi alloy. *Materials Science and Engineering: A*, 277(1-2):169–175, 2000.

[30] Priit Põdra and Sören Andersson. Finite element analysis wear simulation of a conical spinning contact considering surface topography. *Wear*, 224:13–21, 1999.

[31] Nam Ho Kim, Dongki Won, David Burris, Brian Holtkamp, Gregory R Gessel, Paul Swanson, and Gregory Sawyer. Finite element analysis and experiments of metal/metal wear in oscillatory contacts. *Wear*, 258:1787–1793, 2005.

[32] Saad Mukras, Nam H. Kim, W. Gregory Sawyer, David B. Jackson, and Lawrence W. Bergquist. Numerical integration schemes and parallel computation for wear prediction using finite element method. *Wear*, 266(7-8):822–831, 2009.

[33] I.R McColl, J Ding, and S.B Leen. Finite element simulation and experimental validation of fretting wear. *Wear*, 256(11-12):1114–1127, 2004.

[34] Jorge C. Fialho, Paulo R. Fernandes, Luis Eça, and João Folgado. Computational hip joint simulator for wear and heat generation. *Journal of Biomechanics*, 40(11):2358–2366, 2007.

[35] Priit Põdra and Sören Andersson. Wear simulation with the Winkler surface model. *Wear*, 207:79–85, 1997.

[36] Gregory M Erickson, Brandon A Krick, Matthew Hamilton, Gerald R Bourne, Mark A Norell, Erica Lilleodden, and W Gregory Sawyer. Complex dental structure and wear biomechanics in hadrosaurid dinosaurs. *Science (New York, N.Y.)*, 338(6103):98–101, 2012.

[37] Gregory M Erickson, Mark A Sidebottom, John F Curry, David Ian Kay, Stephen Kuhn-Hendricks, Mark A Norell, W Gregory Sawyer, and Brandon A Krick. Paleotribology: development of wear measurement techniques and a three-dimensional model revealing how grinding dentitions self-wear to enable functionality. *Surface Topography: Metrology and Properties*, 4(2):024001, 2016.

[38] Mark A. Sidebottom, Florian Feppon, Natasha Vermaak, and Brandon A. Krick. Modeling Wear of Multimaterial Composite Surfaces. *Journal of Tribology*, 138(4):041605, 2016.

[39] Florian Feppon, Mark A. Sidebottom, Georgios Michailidis, Brandon A. Krick, and Natasha Vermaak. Efficient Steady-State Computation for Wear of Multimaterial Composites. *Journal of Tribology*, 138(3):031602, 2016.

[40] Florian Feppon, G Michailidis, MA Sidebottom, Grégoire Allaire, BA Krick, and N Vermaak. Introducing a level-set based shape and topology optimization method for the wear of composite materials with geometric constraints. *Structural and Multidisciplinary Optimization*, 55(2):547–568, 2017.

[41] Tomas Grejtak, Xiu Jia, Florian Feppon, Sam G. Joynson, Annaliese R. Cunniffe, Yupin Shi, David P. Kauffman, Natasha Vermaak, and Brandon A. Krick. Topology Optimization of Composite Materials for Wear: A Route to Multifunctional Materials for Sliding Interfaces. *Advanced Engineering Materials*, page 1900366, 2019.

[42] Ronald F. Gibson. A review of recent research on mechanics of multifunctional composite materials and structures. *Composite Structures*, 92(12):2793–2810, 2010.

[43] Isaac M. Daniel and Ori. Ishai. *Engineering mechanics of composite materials*. Oxford University Press, 2006.

[44] Roy Cox. *Engineered Tribological Composites*. SAE International, Warrendale, PA, 2011.

[45] Klaus Friedrich. *Advances in composite tribology*. Elsevier, 1993.

[46] N.W. Khun, D.W. Sun, M.X. Huang, J.L. Yang, and C.Y. Yue. Wear resistant epoxy composites with diisocyanate-based self-healing functionality. *Wear*, 313(1-2):19–28, 2014.

[47] K. Friedrich, Z. Lu, and A.M. Hager. Recent advances in polymer composites' tribology. *Wear*, 190(2):139–144, 1995.

[48] Sture Hogmark, Staffan Jacobson, and Mats Larsson. Design and evaluation of tribological coatings. *Wear*, 246(1-2):20–33, 2000.

[49] Martin Philip Bendsøe and Ole Sigmund. *Topology Optimization: Theory, Methods and Applications*. 2003.

[50] Martin Philip Bendsøe and Noboru Kikuchi. Generating optimal topologies in structural design using a homogenization method. *Computer Methods in Applied Mechanics and Engineering*, 71(2):197–224, 1988.

[51] Grégoire Allaire, François Jouve, and Anca-Maria Toader. A level-set method for shape optimization. *Comptes Rendus Mathematique*, 334(12):1125–1130, 2002.

[52] Michael Yu Wang, Xiaoming Wang, and Dongming Guo. A level set method for structural topology optimization. *Computer Methods in Applied Mechanics and Engineering*, 192(1-2):227–246, 2003.

[53] Grégoire Allaire, François Jouve, and Anca-Maria Toader. Structural optimization using sensitivity analysis and a level-set method. *Journal of Computational Physics*, 194(1):363–393, 2004.

[54] Li Li, Michael Yu Wang, and Peng Wei. XFEM schemes for level set based structural optimization. *Frontiers of Mechanical Engineering*, 7(4):335–356, 2012.

[55] Haipeng Jia, H G Beom, Yuxin Wang, Song Lin, and Bo Liu. Evolutionary level set method for structural topology optimization. *Computers and Structures*, 89:445–454,

2011.

[56] S.Y. Wang, K.M. Lim, B.C. Khoo, and M.Y. Wang. An extended level set method for shape and topology optimization. *Journal of Computational Physics*, 221(1):395–421, 2007.

[57] Xiaodong Huang and Yi-Min Xie. A further review of ESO type methods for topology optimization. *Structural and Multidisciplinary Optimization*, 41(5):671–683, 2010.

[58] Xu Guo, Weisheng Zhang, Jian Zhang, and Jie Yuan. Explicit structural topology optimization based on moving morphable components (MMC) with curved skeletons. *Computer Methods in Applied Mechanics and Engineering*, 310:711–748, 2016.

[59] Weisheng Zhang, Junfu Song, Jianhua Zhou, Zongliang Du, Yichao Zhu, Zhi Sun, and Xu Guo. Topology optimization with multiple materials via moving morphable component (MMC) method. *International Journal for Numerical Methods in Engineering*, 113(11):1653–1675, 2018.

[60] A.R. Yildiz, N. Öztürk, N. Kaya, and F. Öztürk. Integrated optimal topology design and shape optimization using neural networks. *Structural and Multidisciplinary Optimization*, 25(4):251–260, 2003.

[61] Sarah Bobby, Seymour M. J. Spence, and Ahsan Kareem. Data-driven performance-based topology optimization of uncertain wind-excited tall buildings. *Structural and Multidisciplinary Optimization*, 54(6):1379–1402, 2016.

[62] Boyan S. Lazarov, Ole Sigmund, Knud E. Meyer, and Joe Alexandersen. Experimental validation of additively manufactured optimized shapes for passive cooling. *Applied*

Energy, 226:330–339, 2018.

[63] Alok Sutradhar, Glaucio H Paulino, Michael J Miller, and Tam H Nguyen. Topological optimization for designing patient-specific large craniofacial segmental bone replacements. *Proceedings of the National Academy of Sciences of the United States of America*, 107(30):13222–7, 2010.

[64] Ole Sigmund and Kurt Maute. Topology optimization approaches: A comparative review. *Structural and Multidisciplinary Optimization*, 2013.

[65] Joshua D. Deaton and Ramana V. Grandhi. A survey of structural and multidisciplinary continuum topology optimization: Post 2000. *Structural and Multidisciplinary Optimization*, 49(1):1–38, 2014.

[66] S Torquato, S Hyun, and A Donev. Multifunctional Composites: Optimizing Microstructures for Simultaneous Transport of Heat and Electricity. 2002.

[67] James K. Guest and Jean H. Prévost. Optimizing multifunctional materials: Design of microstructures for maximized stiffness and fluid permeability. *International Journal of Solids and Structures*, 43(22-23):7028–7047, 2006.

[68] A.V. Krysko, J. Awrejcewicz, S.P. Pavlov, K.S. Bodyagina, and V.A. Krysko. Topological optimization of thermoelastic composites with maximized stiffness and heat transfer. *Composites Part B: Engineering*, 158:319–327, 2019.

[69] Sarah L. Mitchell and Michael Ortiz. Computational multiobjective topology optimization of silicon anode structures for lithium-ion batteries. *Journal of Power Sources*, 326:242–251, 2016.

[70] F. Feppon, G. Michailidis, M. A. Sidebottom, G. Allaire, B. A. Krick, and N. Vermaak. Introducing a level-set based shape and topology optimization method for the wear of composite materials with geometric constraints. *Structural and Multidisciplinary Optimization*, 55(2):547–568, 2017.

[71] J. F. Archard. Contact and Rubbing of Flat Surfaces. *Journal of Applied Physics*, 24(8):981–988, 1953.

[72] Lars Pastewka, Stefan Moser, Peter Gumbsch, and Michael Moseler. Anisotropic mechanical amorphization drives wear in diamond. *Nature materials*, 10(1):34–38, 2011.

[73] Arnold D Kerr. Elastic and viscoelastic foundation models. *Journal of Applied Mechanics*, 31(3):491–498, 1964.

[74] WG Sawyer. Surface shape and contact pressure evolution in two component surfaces: application to copper chemical mechanical polishing. *Tribology letters*, 17(2):139–145, 2004.

[75] Kyle G Rowe, Gregory M Erickson, W Gregory Sawyer, and Brandon A Krick. Evolution in surfaces: interaction of topography with contact pressure during wear of composites including dinosaur dentition. *Tribology Letters*, 54(3):249–255, 2014.

[76] Mark A Sidebottom, Florian Feppon, Natasha Vermaak, and Brandon A Krick. Modeling wear of multimaterial composite surfaces. *Journal of Tribology*, 138(4):041605, 2016.

[77] Florian Feppon, Mark A Sidebottom, Georgios Michailidis, Brandon A Krick, and

Natasha Vermaak. Efficient steady-state computation for wear of multimaterial composites. *Journal of Tribology*, 138(3):031602, 2016.

[78] JR Vail, BA Krick, KR Marchman, and W Gregory Sawyer. Polytetrafluoroethylene (ptfe) fiber reinforced polyetheretherketone (peek) composites. *Wear*, 270(11):737–741, 2011.

[79] W Gregory Sawyer, Nicolas Argibay, David L Burris, and Brandon A Krick. Mechanistic studies in friction and wear of bulk materials. *Annual Review of Materials Research*, 44:395–427, 2014.

[80] Kenneth Langstreth Johnson and Kenneth Langstreth Johnson. *Contact mechanics*. Cambridge university press, 1987.

[81] Yong Hoon Lee, Jonathon K Schuh, Randy H Ewoldt, and James T Allison. Enhancing full-film lubrication performance via arbitrary surface texture design. *Journal of Mechanical Design*, 139(5):053401, 2017.

[82] Izhak Etsion, Gregory Halperin, and Gregory Ryk. Improving tribological performance of mechanical components by laser surface texturing. In *Hydraulic Failure Analysis: Fluids, Components, and System Effects*. ASTM International, 2001.

[83] Brett G Compton and Jennifer A Lewis. 3d-printing of lightweight cellular composites. *Advanced materials*, 26(34):5930–5935, 2014.

[84] Asaf Levy, Aslan Miriyev, Amy Elliott, Sudarsanam Suresh Babu, and Nachum Frage. Additive manufacturing of complex-shaped graded tic/steel composites. *Materials & Design*, 118:198–203, 2017.

[85] Xin Wang, Man Jiang, Zuowan Zhou, Jihua Gou, and David Hui. 3d printing of polymer matrix composites: a review and prospective. *Composites Part B: Engineering*, 110:442–458, 2017.

[86] Joshua J Martin, Brad E Fiore, and Randall M Erb. Designing bioinspired composite reinforcement architectures via 3d magnetic printing. *Nature communications*, 6:8641, 2015.

[87] Rachel R Collino, Tyler R Ray, Rachel C Fleming, James D Cornell, Brett G Compton, and Matthew R Begley. Deposition of ordered two-phase materials using microfluidic print nozzles with acoustic focusing. *Extreme Mechanics Letters*, 8:96–106, 2016.

[88] Dooroo Kim, Robert L Jackson, and Itzhak Green. Experimental investigation of thermal and hydrodynamic effects on radially grooved thrust washer bearings. *Tribology transactions*, 49(2):192–201, 2006.

[89] To Him Yu and Farshid Sadeghi. Groove effects on thrust washer lubrication. *Journal of Tribology*, 123(2):295–304, 2001.

[90] Florian Feppon, G Michailidis, MA Sidebottom, Grégoire Allaire, BA Krick, and N Vermaak. Introducing a level-set based shape and topology optimization method for the wear of composite materials with geometric constraints. *Structural and Multidisciplinary Optimization*, 55(2):547–568, 2017.

[91] TF Fwa, XP Shi, and SA Tan. Use of pasternak foundation model in concrete pavement analysis. *Journal of transportation engineering*, 122(4):323–328, 1996.

[92] Henri P. Gavin. The levenberg-marquardt method for nonlinear least squares curve-fitting problems. 2017.

[93] Xiu Jia, Tomas Grejtak, Brandon Krick, and Natasha Vermaak. Design of composite systems for rotary wear applications. *Materials & Design*, 134:281–292, 2017.

[94] BLOK and H. Theoretical Study of Temperature Rise at Surfaces of Actual Contact under Oiliness Lubricating Conditions. *Proc. Instn. Mech. Engrs. (General discussion on lubrication and lubricants)*, 2:222, 1937.

[95] JAEGER and JC. Moving sources of heat and the temperature of sliding contacts. *Proceedings of the Royal Society of New South Wales*, 76:203–224, 1942.

[96] F E Kennedy and Jr Associate Professor. Surface Temperatures in Sliding Systems-A Finite Element Analysis. Technical report, 1981.

[97] A. A. Yevtushenko and P. Grzes. The FEM-Modeling of the Frictional Heating Phenomenon in the Pad/Disc Tribosystem (A Review). *Numerical Heat Transfer, Part A: Applications*, 58(3):207–226, 2010.

[98] A.A. Yevtushenko, M. Kuciej, and O. Yevtushenko. Three-element model of frictional heating during braking with contact thermal resistance and time-dependent pressure. *International Journal of Thermal Sciences*, 50(6):1116–1124, 2011.

[99] A.A. Yevtushenko and P. Grzes. 3D FE model of frictional heating and wear with a mutual influence of the sliding velocity and temperature in a disc brake. *International Communications in Heat and Mass Transfer*, 62:37–44, 2015.

[100] G. Bergmann, F. Graichen, A. Rohlmann, N. Verdonschot, and G.H. van Lenthe. Frictional heating of total hip implants. Part 2: finite element study. *Journal of Biomechanics*, 34(4):429–435, 2001.

[101] M.S. Uddin and P. Majewski. Frictional Heating in Hip Implants A Review. *Procedia Engineering*, 56:725–730, 2013.

[102] R. Komanduri and Z.B. Hou. Analysis of heat partition and temperature distribution in sliding systems. *Wear*, 251(1-12):925–938, 2001.

[103] W Malalasekera and HK Versteeg. *An introduction to computational fluid dynamics: the finite volume method*. PEARSON Prentice Hall, 2007.

[104] Z.P. Lu and K. Friedrich. On sliding friction and wear of PEEK and its composites. *Wear*, 181-183:624–631, 1995.

[105] G. Rajaram, S. Kumaran, T. Srinivasa Rao, and M. Kamaraj. Studies on high temperature wear and its mechanism of AlSi/graphite composite under dry sliding conditions. *Tribology International*, 43(11):2152–2158, 2010.

[106] T. Dbouk. A review about the engineering design of optimal heat transfer systems using topology optimization. *Applied Thermal Engineering*, 112:841–854, 2017.

[107] Gil Ho Yoon. Topological layout design of electro-fluid-thermal-compliant actuator. *Computer Methods in Applied Mechanics and Engineering*, 209-212:28–44, 2012.

[108] Joe Alexandersen, Ole Sigmund, Knud Erik Meyer, and Boyan Stefanov Lazarov. Design of passive coolers for light-emitting diode lamps using topology optimisation. *International Journal of Heat and Mass Transfer*, 122:138–149, 2018.

[109] Alberto Pizzolato, Ashesh Sharma, Kurt Maute, Adriano Sciacovelli, and Vittorio Verda. Topology optimization for heat transfer enhancement in Latent Heat Thermal Energy Storage. *International Journal of Heat and Mass Transfer*, 113:875–888, 2017.

[110] Wenjie Zuo and Kazuhiro Saitou. Multi-material topology optimization using ordered SIMP interpolation. *Structural and Multidisciplinary Optimization*, 55(2):477–491, 2017.

[111] Grégoire Allaire and Lukas Jakabčin. Taking into account thermal residual stresses in topology optimization of structures built by additive manufacturing. *Mathematical Models and Methods in Applied Sciences*, 28(12):2313–2366, 2018.

[112] Martin Philip Bendsoe and Ole Sigmund. *Topology Optimization: Theory, Methods and Applications*. Springer, February 2004.

[113] Jaco Dirker and Josua P Meyer. Topology optimization for an internal heat-conduction cooling scheme in a square domain for high heat flux applications. *Journal of Heat Transfer*, 135(11):111010, 2013.

[114] Logan Garrick Page, Jaco Dirker, and Josua P Meyer. Topology optimization for the conduction cooling of a heat-generating volume with orthotropic material. *International Journal of Heat and Mass Transfer*, 103:1075–1083, 2016.

[115] Ole Sigmund. Morphology-based black and white filters for topology optimization. *Structural and Multidisciplinary Optimization*, 33(4-5):401–424, 2007.

[116] Ole Sigmund. On the Design of Compliant Mechanisms Using Topology Optimization. *Mechanics of Structures and Machines*, 25(4):493–524, 1997.

[117] Susana Rojas-Labanda and Mathias Stolpe. An efficient second-order SQP method for structural topology optimization. *Structural and Multidisciplinary Optimization*, 53(6):1315–1333, 2016.

[118] R.H.W. Hoppe, S.I. Petrova, and V. Schulz. Primal-Dual Newton-Type Interior-Point Method for Topology Optimization. *Journal of Optimization Theory and Applications*, 114(3):545–571, 2002.

[119] Krister Svanberg. The method of moving asymptotesa new method for structural optimization. *International journal for numerical methods in engineering*, 24(2):359–373, 1987.

[120] Francois H. Burger, Jaco Dirker, and Josua P. Meyer. Three-dimensional conductive heat transfer topology optimisation in a cubic domain for the volume-to-surface problem. *International Journal of Heat and Mass Transfer*, 67:214–224, 2013.

[121] Jaco Dirker and Josua P. Meyer. Topology Optimization for an Internal Heat-Conduction Cooling Scheme in a Square Domain for High Heat Flux Applications. *Journal of Heat Transfer*, 135(11):111010, 2013.

[122] Klaus Friedrich. *Advances in composite tribology*, volume 8. Elsevier, 2012.

[123] Tomas Grejtak, Xiu Jia, Florian Feppon, Sam G Joynson, Annaliese R Cunniffe, Yupin Shi, David P Kauffman, Natasha Vermaak, and Brandon A Krick. Topology optimization of composite materials for wear: A route to multifunctional materials for sliding interfaces. *Advanced Engineering Materials*, page 1900366.

Vita

Xiu Jia was born on August 30th, 1992 in Maanshan, Anhui, China. Xiu graduated from Maanshan No. 2 High School in 2010 and began her undergraduate study in the Department of Modern Mechanics at the University of Science and Technology of China (USTC). After graduating from USTC with a B.S. degree in Theoretical and Applied Mechanics in 2014, Xiu started her doctorate program under the supervision of Prof. Natasha Vermaak in the Department of Mechanical Engineering and Mechanics at Lehigh University. Her research focuses on the design of tribological composites for multifunctional applications through model development and topology optimization. At the time of graduation, Xiu has authored two and co-authored one journal articles (with another one article currently under review). Xiu has delivered six oral presentations at conferences (one invited). She has also presented three posters at conferences and workshops (one of which was awarded the ASME-IMECE NSF Student Poster Competition 2nd Place Award). Xiu has been honored as recipient of Lehigh's P.C. Rossin College of Engineering and Applied Science 2019 Graduate Student Leadership & Service Award and the 2017 Leslie Sperling Award from the Lehigh Emulsion Polymers Institute and Center for Polymer Science and Engineering. For the past four years, Xiu has been an active member in the student organization, Lehigh Women in Science and Engineering, and served as the President during the academic year of 2018-2019.